NAVAL POSTGRADUATE SCHOOL
MONTEREY, CALIFORNIA

THESIS

DIECAST MODEL SIMULATION
OF THE
CALIFORNIA COASTAL ZONE

by

Stanley A. Akahoshi

September, 1995

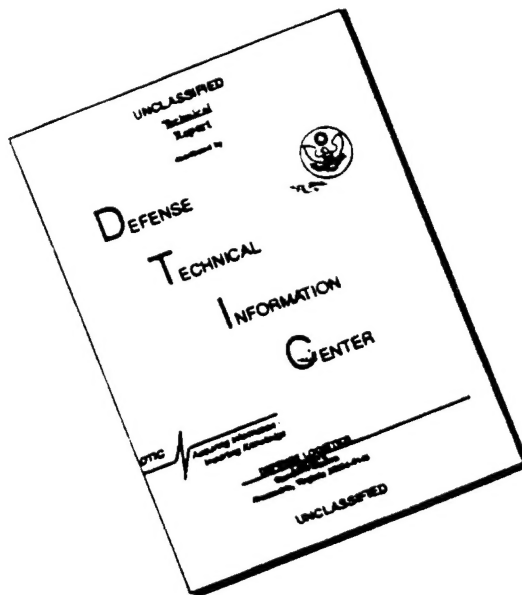Thesis Advisor: Robert L. Haney

Approved for public release; distribution is unlimited.

DISCLAIMER NOTICE

DEFENSE
TECHNICAL
INFORMATION
CENTER

THIS DOCUMENT IS BEST QUALITY AVAILABLE. THE COPY FURNISHED TO DTIC CONTAINED A SIGNIFICANT NUMBER OF PAGES WHICH DO NOT REPRODUCE LEGIBLY.

REPORT DOCUMENTATION PAGE

Form Approved OMB No. 0704-0188

1. AGENCY USE ONLY *(Leave blank)*	2. REPORT DATE September 1995	3. REPORT TYPE AND DATES COVERED Master's Thesis

4. TITLE AND SUBTITLE **DIECAST MODEL SIMULATION OF THE CALIFORNIA COASTAL ZONE**	5. FUNDING NUMBERS
6. AUTHOR(S) Akahoshi, Stanley, A	

7. PERFORMING ORGANIZATION NAME(S) AND ADDRESS(ES) Naval Postgraduate School Monterey CA 93943-5000	8. PERFORMING ORGANIZATION REPORT NUMBER

9. SPONSORING/MONITORING AGENCY NAME(S) AND ADDRESS(ES) Office of Naval Research Navy Ocean Modeling and Prediction 800 N. Quincy St. Arlington, Virginia 22217	10. SPONSORING/MONITORING AGENCY REPORT NUMBER

11. SUPPLEMENTARY NOTES   The views expressed in this thesis are those of the author and do not reflect the official policy or position of the Department of Defense or the U.S. Government.

12a. DISTRIBUTION/AVAILABILITY STATEMENT Approved for public release; distribution is unlimited.	12b. DISTRIBUTION CODE

13. ABSTRACT *(maximum 200 words)*

The high resolution DIECAST ocean model is used to simulate mesoscale variability in the California coastal zone. This simulation uses realistic topography and coastal geometry with boundary forcing only in the form of an equatorward-flowing jet, structured after observations, imposed at the northern boundary. The mesoscale features produced by the model are qualitatively consistent with those seen in observations. Their spatial scales are somewhat larger and their intensities somewhat weaker than in observations. The jet imposed at the northern boundary increases in horizontal and vertical scale as it meanders south through the domain. Cyclones and anticyclones are shown to have preferred locations and a general tendency for non-steady southwestward propagation with a phase speed of about 10 cm/s.

14. SUBJECT TERMS Diecast model, California coastal zone, California Current, Eddies			15. NUMBER OF PAGES 108
			16. PRICE CODE

17. SECURITY CLASSIFI- CATION OF REPORT Unclassified	18. SECURITY CLASSIFI- CATION OF THIS PAGE Unclassified	19. SECURITY CLASSIFI- CATION OF ABSTRACT Unclassified	20. LIMITATION OF ABSTRACT UL

NSN 7540-01-280-5500

Standard Form 298 (Rev. 2-89)
Prescribed by ANSI Std. 239-18 298-102

DIECAST MODEL SIMULATION
OF THE
CALIFORNIA COASTAL ZONE

Stanley A. Akahoshi
Lieutenant Commander, United States Navy
B.S., Trenton State College, 1982

Submitted in partial fulfillment
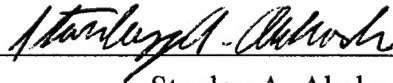of the requirements for the degree of

MASTER OF SCIENCE IN METEROLOGY AND PHYSICAL
OCEANOGRAPHY

from the
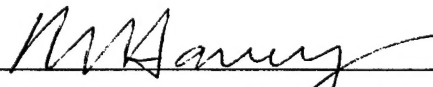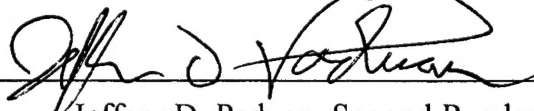
NAVAL POSTGRADUATE SCHOOL
September 1995

Author: _____

Stanley A. Akahoshi

Approved by: _____

Robert L. Haney, Thesis Advisor

_____

Jeffery D. Paduan, Second Reader

_____

Robert L. Haney, Chairman
Department of Meteorology

iii

ABSTRACT

The high resolution DIECAST ocean model is used to simulate mesoscale variability in the California coastal zone. This simulation uses realistic topography and coastal geometry with boundary forcing only in the form of an equatorward-flowing jet, structured after observations, imposed at the northern boundary. The mesoscale features produced by the model are qualitatively consistent with those seen in observations. Their spatial scales are somewhat larger and their intensities somewhat weaker than in observations. The jet imposed at the northern boundary increases in horizontal and vertical scale as it meanders south through the domain. Cyclones and anticyclones are shown to have preferred locations and a general tendency for non-steady southwestward propagation with a phase speed of about 10 cm/s.

TABLE OF CONTENTS

I.   INTRODUCTION

The purpose of this study is to describe and analyze a numerical simulation of the California coastal zone using the DIECAST (Dietrich/Center for Air Sea Technology) ocean model, and to compare the results with observations. This chapter briefly describes the California coastal zone, previous model studies, and the scope and intent of this study.

A.   NATURE OF THE CALIFORNIA COASTAL ZONE

The California Current is the southward-flowing eastern boundary current of the North Pacific gyre. It is strongest during summer when the upwelling favorable northerly winds are at a maximum due to the increased pressure gradient between the California low and the oceanic subtropical high off the California coast.

The basic conceptual model for the California coastal zone during summer is that of equatorward-flowing winds causing upwelling of cold, salty water along the coast and generating a coastal front with an equatorward-flowing coastal jet and a poleward-flowing undercurrent. Extensive analysis of this region during the Coastal Transition Zone (CTZ) experiment provided a more complex conceptual model for the region between 36°N and 42°N. The new picture is that of a meandering surface jet that interacts with a field of eddies and broadens south of 39°N where the eddies become more dominant (Strub et al., 1991).

Geosat altimeter data, along with coincident AVHRR (Advanced Very High Resolution Radiometer) and field data, show that the coastal front and inferred jet lie 20-50 km off Oregon and further from the coast off California, in a convoluted meandering pattern (Strub and James, 1995). The coastal front, which is located beyond the shelf break at 41.5°N (about 50 km south of the Oregon border), appears to mark the boundary between the cold, salty upwelled water and

1

the warmer, fresher offshore water (Kosro et al., 1991). The associated jet meanders southward with maximum velocities of 50-100 cm/s, alongshore wavelengths of O(200-300 km), and onshore-offshore displacement amplitudes of O(100-200 km) (Brink et al., 1991; Kosro et al., 1991).

Cold features referred to as filaments, appear on satellite imagery during the upwelling season. They can extend hundreds of kilometers offshore and have a tendency to be observed near capes such as Cape Mendocino, Point Arena, and Point Reyes. Drifter observations off Point Arena in July 1988 showed a cold filament extending 350 km offshore with surface currents exceeding 100 cm/s. The temporal development was strongly influenced by mesoscale variability, and the northern offshore temperature front of the filament was closely associated with the core of a broader high speed jet (Swensen et al., 1991). AVHRR satellite images of sea surface temperature clearly show eddies and filaments in the California coastal zone (see Figure 1.1).

B.   PREVIOUS MODEL STUDIES

1.   Batteen et al., 1989
The numerical study of Batteen et al., (1989) focused on the role of wind forcing in the California current system and supported the theory that wind forcing can be a significant factor for the formation of eddies. The model used hydrostatic, rigid-lid, beta-plane and f-plane, and Boussinesq approximations in a high resolution, 10 level, primitive equation model. In order to focus on wind forcing, the model used a flat bottom and a straight vertical wall for the California coast. The other three boundaries were open.

Experiments were run with summertime climatological wind forcing both with and without alongshore variability on both an f-plane and beta-plane. Each experiment resulted in the generation of an equatorward coastal jet and a poleward

undercurrent that would later become unstable and lead to the formation of eddies and jets. The horizontal scale of the eddies was similar to observations, but their intensity was significantly weaker than observed. Additionally, these eddies tended to form in the region of maximum alongshore wind stress, with the beta effect modifying the location of the eddy generation.

2. Haidvogel et al., 1991

The numerical study of Haidvogel et al., (1991) focused on the role of topography and coastal geometry in the evolution of a forced, surface-intensified, eastern boundary current. The model used hydrostatic, rigid-lid, f-plane, and Boussinesq approximations in a semi-spectral primitive equation model utilizing sigma (terrain-following) vertical coordinates. The model configuration was a channel with solid walls for the coastal and western boundaries and cyclic boundary conditions at the northern and southern boundaries, smoothed shelf and slope topography, and an irregular coastal geometry with a representative cape. Forcing consisted of nudging the system back to a broad O(300 km), geostrophically-balanced, equatorward jet on a time scale of 45 days. This equatorward jet had a maximum velocity of 45 cm/s located at the surface. There was no wind forcing included in this study.

The experiment produced simulated filaments with space and time scales, as well as current patterns and speeds, that compared well with observations. There was significant offshore transport of cold water and an eddy dipole was produced at the offshore end of a filament. Removal of the coastal cape or reversing the surface flow resulted in inhibited filament formation. These results suggest that shelf and slope topography, coastal geometry, and the existence of a strong equatorward jet are all important in the formation of filaments in the California coastal zone.

3

3.   McCreary et al., 1991

The numerical study of McCreary et al., (1991), used a non-linear 2 1/2-layer model that included entrainment of cool second-layer water into the upper layer. This model was applied to a highly-resolved regional rectangular basin (30°N to 45°N and three degrees longitude offshore) with open northern and western boundaries and a closed southern boundary. Forcing consisted of an upwelling-favorable alongshore wind field without curl. Winds were increased over a three month period to simulate the increase observed during spring.

The model was successful in simulating many observed features including the surface jet, undercurrent, the upwelling front, eddies, and filaments without any coastal capes or topographic features. The growth mechanism in this case was baroclinic instability with no preferred location along the coast. Eddies propagated offshore under the influence of the beta-effect, and there were differences between cyclonic and anticyclonic eddies due to the asymmetric effects of vertical turbulent mixing (entrainment).

C.   OBJECTIVE OF THIS STUDY

The objective of this study is to test the importance of boundary forcing, in the form of an equatorward-flowing surface jet, at the northern boundary, in driving the eastern boundary ocean variability. In this experiment there is no wind forcing, highly simplified (surface damping) buoyancy forcing, and no boundary forcing at the southern boundary.

In this study, the model used is one large step closer to being fully realistic for the California coastal zone. All of the previously discussed model studies generated results that were consistent with the basic conceptual model and compared well with observations, and each provided useful information on specific processes, e.g., the role of wind forcing,

4

topography, coastal geometry, a beta-plane, etc. However, each study had its own limitations or unrealistic aspects in order to focus on these specific mechanisms. In Batteen et al., (1989), wind forcing with alongshore variability was used but the bottom was modelled as flat and the coast as a vertical wall. In Haidvogel et al., (1991), an irregular coastline geometry was used, but the model used smoothed topography and a solid wall for the western boundary. Additionally, periodic boundary conditions at the north and south boundaries did not allow for a beta-effect. In McCreary et al., (1991), boundary conditions did allow for a beta-effect, but the model used was only a 2 1/2-layer model and the region was modelled as a rectangular basin. None of the models reached an equilibrium state.

In this study, the single effect of lateral boundary forcing in producing mesoscale variability in the California Current is investigated. Both realistic topography and coastal geometry have been used, and the use of open boundary conditions allow for a beta-plane. Wind forcing is therefore not used, but the alternate forcing mechanism is that of a realistic equatorward-flowing jet that is imposed at the northern boundary. Surface buoyancy forcing is highly simplified, but well-suited to this study which does not focus on the mixed-layer. A companion study utilizing steady, upwelling-season wind forcing in addition to the jet, will provide information on the role of wind forcing (J. Donato, personal communication, 1995).

The remainder of this paper is organized as follows: Chapter II describes the DIECAST model and the model parameters used in the experiment. Chapter III presents a description of the results including comparisons with available observations. Chapters IV and V are an analysis of the frequency and motion of closed eddies. Chapter VI is the conclusion.
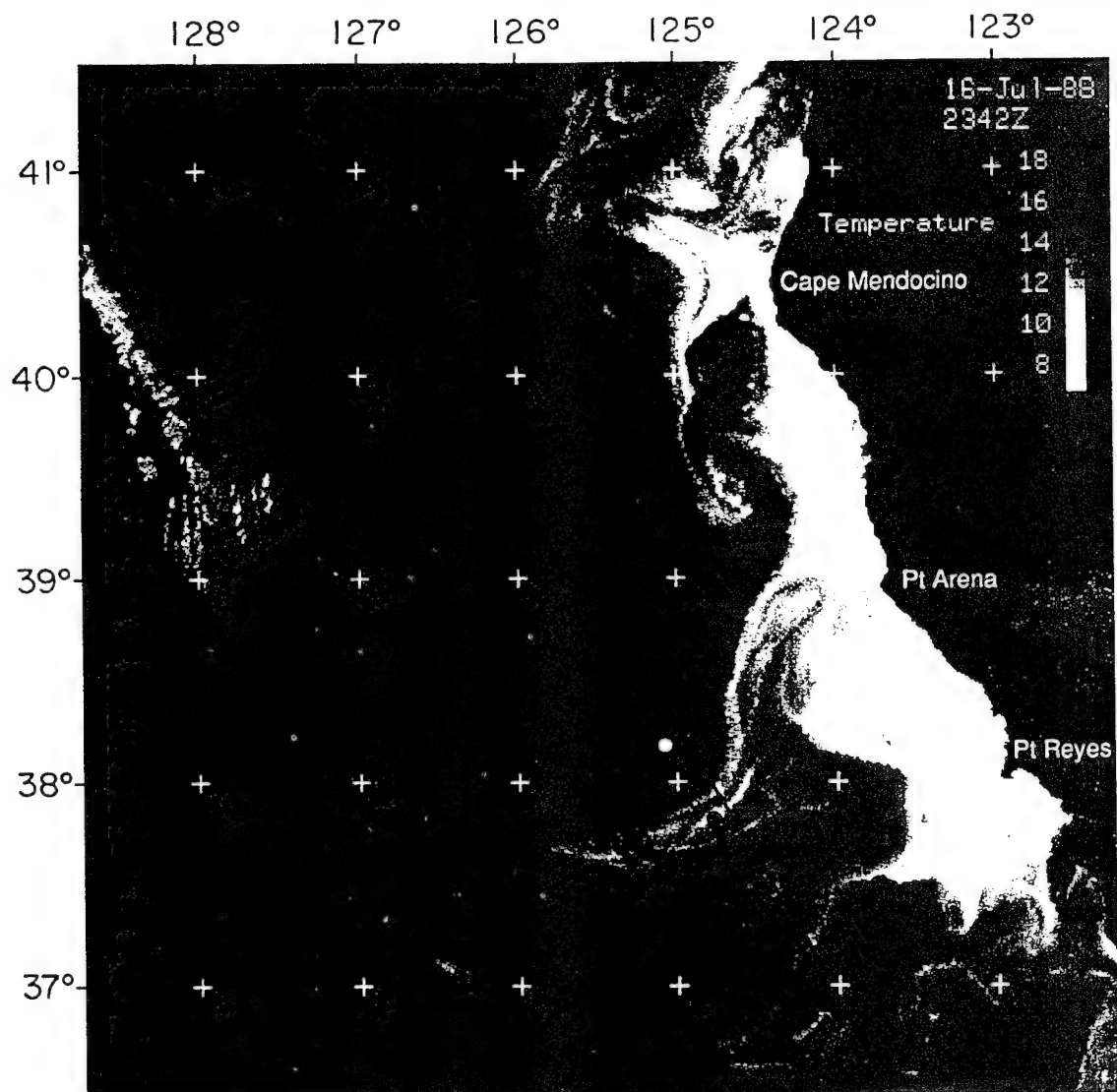
Figure 1.1. AVHRR (Advanced Very High Resolution Radiometer) satellite image taken on July 16, 1988, showing sea surface temperature in the California coastal zone. (from Dewey et al., 1991)

II. MODEL DESCRIPTION AND CONFIGURATION

This chapter provides a brief description of the DIECAST model and its configuration for the simulation being studied.

A. DIECAST MODEL

The DIECAST model is a hydrostatic, incompressible, rigid-lid, partially implicit, fully conservative, z-level, relocatable ocean circulation model. It uses an Arakawa 'a' grid with a special treatment of the incompressibility equation and the pressure gradient terms which are the weak points normally associated with that grid. This special treatment involves high order interpolations to a 'c' grid where computations are performed and then interpolated back to the 'a' grid. This combines the strengths of the two grids. (Dietrich and Ko, 1994)

B. MODEL CONFIGURATION

1. Domain

The domain of the model is from 32.0°N to 42.0°N and from the coast to 132.5°W. To remove possible boundary effects on the analyzed fields, the domain for the analysis has been reduced to 36.0°N to 42.0°N and from the California coast to 128.0°W. This domain corresponds to the California-Oregon border down to about 65 km south of Monterey, and from the California coast out to as much as 600 km seaward. The coastline includes Cape Mendocino, Point Arena, and Point Reyes (see Figure 2.1). Unless otherwise stated, domain will refer to the smaller region of analyzed data.

2. Resolution

Horizontal resolution is 1/12 degree providing a dx=7.2 km and a dy=9.2 km. Vertical resolution is 20 levels as shown in Table 2.1. Higher resolution in upper ocean was designed to resolve the larger vertical gradients in the upper ocean. This also provided for a realistic representation of the

7

topography by the model (see Figure 2.1). The bottom depths
are derived from the ETOPO-5 topographic data set.

level	depth	level	depth	level	depth	level	depth
1	10	6	181	11	612	16	1690
2	33	7	239	12	756	17	2052
3	60	8	308	13	930	18	2487
4	94	9	391	14	1138	19	3011
5	133	10	491	15	1389	20	3639

Table 2.1. Model level depths.

3. Initial Conditions

Initial conditions consisted of climatological summertime
(June-August) temperature and salinity data provided by
Levitus (1982). This data was applied throughout the three-
dimensional domain after interpolation from Levitus (1982) one
degree resolution climatological fields. Initial conditions
for the fields of temperature and salinity at 10 m and 239 m
depth are shown in Figure 2.2.

4. Boundary Conditions

The northern and southern boundaries are partially open
with the advection velocity normal to the boundary constant
and specified by the geostrophic currents computed from the
vertical sections of temperature and salinity. These vertical
sections are held constant at the Levitus values. The
northern boundary is augmented to produce a jet as discussed
below. The western boundary is also open but with the
advection velocity normal to the boundary determined by the
model velocity and damped to the geostrophic currents computed
from the Levitus fields. The southern and western boundaries
for the smaller area of data analysis are at least four
degrees inside the full model domain.

5.   Forcing

Primary model forcing is provided by a realistic equatorward-flowing surface jet imposed at the northern boundary. This is accomplished by adjusting the vertical latitude section of temperature and salinity at that boundary. Figure 2.3 shows the vertical sections of Levitus temperature and salinity at 42.0°N. Figure 2.4 shows the vertical sections of temperature and salinity after the adjustment is made to produce the imposed jet, and Figure 2.5a show the resulting vertical section of density (anomaly). These adjusted values are the northern boundary conditions. The resulting geostrophic velocity on the boundary is structured as a gaussian jet with a core velocity of 50 cm/sec, a horizontal scale of about 65 km, and a vertical scale of about 200 m (see Figure 2.5b). It is positioned about 100 km offshore at 42.0°N in 3000 m water and well beyond the slope region. This jet structure and placement is intended to replicate that observed in June 1987 during the Coastal Transition Zone (CTZ) experiment (Kosro et al., 1991).

The use of a jet for boundary forcing may be controversial in that the jet is usually thought of as the response to the wind forcing. Furthermore, since this establishes the structure of the jet at the northern boundary, it might be expected that any results having to do with the jet structure throughout the domain may be partially predetermined. This aspect will be looked at in Chapter III. However, the equatorward-flowing coastal jet at the northern boundary is the result of wind (and perhaps other) forcing outside the model domain. It is therefore considered to be a valid external forcing mechanism.

Surface buoyancy forcing is very much simplified and consists of damping the surface fields of temperature and salinity back to the initial Levitus (1982) values on a time scale of 60 days. McCreary et al., (1991) observed that

9

doubling the damping time scale from 40 to 80 days in his model study produced similar results, while only taking longer for his model to reach equilibrium. Thus, the exact value of the damping time scale used is not considered to be critical to the solution.
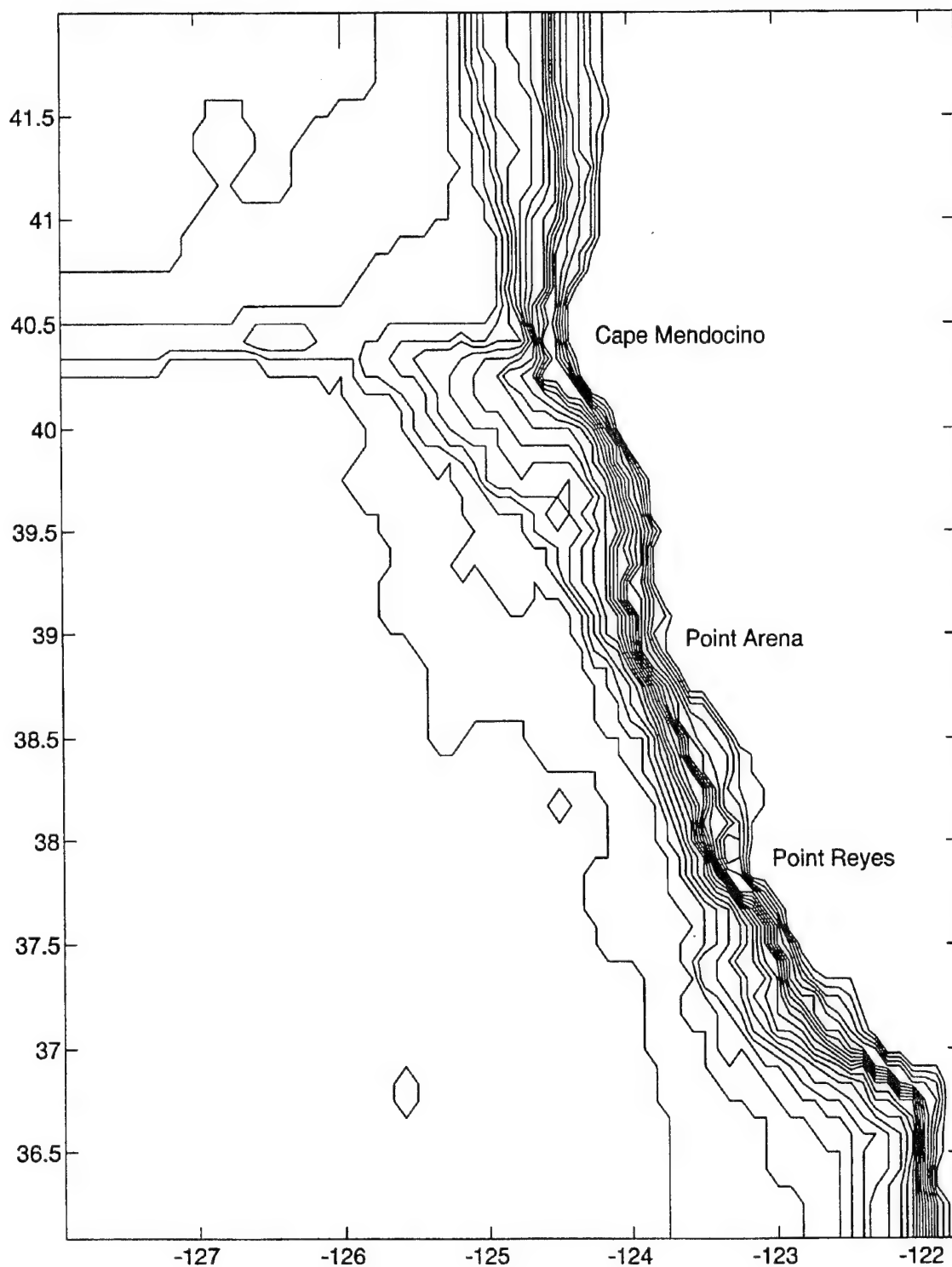
Figure 2.1. Model domain and topography. Contour values are the model levels listed in Table 2.1.
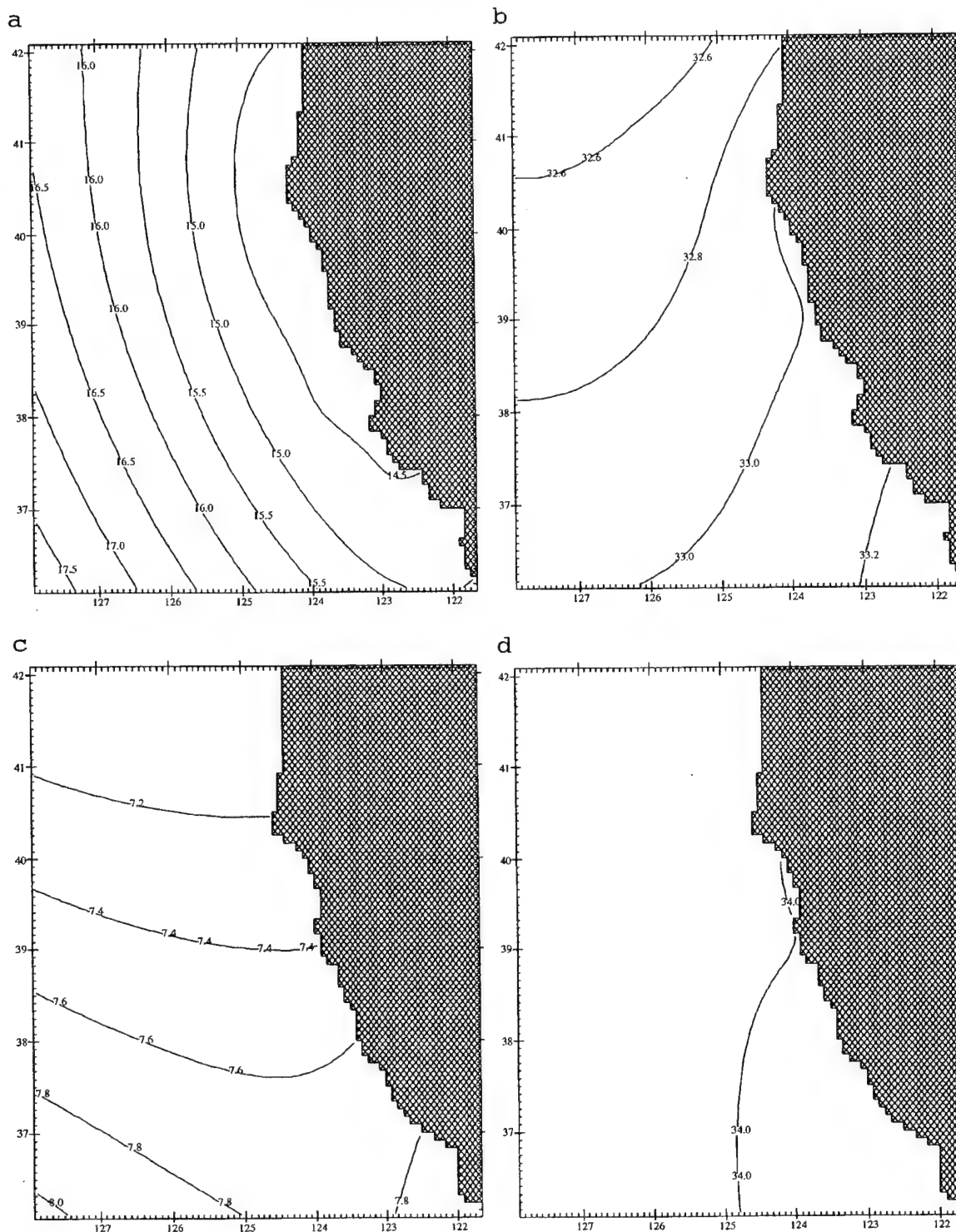
Figure 2.2. Initial conditions interpolated from Levitus (1982) climatological fields: (a) temperature (°C) at 10 m depth; (b) salinity (psu) at 10 m depth; (c) temperature (°C) at 239 m depth; (d) salinity (psu) at 239 m depth.
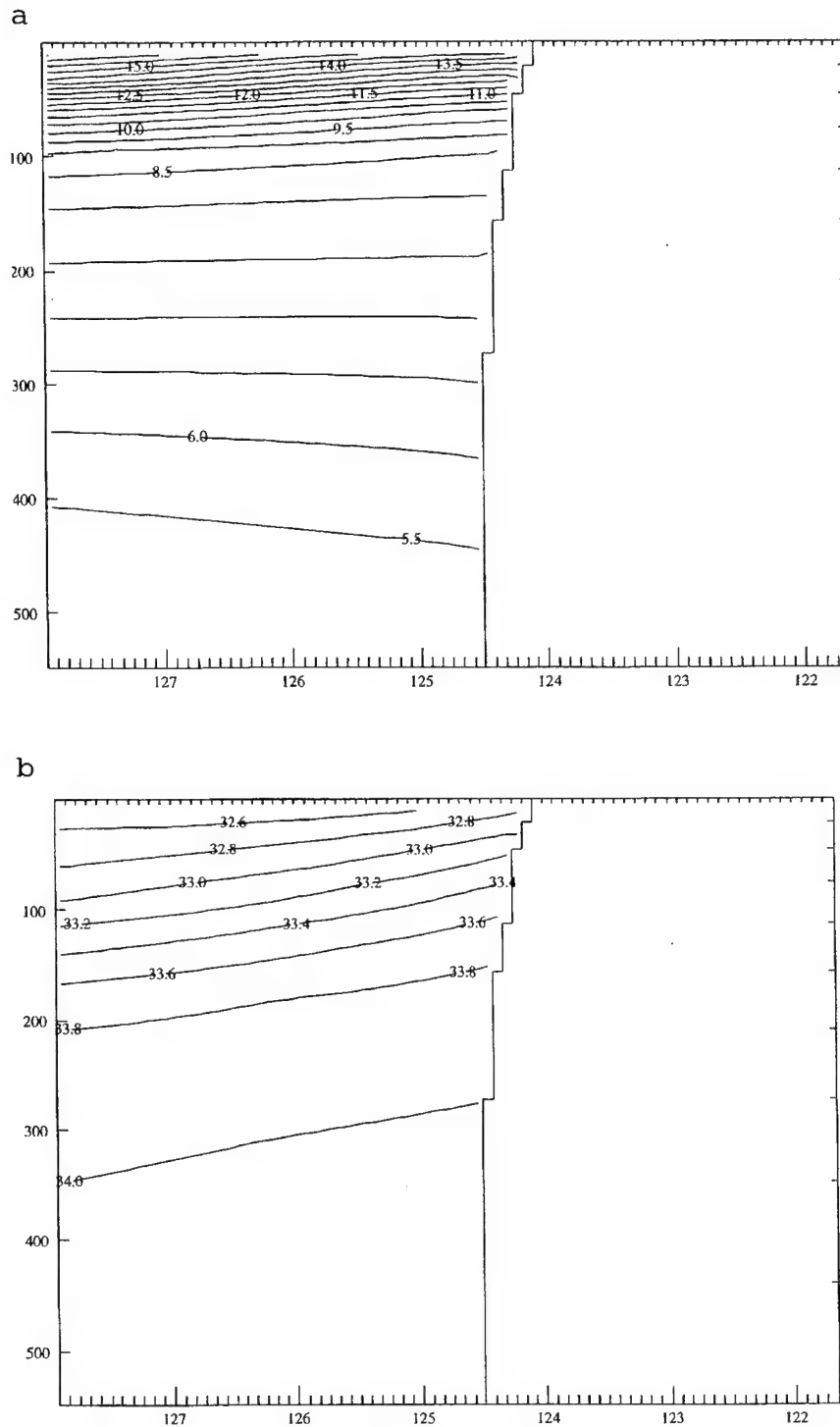
12

Figure 2.3.   Vertical sections interpolated from Levitus (1982) climatological fields at latitude 42.0°N, depth is in m: (a) temperature (°C); (b) salinity (psu).

13

a

b

Figure 2.4. Northern boundary conditions. Vertical sections after adjustment of Levitus (1982) climatological fields at latitude 42.0°N, depth is in m: (a) temperature (°C); (b) salinity (psu).
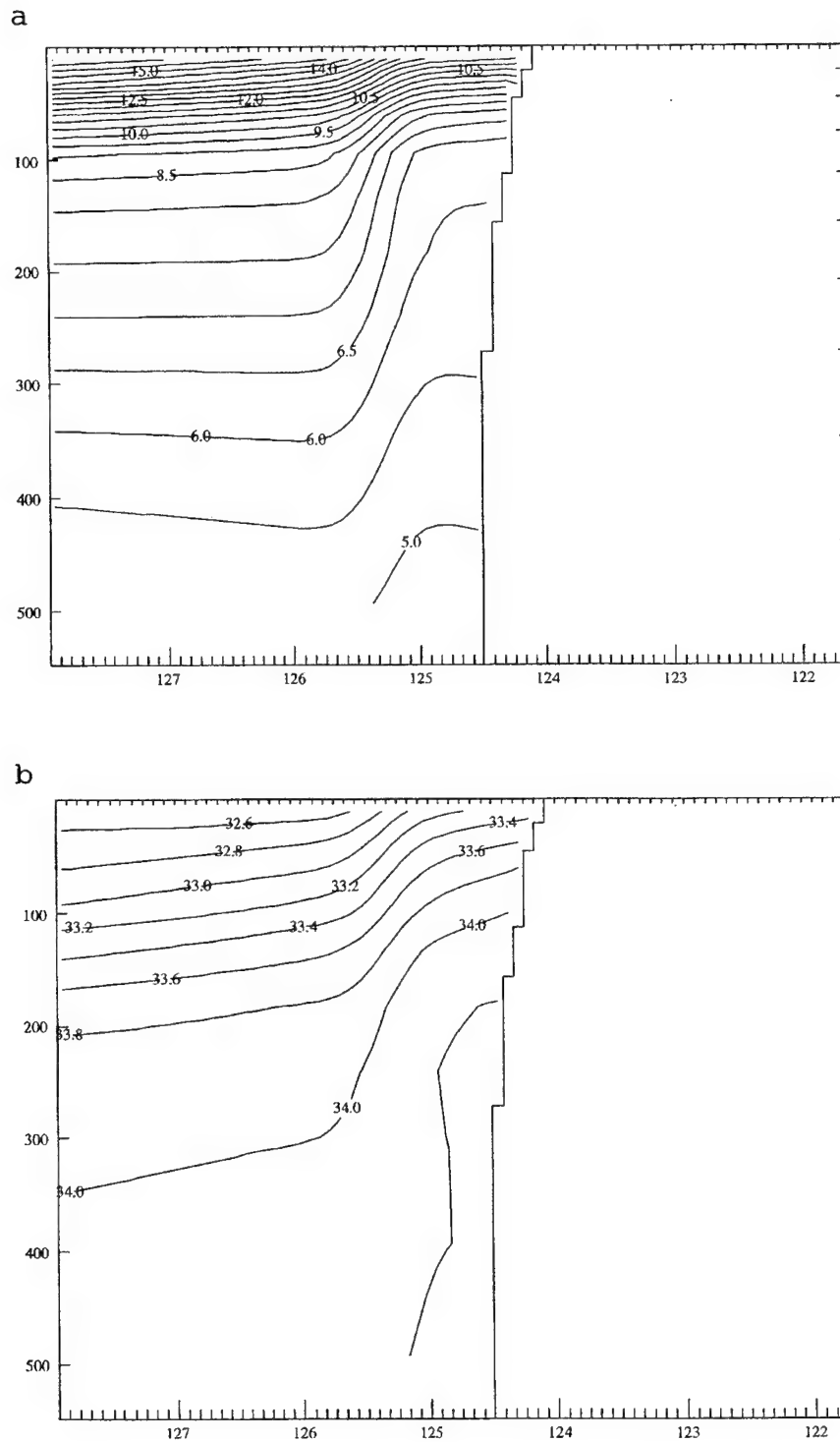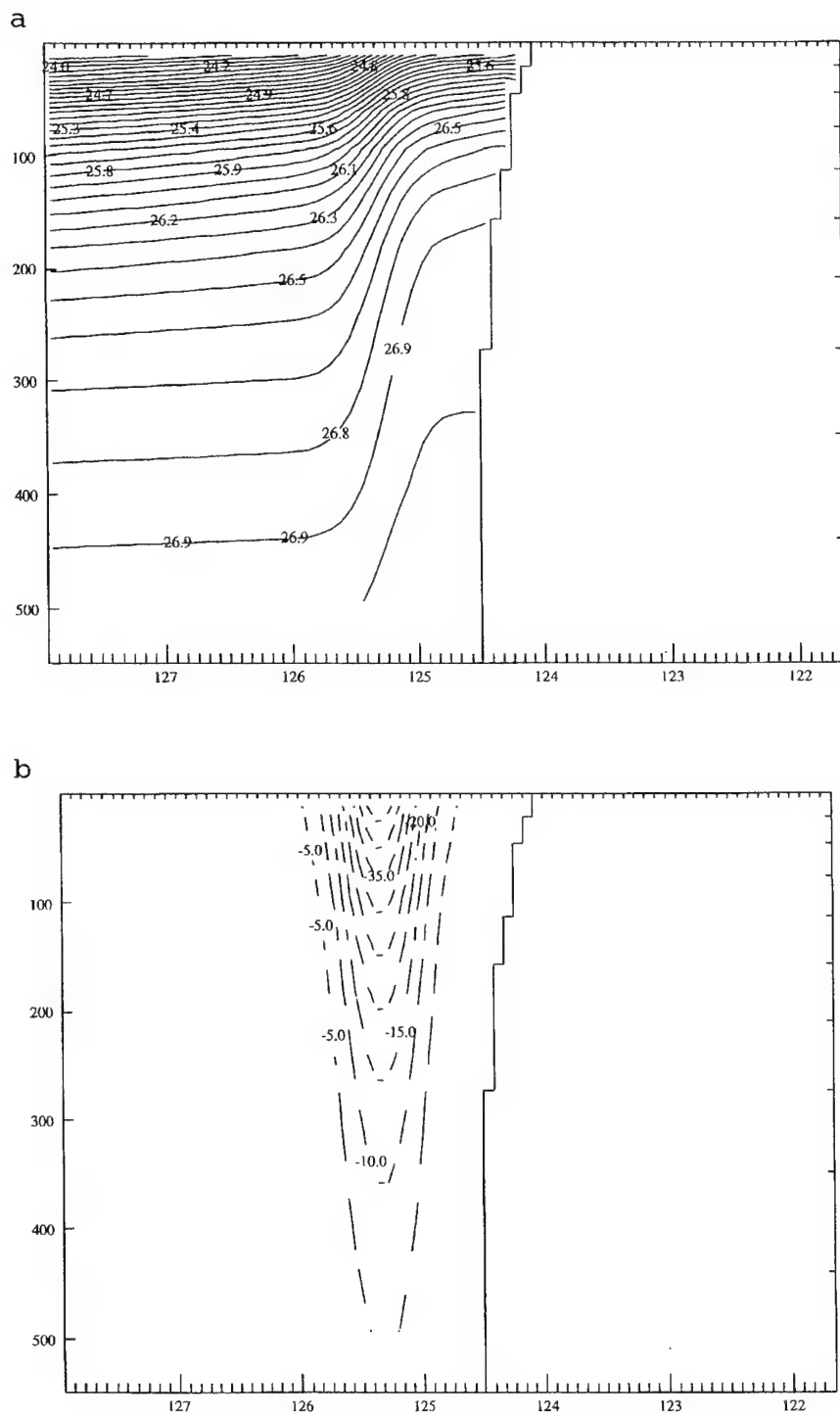
Figure 2.5.   Northern boundary conditions.   Vertical sections
after adjustment of Levitus (1982) climatological fields at
latitude 42.0°N, depth is in m: (a) density anomaly (kg/m^3);
(b) v-velocity (cm/s).

15

III.   MODEL SIMULATION RESULTS

In this chapter, model fields are analyzed and compared with available observations. The characteristic features of the California coastal zone including the coastal jet, eddies and the undercurrent, are compared with observations from the California Transition Zone (CTZ) experiment and the Coastal Ocean Dynamics Experiment (CODE).

A.   MODEL RUN TO EQUILIBRIUM

The model was run for five years. This long run ensured ample data would be available after allowing for the model to reach equilibrium.   To ensure the model had reached equilibrium before using data for analysis, time-series of model vertical velocity and density were taken at two locations, about 20 km and 100 km offshore of Point Arena (see Figure 3.1). The inshore time-series was taken at 10 m depth, while the offshore data was taken at 10 m and 491 m depth. Considerable variability on a wide spectrum of time-scales is apparent in all the time series and a near equilibrium state is reached after about 1-2 years with the vertical velocities reaching that state earlier than the density (see Figures 3.2 and 3.3).   Therefore, the data analyzed in this study will start with year three. This allows for three full years, or the equivalent of 12 (unfortunately not independent) summers of near-equilibrium data for analysis.

B.   TIME-EVOLUTION

Animation of the model fields of the pressure at 10 m revealed a distinct change in the model behavior over the three years. Year three (the first year analyzed) and year five were similar to each other, and consistent with the conceptual model for the California coastal zone. While year four took on a very different character as the coastal jet turned west and exited the domain just 100 km inside the

17

northern boundary.   The following summary of the time-evolution of the pressure fields will describe the major events, e.g., the formation of large meanders and eddies from the main flow.

1.   Year Three

Year three (days 722-1080) begins with the coastal jet flowing equatorward with meanders at Cape Mendocino, Point Arena, and Point Reyes (see Figure 3.4a). By day 790, the Cape Mendocino meander has extended to the western boundary where it has cut off and produced a westward propagating elongated cyclonic eddy, while the Point Arena meander has also cut off and produced a more intense westward propagating cyclonic circular eddy (see Figure 3.4b). By day 840, there are three new meanders at the three capes. By day 880, a weak cyclonic eddy cuts off from the Cape Mendocino meander, and a strong cyclonic eddy cuts off from the Point Arena meander. These two eddies combine to create a single strong eddy that then propagates westward (see Figure 3.4c). On about day 970, a meander that had propagated northward from below the southern boundary of data (and of the figures), cuts off and produces a cyclonic eddy offshore of Point Arena, temporarily hindering growth of the point Arena meander (see Figure 3.4d). On about day 1025, the Cape Mendocino meander, which has grown very large, cuts off and produces a 250 km diameter cyclonic eddy as it extends to the western boundary (see Figure 3.5a). By day 1050, the well-developed Point Arena meander absorbs a second meander that has propagated down from Cape Mendocino. This hinders eddy formation by creating a longer wavelength, smaller amplitude meander. A new meander has formed off Point Arena (see Figure 3.5b).

2.   Year Four

Year four (days 1082-1440) begins with another failure of the Point Arena meander to cut off as it elongates, absorbs another meander from Cape Mendocino, and retracts back towards

18

the coast (see Figure 3.5c). On about day 1125, the Point Reyes meander cuts off and produces a cyclonic eddy (see Figure 3.5d). By day 1200, the coastal jet has veered west and exited the domain just 100 km inside the northern border, returning towards the coast as a southeastward-flowing jet just inside the southwest corner of the domain (see Figure 3.6a). This results in an unusual pattern of weak currents, residual eddies from the previous year, and eddies that have drifted back into the domain from the region outside of the data area.

3. Year Five

By the beginning of year five (days 1442-1800), most of the jet has receded back to the coast with meanders at each of the three capes (see Figure 3.6b). By day 1500, the Point Arena meander, which had again come close to producing a closed eddy, absorbs still another meander from Cape Mendocino, creating one large meander from Cape Mendocino to Point Arena (see Figure 3.6c). By day 1576, this large meander has separated into two meanders, while a third meander is forming at Point Reyes. By day 1610, the Cape Mendocino meander has extended to the western boundary where it has cut off into a cyclonic circular eddy; while the Point Arena and Point Reyes meanders combine to form a single, longer wave length meander off Point Arena, again hindering eddy formation (see Figure 3.6d). On about day 1660, this large meander cuts off and produces a cyclonic eddy well offshore of the coastal jet (see Figure 3.7a). By day 1690, a Cape Mendocino meander has again propagated south to Point Arena and has been replaced by a new meander, while a third meander has formed off Point Reyes. By about day 1720, the Point Arena meander has extended to the western boundary where it partially absorbs an old cyclonic eddy from the region outside the data area, promptly releases it back into the same region, and then retreats back towards the coast (see Figure 3.7b). On about

19

day 1760, the Point Reyes meander cuts off and produces a cyclonic eddy (see Figure 3.7c). At the very end of the model run (day 1800), there are eddies nearing formation at both Cape Mendocino and Point Arena (see Figure 3.7d).

The evolution of the pressure fields shows that there is a long time scale variability with a time scale of approximately one year suggested by the three year run. Years three and five produce patterns consistent with the conceptual model, while year four shows a different and more slowly evolving pattern. Years three and five produce numerous cut-off eddies from meanders in the coastal jet, rather evenly distributed in time, with a shedding period of about 85 days. Year four does not produces any cut-off eddies of comparable scale and intensity, with the coastal jet meandering out of the domain and taking the remainder of the year to return to the coast. It is noted that this long time-scale variability, which occurs under steady boundary forcing, is likely to be altered with time-dependent (e.g., seasonal varying) forcing.

All of the eddies described above were intense cyclones that had formed from meanders in the coastal jet. Anticyclonic eddies were formed in conjunction with, or as a product of, the cyclone formation. These anticyclonic eddies were of similar scale but much less intense than the cyclonic eddies.

Meanders and eddies were observed to form at all three capes. However, some eddies were formed from meanders that had originated from an upstream cape. These meanders propagated downstream before amplifying and producing an eddy at the next cape. Additionally, it was observed that meanders propagating down to a cape where an eddy was already nearing formation, had a hindering effect on that eddy formation.

C.   HORIZONTAL FIELDS

Both instantaneous and averaged model fields are compared with observations. The instantaneous fields are compared to observed surface data from the CTZ experiment which was taken on a somewhat smaller domain. The averaged fields are compared with averaged data at 5 m and 150 m depths and taken on a still smaller domain during CODE.

1.   Instantaneous Fields

Subjectively, the surface fields are consistent with the conceptual model of a surface jet that meanders along the convoluted edge of a temperature front and interacts with a field of eddies with the eddies becoming more dominant south of 39.0°N (Strub et al., 1991; Strub and James, 1995).

Model fields of pressure, temperature, and salinity at 10 m depth for days 1000, 1250, 1500, and 1750 are shown in Figures 3.8-3.10, respectively. The coldest temperatures are 10.0-11.0°C and are located in the upwelling zones while the warmest temperatures are 15.0-16.0°C and located well offshore of the upwelling zone. Observed temperature fields from May and June, 1987 are shown in Figure 3.11. Considering that the observed analyses cover only the near-shore half of the model domain, the range of SST variability is qualitatively similar. Over a region from approximately the coast to 126°W and 37°N to 40°N (the region north of 40°N not used due to both the constraints at the northern boundary, and the large gap in the observations), model temperatures vary from about 10.5-13.5°C, which is very close to observations of 10.0-13.5°C, from June 1987. This indicates that the model establishes a meandering three degree temperature gradient in a manner consistent with observations.

The model fields of salinity for the same days show that the saltiest waters (about 33.4 psu) are found close to the coast while the freshest (about 32.6 psu) are found offshore

and toward the northwest. Over the same region as the observed data (Figure 3.11), model salinities vary from about 32.8-33.4 psu as opposed to observations of 32.4-33.5 psu, from June 1987. The model therefore establishes a salinity gradient that is only about half as strong as observations.

These results show that the model does a better job simulating the temperature fields than the salinity fields. Additionally, while regions of cold, salty water from near-shore appear in both the model and observed offshore eddy fields, the model scales of variability appear qualitatively larger than the observed scales. A summary comparison of the range of the model variables with that of the observations as shown in the above figures, is provided in Table 3.1.

variable	model	observations
temperature (°C)	10.5-13.5	10.0-13.5
salinity (psu)	32.8-33.4	32.4-33.5

Table 3.1. Comparison of the range of the model variables with those of observations (Kosro et al., 1991) in the area from approximately the coast to 126°W and 37°N to 40°N.

2. Mean Fields

The three year mean model fields of temperature and salinity at 10 m and 157 m depth (Figure 3.12), are compared to averages of observed fields at 5 m depth and 150 m depth from the summers of 1981-1982 (Figure 3.13). This comparison is made on a very small domain, from approximately Point Arena to Point Reyes and one degree of longitude offshore. The mean observed fields display a structure of a nearly monotonic increase of salinity and density toward shore, a nearly monotonic decrease of temperature toward shore, and a decrease in gradients with depth (Huyer and Kosro, 1987).

The existence of warm, fresh, and less dense water at grid points immediately next to the coastline, is an

22

unrealistic feature caused by the finite spatial resolution at the irregular boundary, where the water depth may also be shallow (see Figures 3.12). It is caused by the absence of complete advective ventilation at grid points that do not have "water" grid points adjacent to them (above, below, and to the sides). This narrow near-shore strip should simply be considered unresolved by the numerical model.

The range of the model temperatures at 10 m depth is about 11.0-12.0°C, which is much smaller than the observed range of 9.5-12.0°C, and probably indicates the absence of wind forcing in the model which would produce stronger upwelling along the coast. Model isotherms are nearly parallel to the coast, as opposed to observations where there is a divergence of isotherms away from the coast with a temperature decrease towards the south from 10.5 to 9.5°C.

The range of the model salinity at 10 m depth is about 33.1-33.4 psu, which is small compared to the observed range of 32.9-33.9 psu. The weak salinity gradient in the model is consistent with the weak temperature gradient and is most likely due to the absence of wind forcing and the associated coastal upwelling. The model does simulate some of the divergence of isohalines from the coast seen in the observed field. However, the model isohalines do not have the meanders seen in the offshore region of the observed field.

At 157 m depth, the range of the model temperatures is about 4.7-6.0°C, which is about three degrees colder, and indicates a significantly stronger gradient than the observed range of 8.0-8.6°C. Model isotherms are uniformly distributed and nearly parallel to the coast, while the observed isotherms are similar except for a warm tongue near the southwest corner. Additionally, there is no significant decrease in the gradient with depth as is seen in the observed fields.

The range of the model salinity at 157 m depth is about 34.1-34.3 psu, as opposed to 33.8-34.05 psu for the observed

range. At this depth the gradients are similar, but the model salinities are somewhat higher. Additionally, the model gradient at 157 m is about the same as it was near the surface, while the observed gradient at 150 m is only about one-fourth its near-surface value. A summary comparison of the range of the mean model variables with those of the observations as shown in the above figures is provided in Table 3.2.

The mean fields in this small area off Point Arena indicate a few aspects of the model that do not compare well with observations. Gradients of temperature and salinity do not decrease with depth (down to 150 m) as they do in observations. Gradients of temperature and salinity near the surface are weaker than in observations, and at 157 m depth temperature gradients are stronger, temperatures much colder, and salinities much higher than observations. Model isotherms and isohalines tend to be uniform and parallel to the coast, while observed isotherms and isohalines tend to diverge away from the coast and have meanders.

variable	model		observations	
temperature (°C)	11.0-12.0	(10 m)	9.5-12.0	(5 m)
salinity (psu)	33.1-33.4	(10 m)	32.9-33.9	(5 m)
temperature (°C)	4.7-6.0	(157 m)	8.0-8.6	(150 m)
salinity (psu)	34.1-34.3	(157 m)	33.8-34.05	(150 m)

Table 3.2. Comparison of the range of mean model variables with those of observations (Huyer and Kosro, 1987) in the area approximately from the coast to 124°W and 38°N to 39°N.

D. FEATURES OF THE CALIFORNIA COASTAL ZONE

In this section, the simulation of the characteristic features of the California coastal zone will be analyzed and compared with observations. These features include the

equatorward-flowing coastal jet, the poleward-flowing undercurrent, and eddies. Mixed-layer depth is not analyzed as there is no model formulation for vertical turbulent transport to force a mixed-layer response. The location, frequency of occurrence, and propagation of closed cyclonic and anticyclonic eddies will be investigated in the next two chapters.

1. Coastal Jet

As a result of the imposing of a specified jet at the northern boundary, the structure of the jet throughout the domain has been somewhat predetermined. It is the extent to which the interior jet structure is determined by the boundary specification that is of interest in this study. The symmetric gaussian jet, derived from a composite of observed southward directed jets near 41°N, is imposed at the northern boundary 100 km offshore with a core surface velocity of 50 cm/s, a horizontal scale of about 65 km, and a vertical scale of about 200 m (see Figure 2.5). This jet maintains it's general structure of a southward-flowing surface jet with a core velocity of 40-60 cm/s throughout the domain. However, as the jet meanders south, it tends to broaden both horizontally and vertically, and acquires both tilt and asymmetry. A summary comparison of the model jet with observations is provided in Table 3.3.

a. *Location, Amplitude, Wavelength*

Figure 3.8 shows the model fields of pressure at 10 m depth for days 1000, 1250, 1500, and 1750. An inspection of these and many others showed that the location of the jet is about 110-190 km offshore of Cape Mendocino which is consistent with observations (Kosro et al., 1991). Onshore-offshore amplitudes of 90-150 km and alongshore wavelengths of O(200) are consistent with observations derived from CTD data (Kosro et al., 1991) (see Figure 3.11).

b.   Velocity and Scale

Figure 3.14 shows east-west vertical sections of model v-velocity, at latitudes chosen to obtain a section with an east-west plane normal to the jet, on days 1000 and 1500. An inspection of these and many others show a core velocity of about 40-60 cm/s, which is consistent with but on the low end of observations of 50-100 cm/s, and about the same as that imposed at the northern boundary.

The horizontal and vertical scales of the model coastal jet were determined by measuring the width (total distance across the stream) and depth at which the velocity had decreased from its core value by a factor of 1/e. The model jet increases in horizontal scale from the 65 km imposed at the northern boundary to as much 110 km in the model interior, significantly larger than observations of 30-75 km (see Figure 3.15). The jet also increases in vertical scale, from the 200 m imposed at the northern boundary to as much as 350 m in the model interior, significantly larger than observations of 125-200 m (see Figure 3.15).

c.   Vertical Velocity

Model vertical velocities along the coast are generally weak. Figure 3.16 shows vertical cross sections of the three year mean vertical velocity taken along several latitudes. They indicate mean vertical velocities of less than 2 m/d along the full length of the coast. This suggests that the onshore geostrophic current, driven by the poleward pressure gradient due to the differences between the north and south boundary conditions, is too weak to force significant upwelling along the coast. This implies that the interior mean coastal jet is much more a product of the external forcing at the northern boundary (the imposed jet), than the poleward pressure gradient. Thus, the gradients produced and advected south by the imposed jet, are the primary cause of variability in the model simulation.

26

Observed estimates of vertical velocities associated with the meandering coastal jet are O(10-20 m/day) based on drifters near the surface (Brink et. al., 1991; Swensen et al., 1991), and as much as 40 m/day based on ADCP data taken to a depth of 250 m (Dewey et. al., 1991). Figures 3.17 and 3.18 are the horizontal fields of pressure and vertical velocity, respectively, for days 1000, 1250, 1500, and 1750, at 239 m depth. Maximum vertical velocities are about 10 m/day. An inspection of similar plots at deeper depths indicates that they remain at about that level down through most of the water column. These model vertical velocities are somewhat lower than observed estimates which is probably related to the model features being larger and less intense than the observed features (as previously discussed). Vertical velocity patterns associated with the coastal jet are consistent with quasi-geostrophic theory, with positive vorticity advection coinciding with rising motion, and negative vorticity advection coinciding with sinking motion.

d.   *Vorticity*

Although this model feature is qualitatively correct, the vorticity of the model jet is considerably weaker than that of observed jets. Using 60 cm/s for the model jet's core velocity and 35 km for its e-folding half width, one finds a maximum relative vorticity due to cross-stream shear to be about 0.15f, whereas observed jets have a relative vorticity of about 0.25-0.35f (Kosro et al, 1991; Huyer et al., 1991; Dewey et al., 1991).

An inspection of jet cross sections was performed to determine (1) if the cross jet asymmetry showed greater horizontal shear on either the onshore (positive vorticity) or the offshore (negative vorticity) side of the jet, and (2) if there was a tendency towards either onshore tilt or offshore tilt with depth. This inspection showed a high degree of variability, but identified more cases with

27

tilt or offshore tilt with depth. This inspection showed a high degree of variability, but identified more cases with greater shear on the onshore side than on the offshore side, which is consistent with observations (Dewey et. al., 1991; Huyer et al., 1991; Kosro et al., 1991) (see Figure 3.15), and just a slight tendency of offshore tilt with depth.

The tendency for the model jets to have greater positive vorticity and an offshore tilt was further investigated with east-west vertical sections of the three year mean model v-velocity (Figure 3.19). These sections provide only a partial representation of the actual jet because, as the jet meanders southward, its east-west location becomes more variable which tends to broaden and weaken its representation in a three year mean east-west section. Still, these sections support a model tendency towards greater positive vorticity, and a possible model tendency towards offshore tilt with depth. The creation of a composite (ensemble average) model jet would be required for a more accurate representation of the model jet.

variable	model	observations(ref)
core velocity (cm/s)	40-60	50-100 (1,2,3,5)
horizontal scale (km)	70-110	30-75 (2,3)
vertical scale (m)	250-350	125-200 (2,3,4)
location off C.M. (km)	110-190	150-200 (2,6)
on/off amplitude (km)	90-150	O(100-200) (1)
along wavelength (km)	O(200)	O(200) (2)
max vert. vel. (m/day)	O(10)	O(40) (1,4,5)
vorticity (1/s)	.1-.2f	.25-.35f (2,3,4)

Table 3.3. Comparison of model jet with observations.
(1) Brink et al., 1991; (2) Kosro et al., 1991; (3) Huyer et al., 1991; (4) Dewey et al., 1991; (5) Swensen et al., 1991., (6) Strub et al., 1991.

2.   Undercurrent

A poleward-flowing undercurrent of 10-20 cm/s, with a horizontal scale of 10-20 km, an axis at 150-250 meters, and located adjacent to the continental slope is typically observed during the summer season (Huyer et al., 1991; Huyer and Kosro, 1987). A poleward-flowing undercurrent with very different characteristics was produced in the model.

Three year mean sections of model v-velocity at various latitudes clearly shows a southward-flowing coastal jet and a poleward-flowing undercurrent (see Figure 3.19). The model undercurrent has core velocities of about 2 cm/s, a very deep axis at 1000-1500 meters, and a horizontal scale of about 60-80 km.

This simulated undercurrent is significantly weaker, broader, and deeper than observations (Huyer et al., 1991; Kosro et al., 1987). Vertical sections of average alongshore geostrophic currents from CTD data during spring and summer 1981 and 1982 is provided in Figure 3.20. A summary of the comparison of the model undercurrent with observations is provided in Table 3.4.

variable	model	observations
core velocity (cm/s)	2	10-20
horizontal scale (km)	60-80	10-20
depth of axis (m)	1000-1500	150-250

Table 3.4. Comparison of model undercurrent with observations (Huyer et. al., 1991; Kosro et. al. ,1987).

This discrepancy with observations suggests that the undercurrent is driven primarily by winds or (southern) boundary forcing, two forcing mechanisms that are excluded from this model simulation; and that the onshore geostrophic current, driven by the poleward pressure gradient due to the

differences between the north and south boundary conditions, is too weak to force enough downwelling along the coast to drive a stronger undercurrent. Therefore, even in the absence of wind forcing, an improvement for a future study would be to specify a poleward-flowing undercurrent at the southern boundary, in addition to the equatorward coastal jet imposed at the northern boundary.

a. Coastal Eddies

Figures 3.4a and 3.6d show the model fields of pressure with current vectors at 10 m depth on days 970 and 1610, respectively. There are closed eddies present in the pressure fields between 38°N and 39°N on both days (one cyclone and one anticyclone, respectively). Figure 3.21 shows two closed eddies (one cyclone and one anticyclone, respectively) observed during CODE. The model eddies have maximum velocities (taken from vertical sections) of about 30, 26, and 20 cm/s at 20, 80, and 150 m depth as opposed to about 50, 30, and 25 cm/s for the observed eddies at the same depths (Huyer and Kosro, 1987). The horizontal scale of the model eddies was determined by measuring the diameter of the eddy at its maximum tangential velocity. The horizontal scale of the observed eddies was estimated by inspection of surface current vectors. The model coastal eddies have a horizontal scale of 80-100 km, larger than observations of 40-80 km.

The vertical scale of the model eddies was taken as the depth where maximum tangential velocity had decreased from its surface value by a factor of $1/e$. The model eddies have a vertical scale of 250-500 m. This deep vertical scale is probably larger than that of the observed eddies, but the CODE observations were limited to depths of 150 m. At 150 m, the observed velocities have decreased to one-half of their near-surface value, indicating a somewhat larger vertical scale. On the other hand, the model eddies at 150 m have only decreased to two-thirds of their near-surface values.

30

For comparison purposes, the model eddies were limited to those located near the coast and early in their development. Fully-developed closed eddies located further offshore, such as those discussed in Section B of this chapter, have higher maximum velocities (40-60 cm/s) and a larger horizontal scale (80-170 km) than the coastal eddies. Vertical scales of 250-500 m are similar. A summary comparison of the model eddies versus CODE observations (Huyer and Kosro, 1987) is provided in Table 3.5.

variable	model	observations
max velocity at 20 m (cm/s)	30	50
max velocity at 80 m (cm/s)	26	30
max velocity at 150 m (cm/s)	20	25
horizontal scale (km)	80-100	40-80
vertical scale (meters)	250-500	>150

Table 3.5. Comparison of near-shore model eddies with observed eddies.

The analysis in this chapter indicates that the model produces mesoscale features that are generally consistent with the observations and the conceptual model for the California coastal zone. At 157 m depth offshore Point Arena, gradients of temperature are too strong, temperatures are too cold, and salinities are too high. The horizontal and vertical scales of the coastal jet, undercurrent, and coastal eddies are larger than observations while their intensities are smaller. Additionally, there is a long time scale variability with a time scale of about one year, suggested by the three year period analyzed (after allowing two years for the model to reach equilibrium).

31
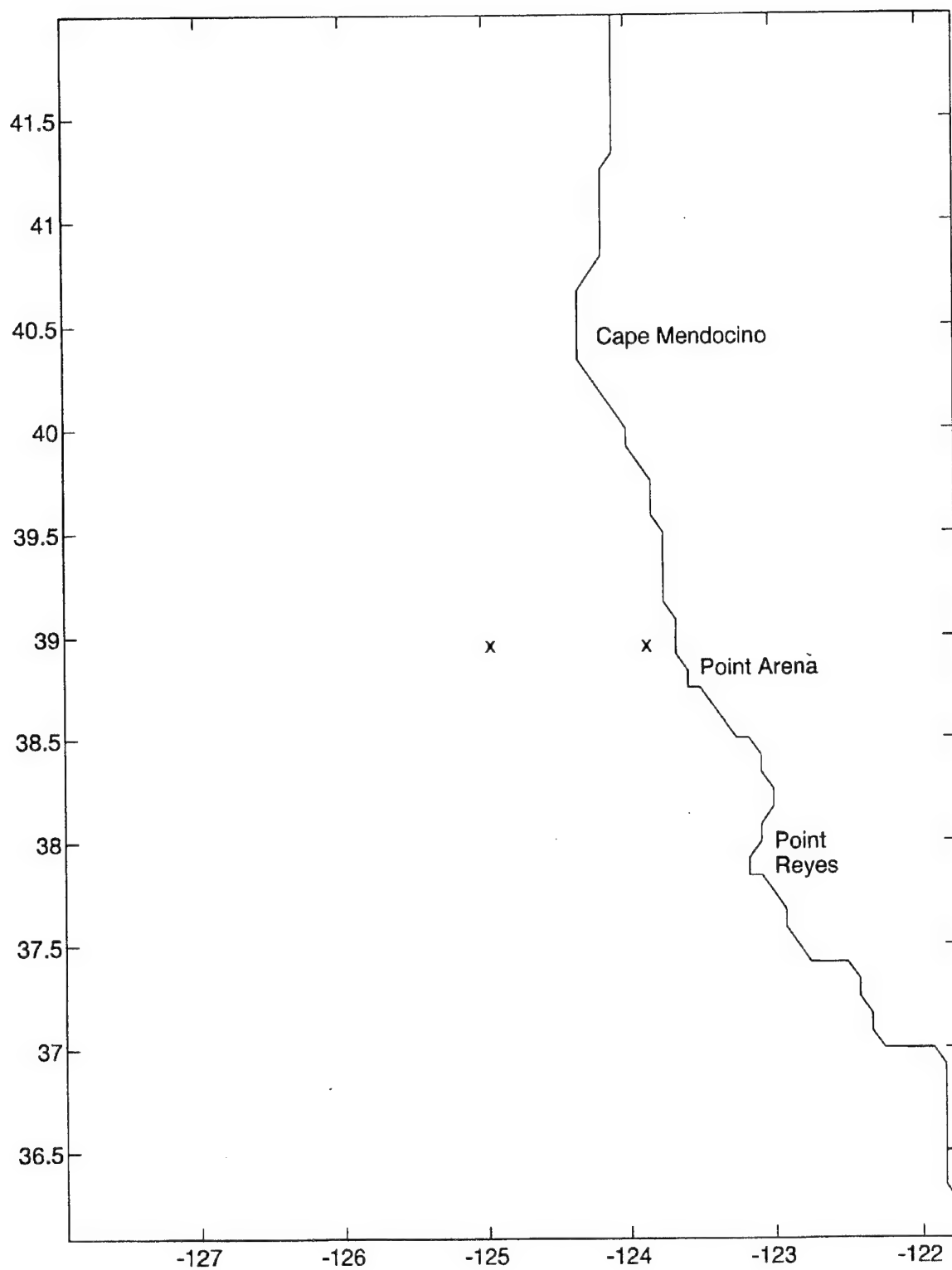
Figure 3.1. Locations for time series.
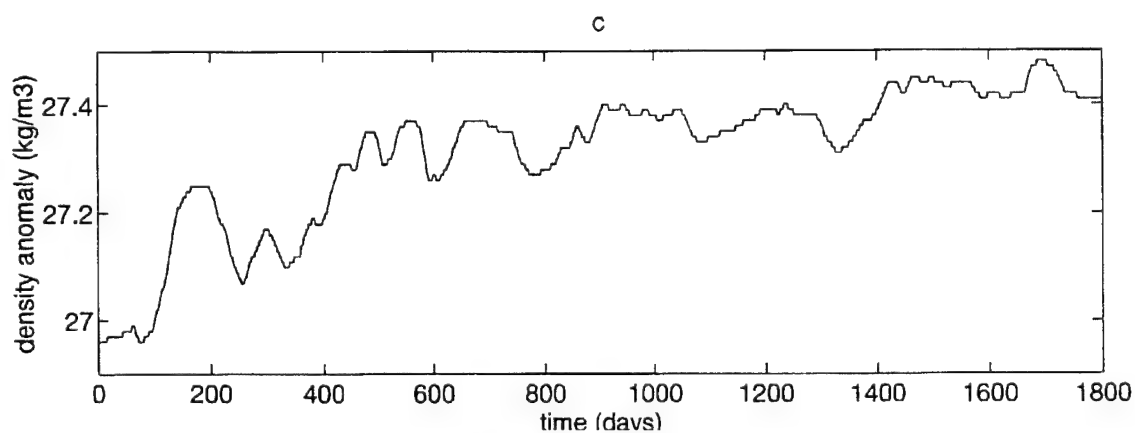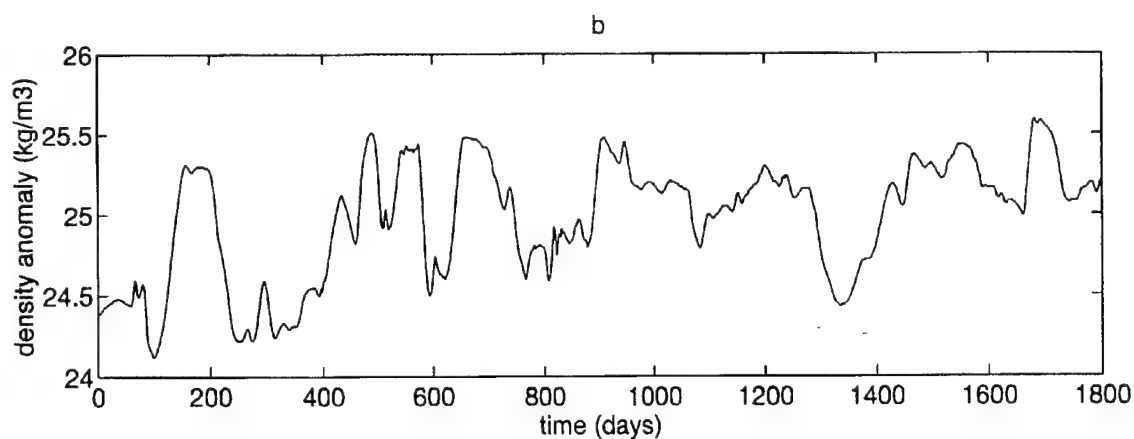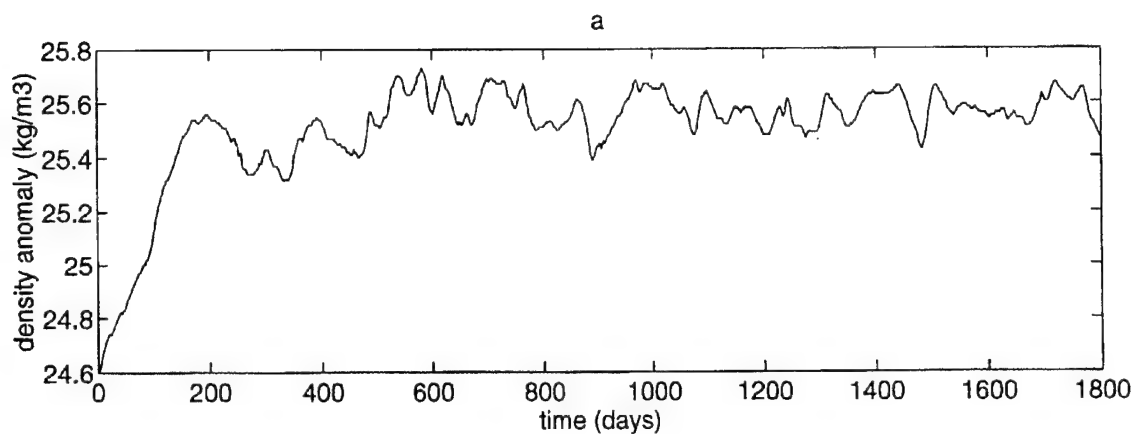
Figure 3.2. Time series of model density anomaly (kg/m^3) taken at locations shown in Figure 3.1: (a) inshore point at 10 m depth; (b) offshore point at 10 m depth; (c) offshore point at 491 m depth.
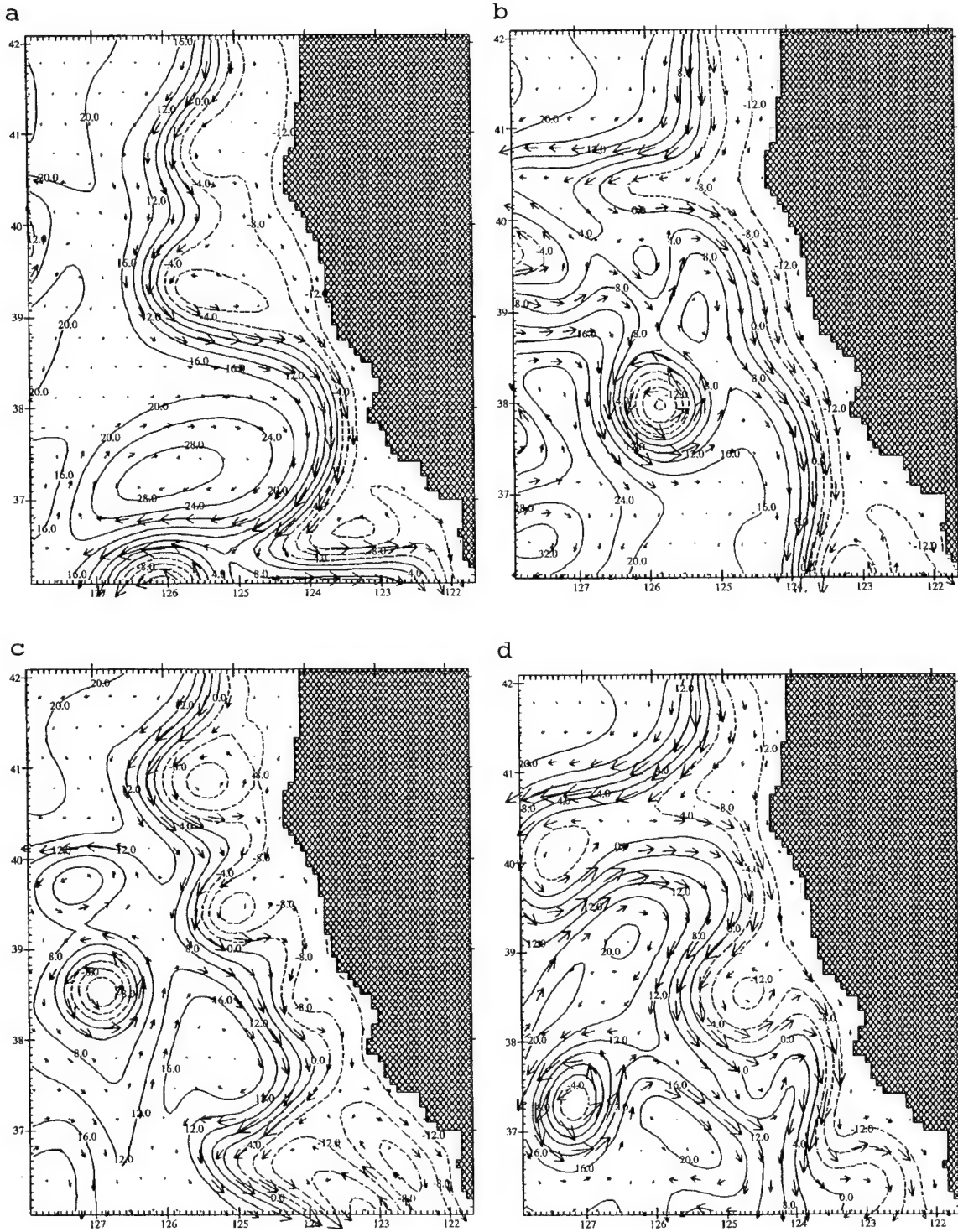
33
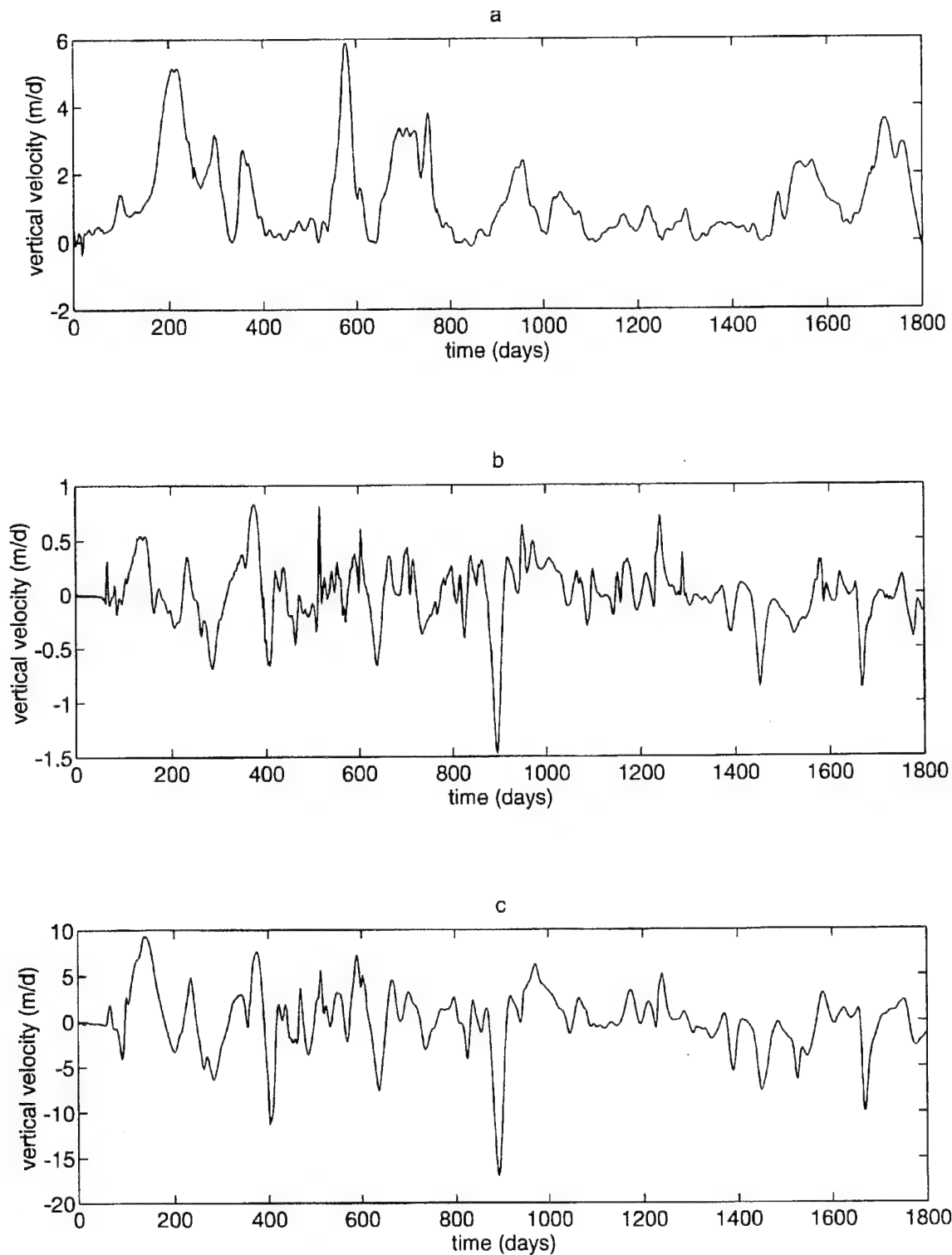
Figure 3.3. Time series of model vertical velocity (m/d) taken at locations shown in figure 3.1: (a) inshore point at 10 m depth; (b) offshore point at 10 m depth; (c) offshore point at 491 m depth.

34

Figure 3.4.   Fields of pressure (cm) at 10 m depth for days 722, 790, 880, and 970.
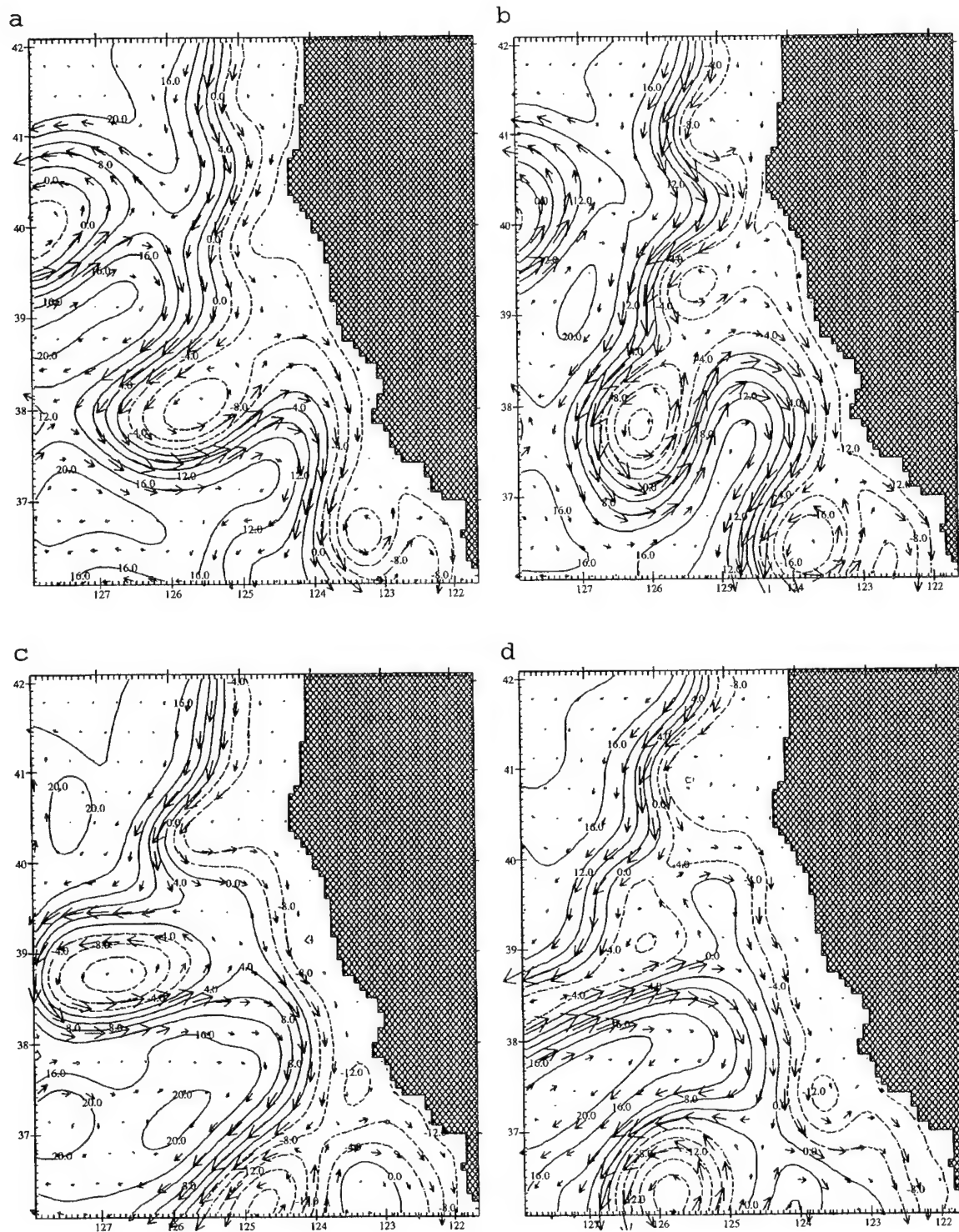
Figure 3.5.   Fields of pressure (cm) at 10 m depth for days
1025, 1050, 1090, and 1125.
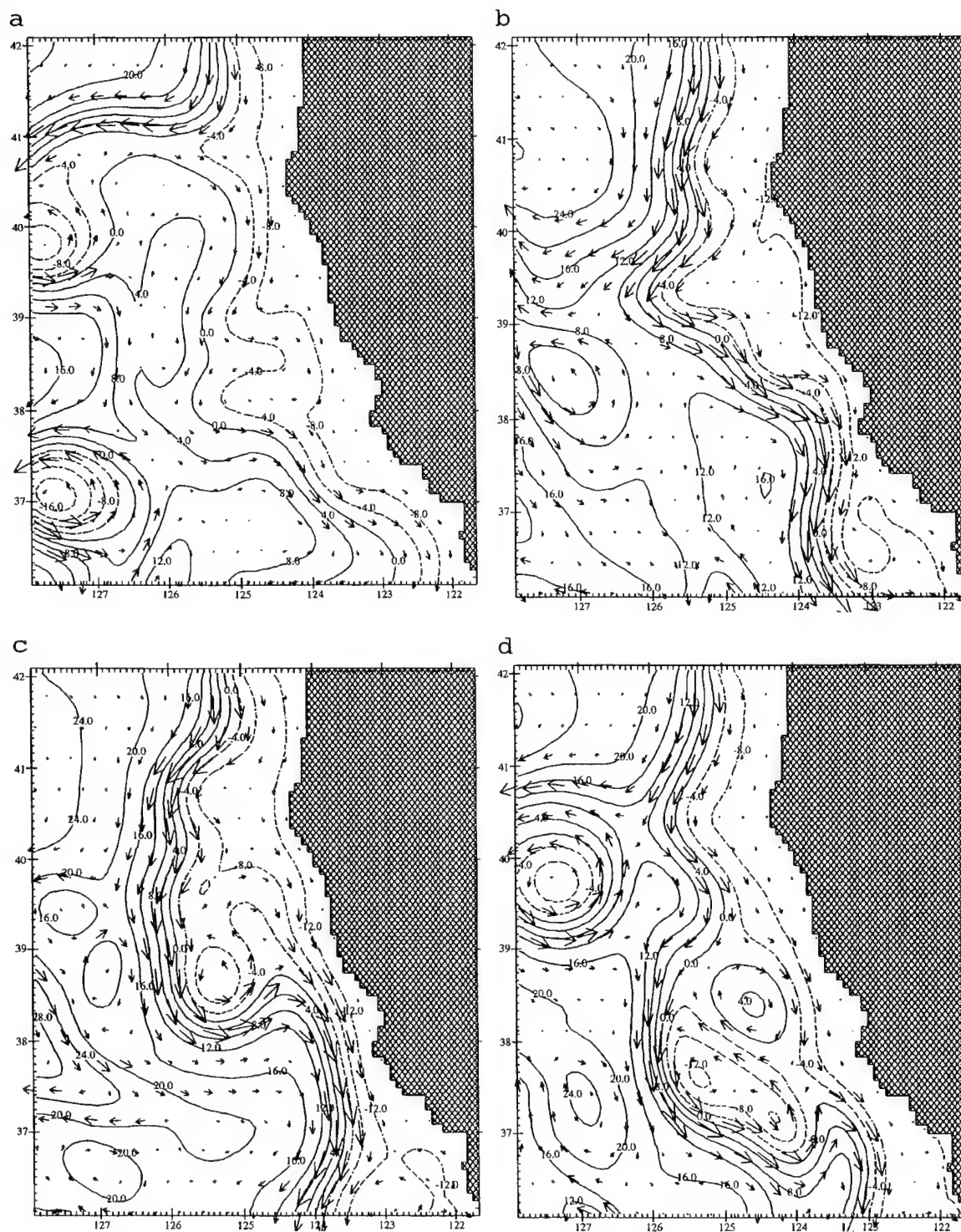
Figure 3.6. Fields of pressure (cm) at 10 m depth for days
1200, 1442, 1500, and 1610.

37
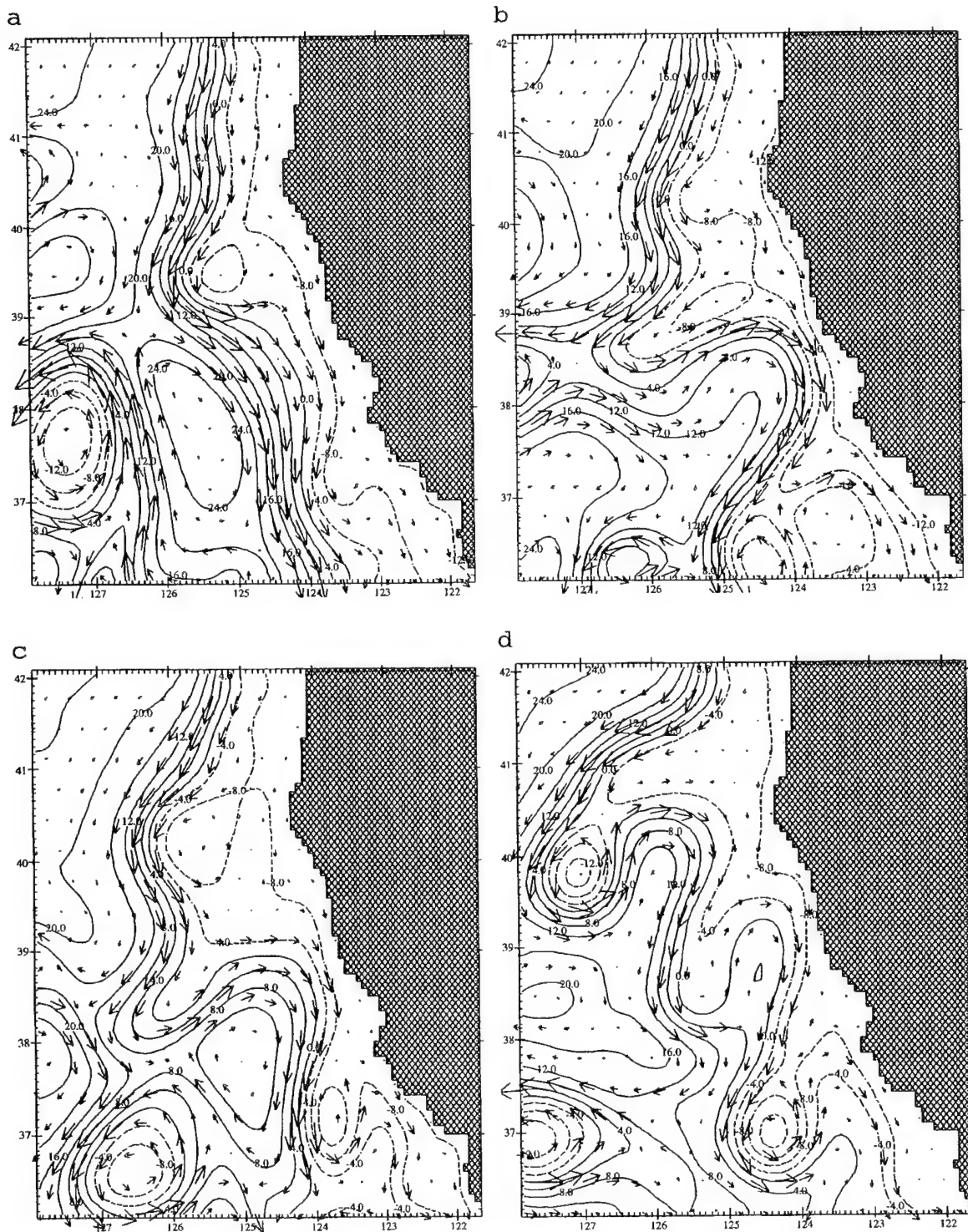
Figure 3.7.   Fields of pressure (cm) at 10 m depth for days
1660, 1720, 1760, and 1800.
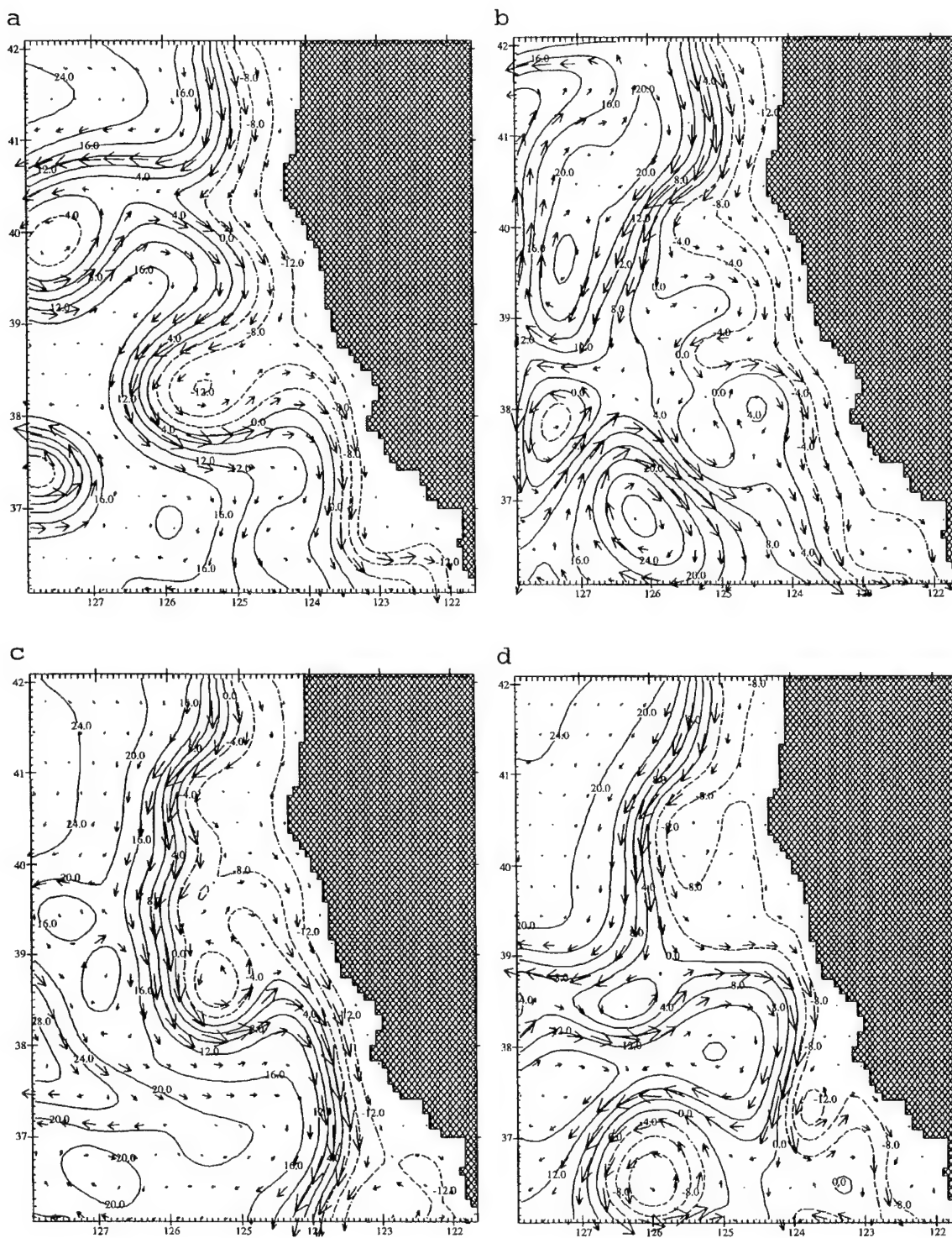
Figure 3.8. Fields of pressure (cm) at 10 m depth for days
1000, 1250, 1500 and 1750.

39
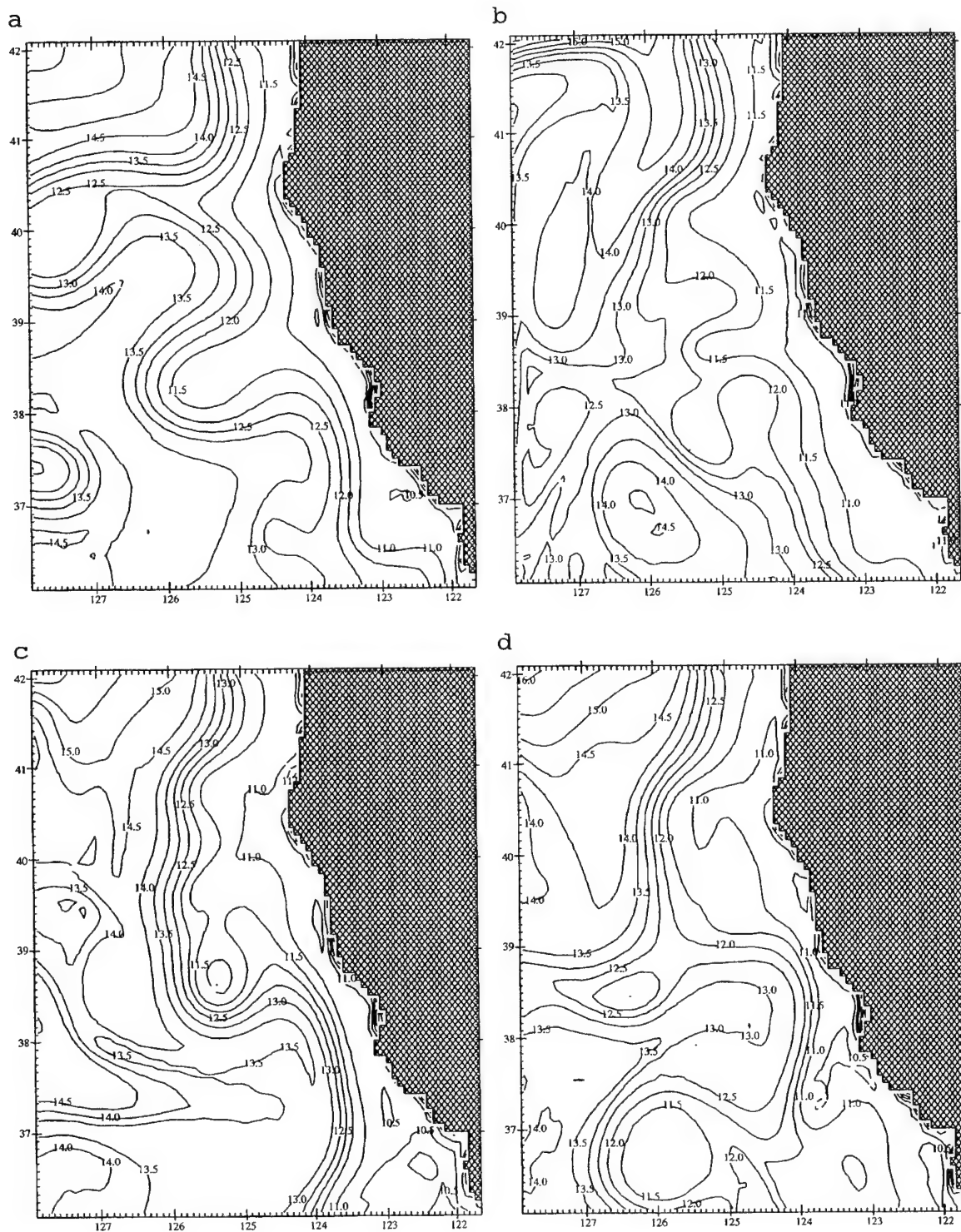
Figure 3.9. Fields of temperature (°C) at 10 m depth for days
1000, 1250, 1500, and 1750.
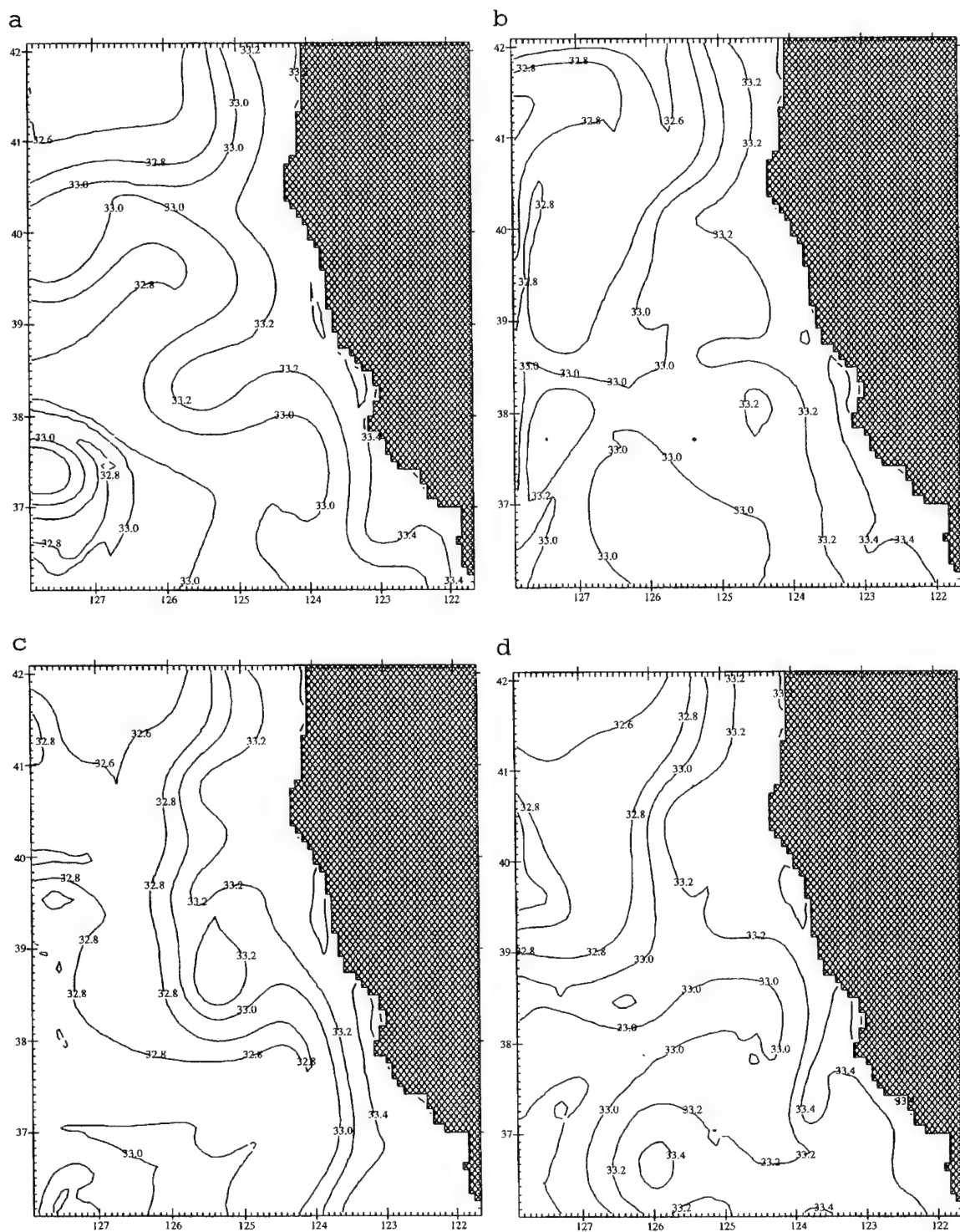
Figure 3.10. Fields of salinity (psu) at 10 m depth for days 1000, 1250, 1500, and 1750.

41
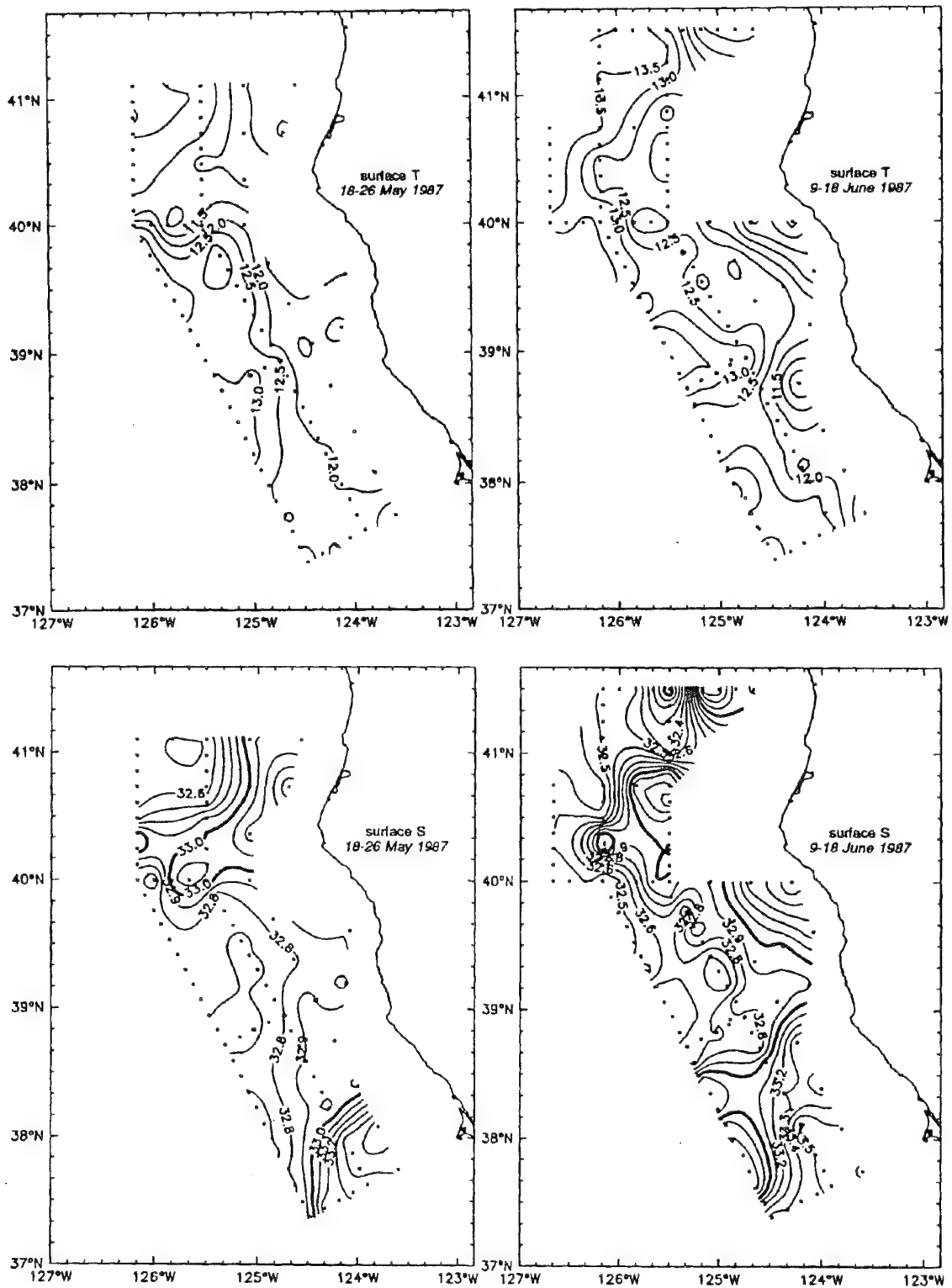
Figure 3.11. Observed fields of temperature (°C) and salinity (psu). (after Kosro et al., 1991)

42
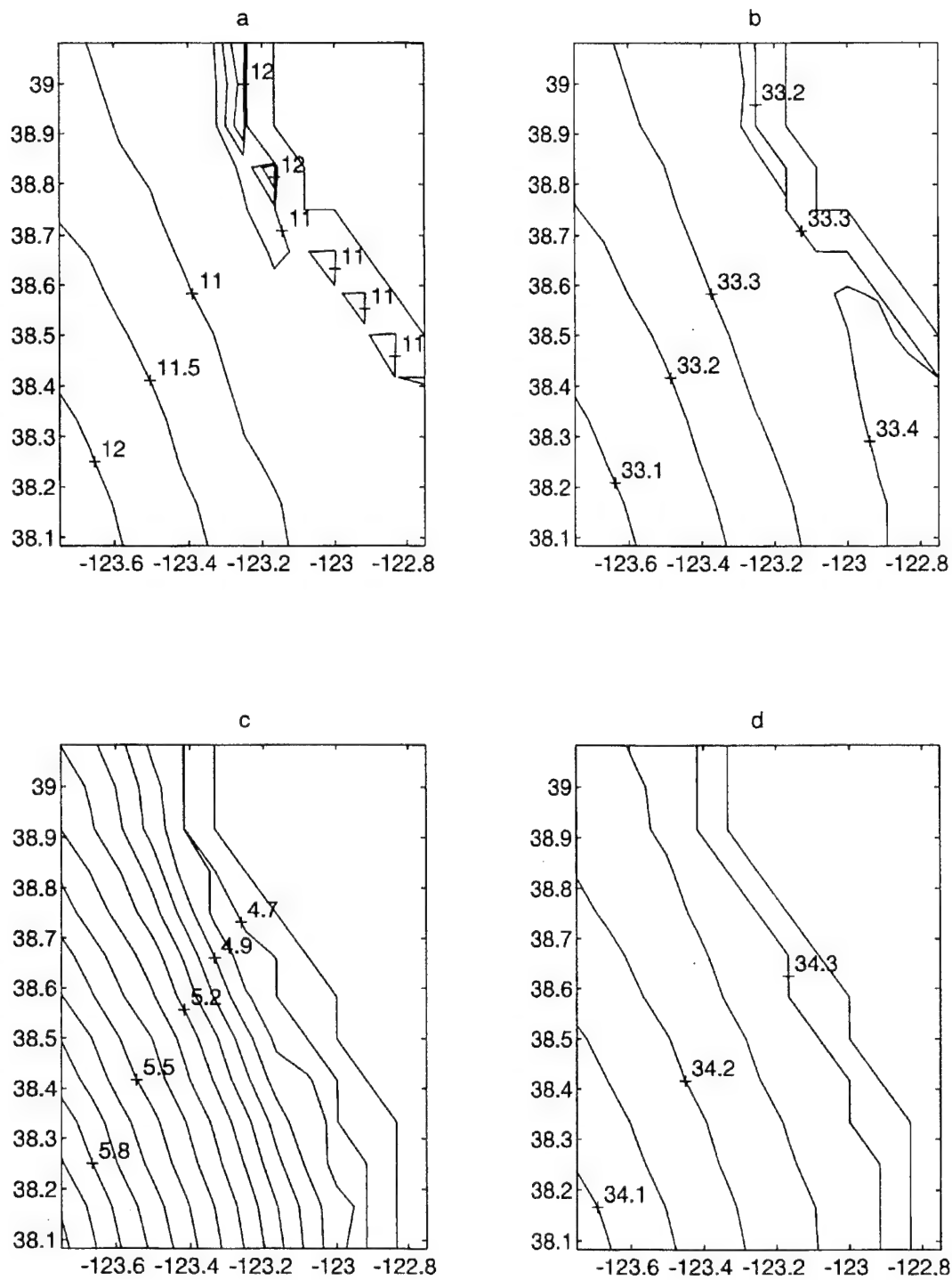
Figure 3.12. Mean model fields: (a) temperature (°C) at 10 m depth; (b) salinity (psu) at 10 m depth; (c) temperature (°C) at 157 m depth; (d) salinity (psu) at 157 m depth.
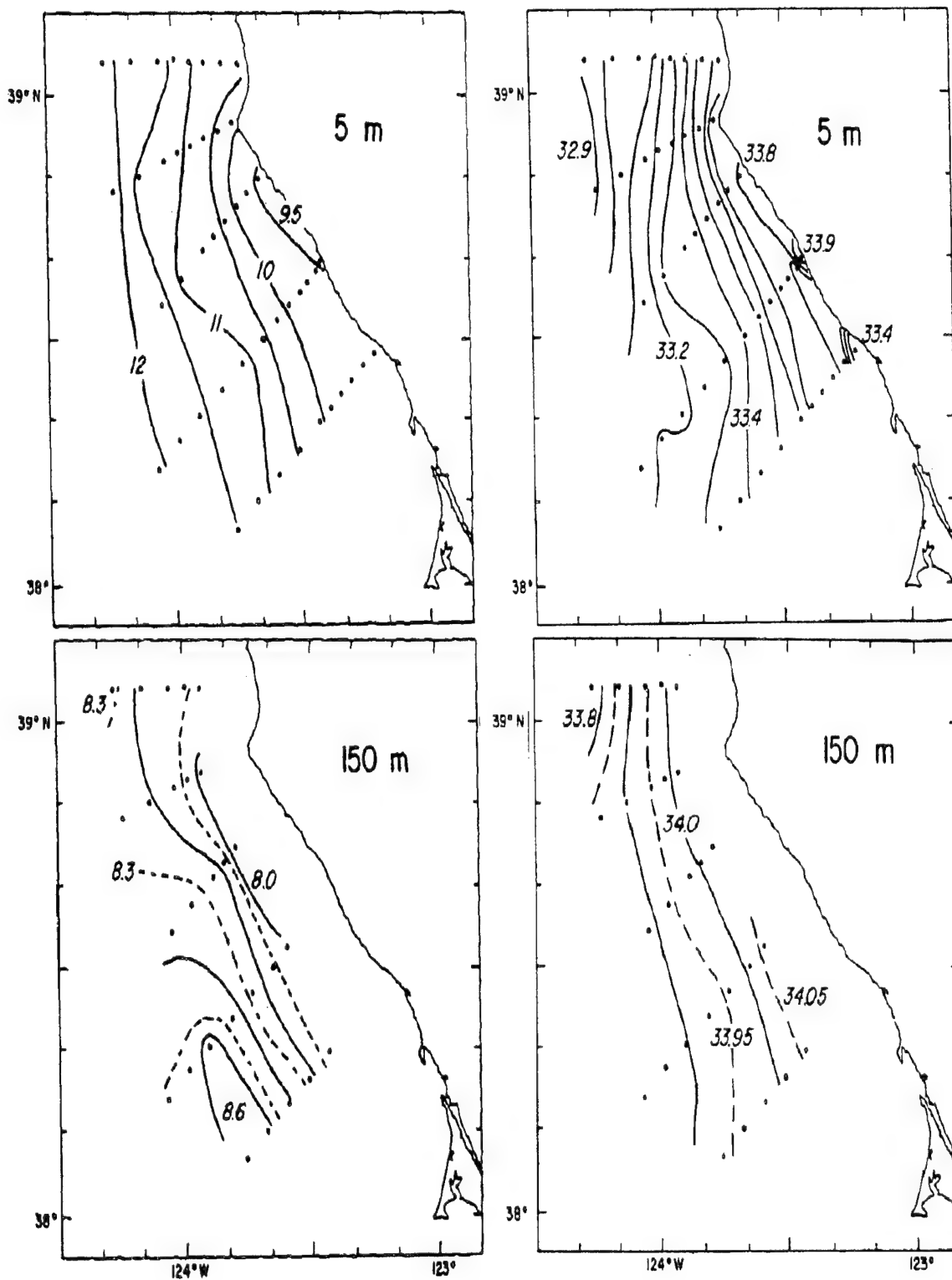
Figure 3.13. Mean observed fields: (left) temperature (°C)
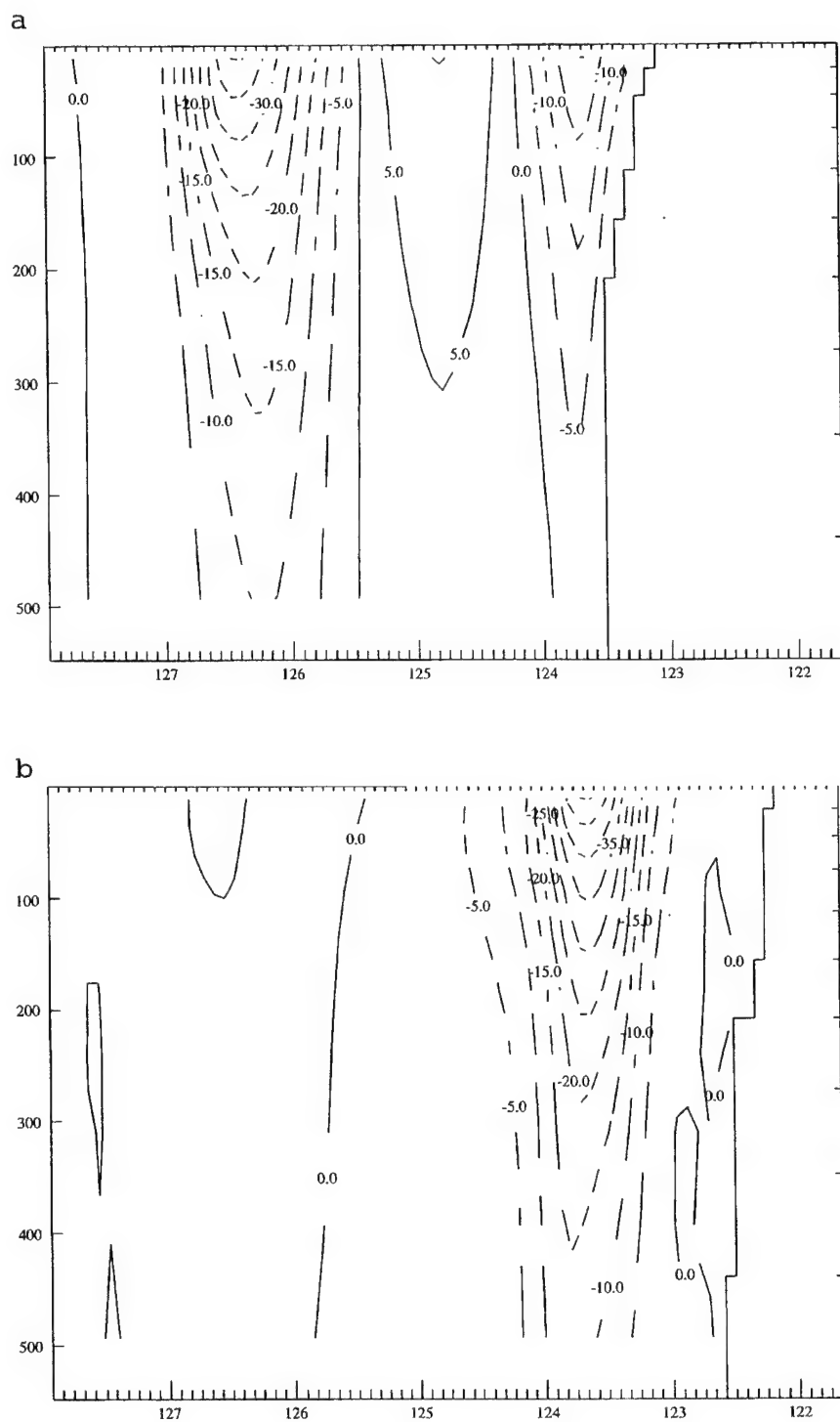and (right) salinity (psu), at 5 m and 150 m depth. (after
Huyer and Kosro, 1987)

44

Figure 3.14. Vertical sections of v-velocity (cm/s), depth is in m: (a) along latitude 38.3°N on day 1000; (b) along latitude 37.0°N on day 1500.
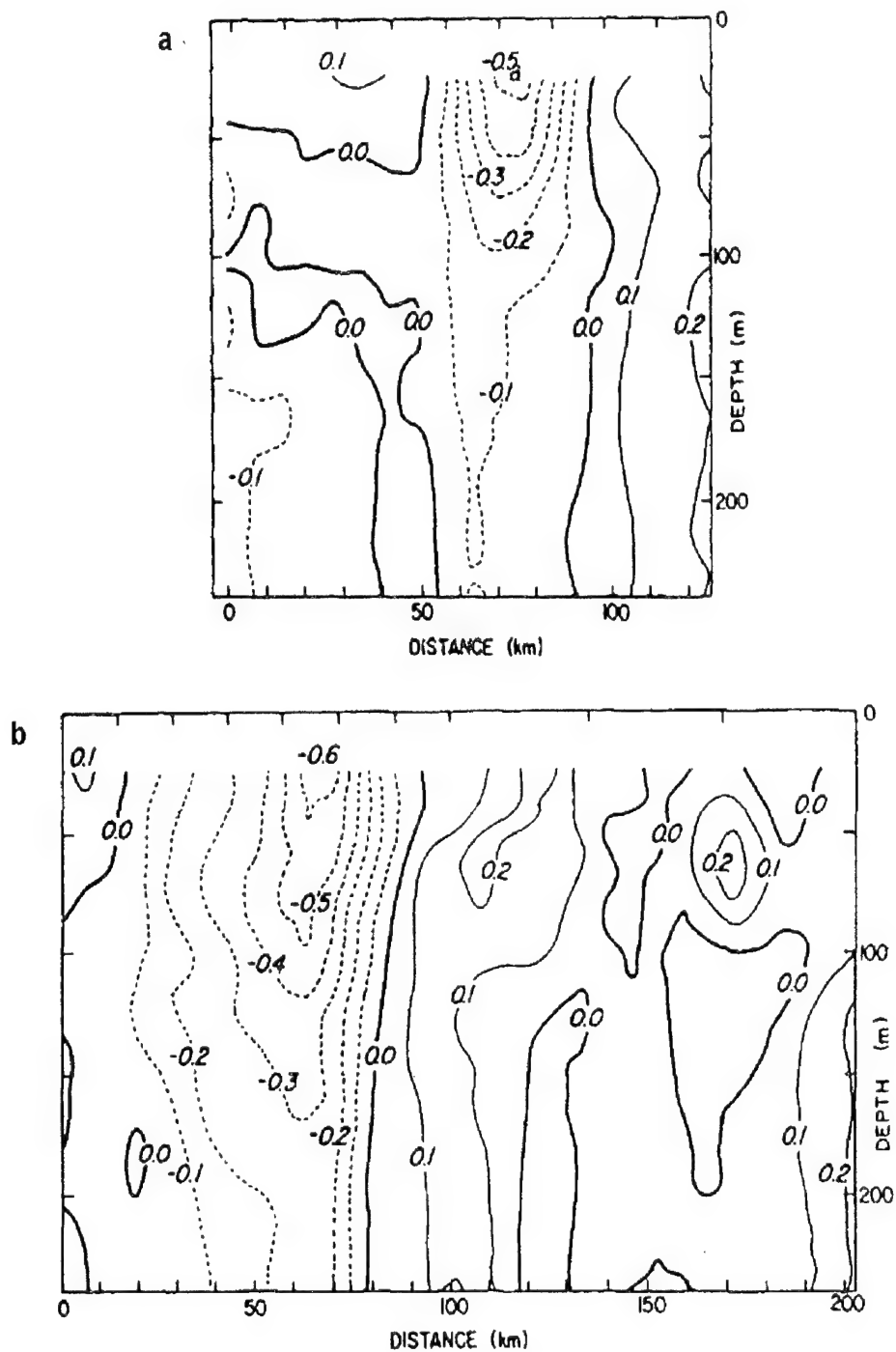
Figure 3.15. Vertical sections of observed v-velocity (cm/s) in June, 1987: (a) along latitude 41.5°N; (b) along latitude 40.0°N. East is on right. (after Kosro et al., 1991)
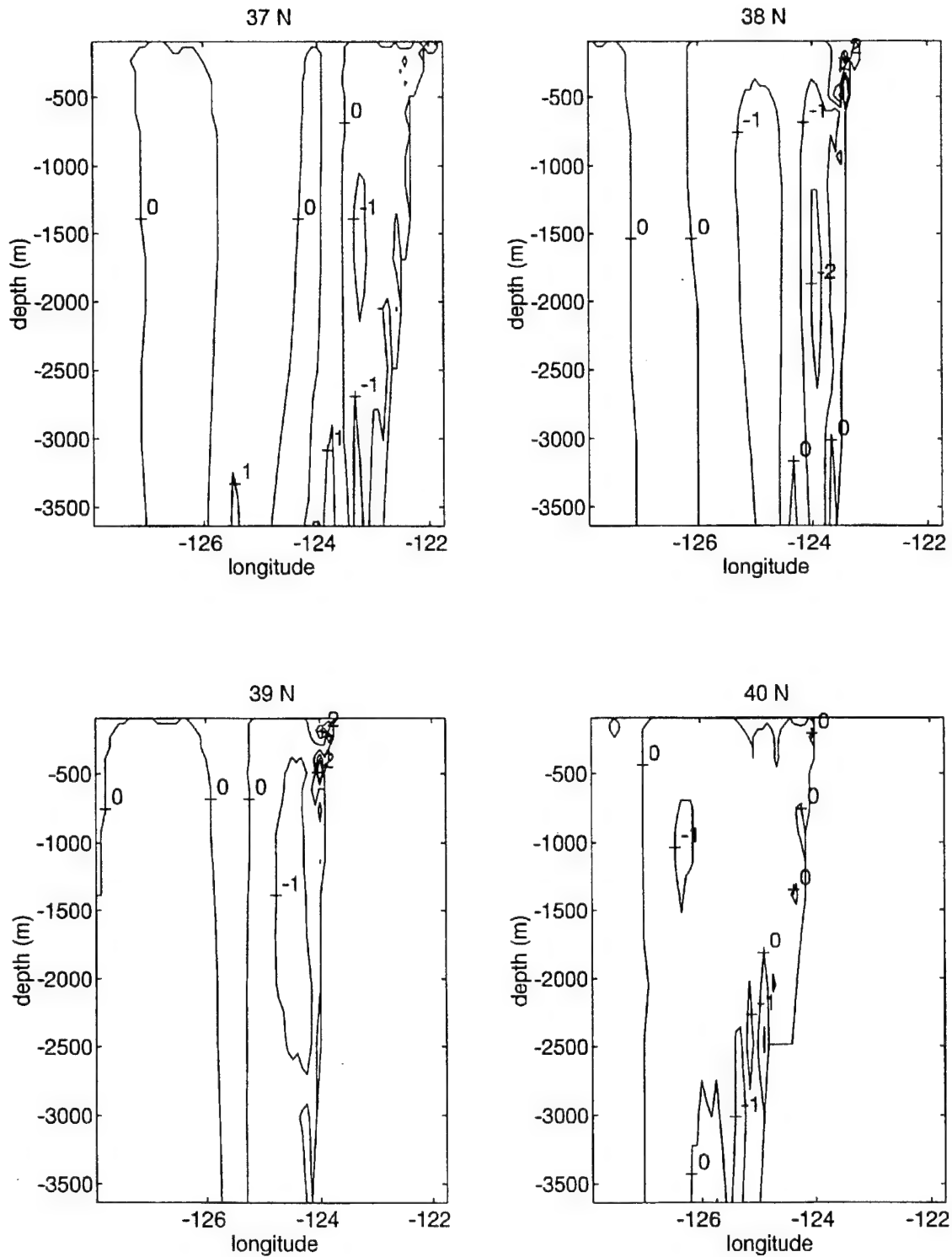
46

Figure 3.16. Vertical sections of mean model vertical velocity (m/d) along latitudes 37.0°N, 38.0°N, 39.0°N, and 40.0°N. Negative values represent upward motion, contour interval is 1.
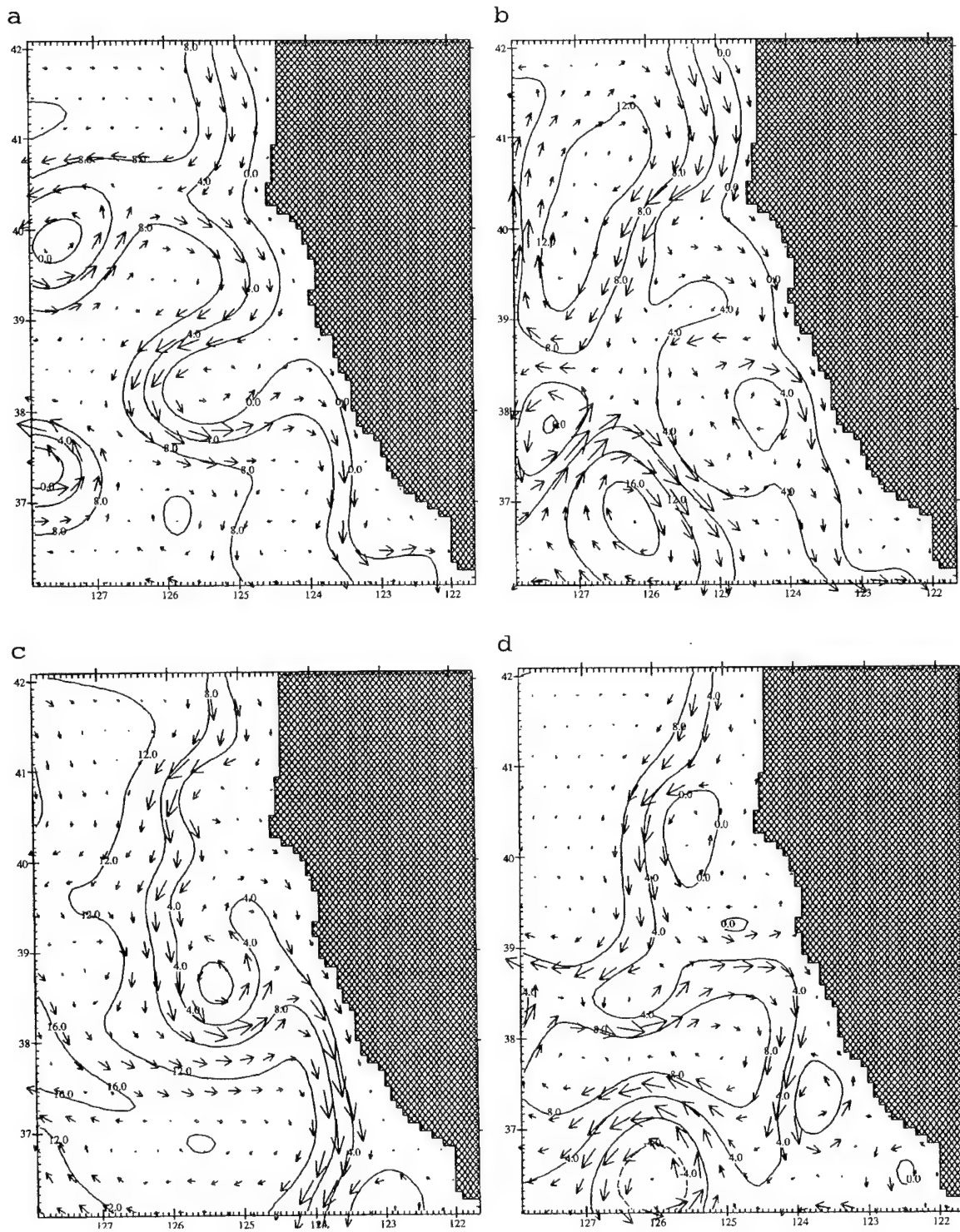
Figure 3.17. Fields of pressure (cm) at 239 m depth for days 1000, 1250, 1500, and 1750.
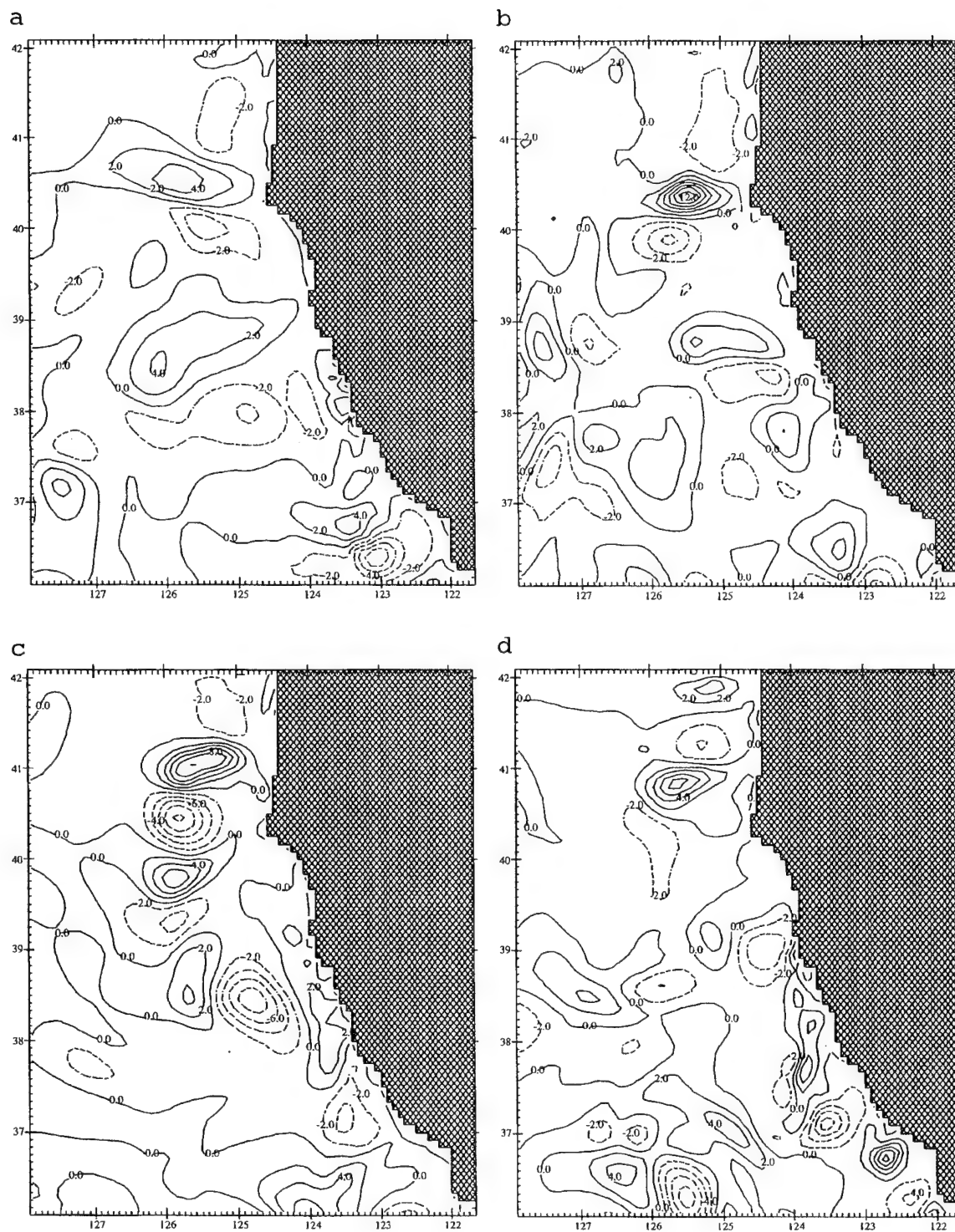
48

Figure 3.18.   Fields of vertical velocity (m/d) at 239 m depth
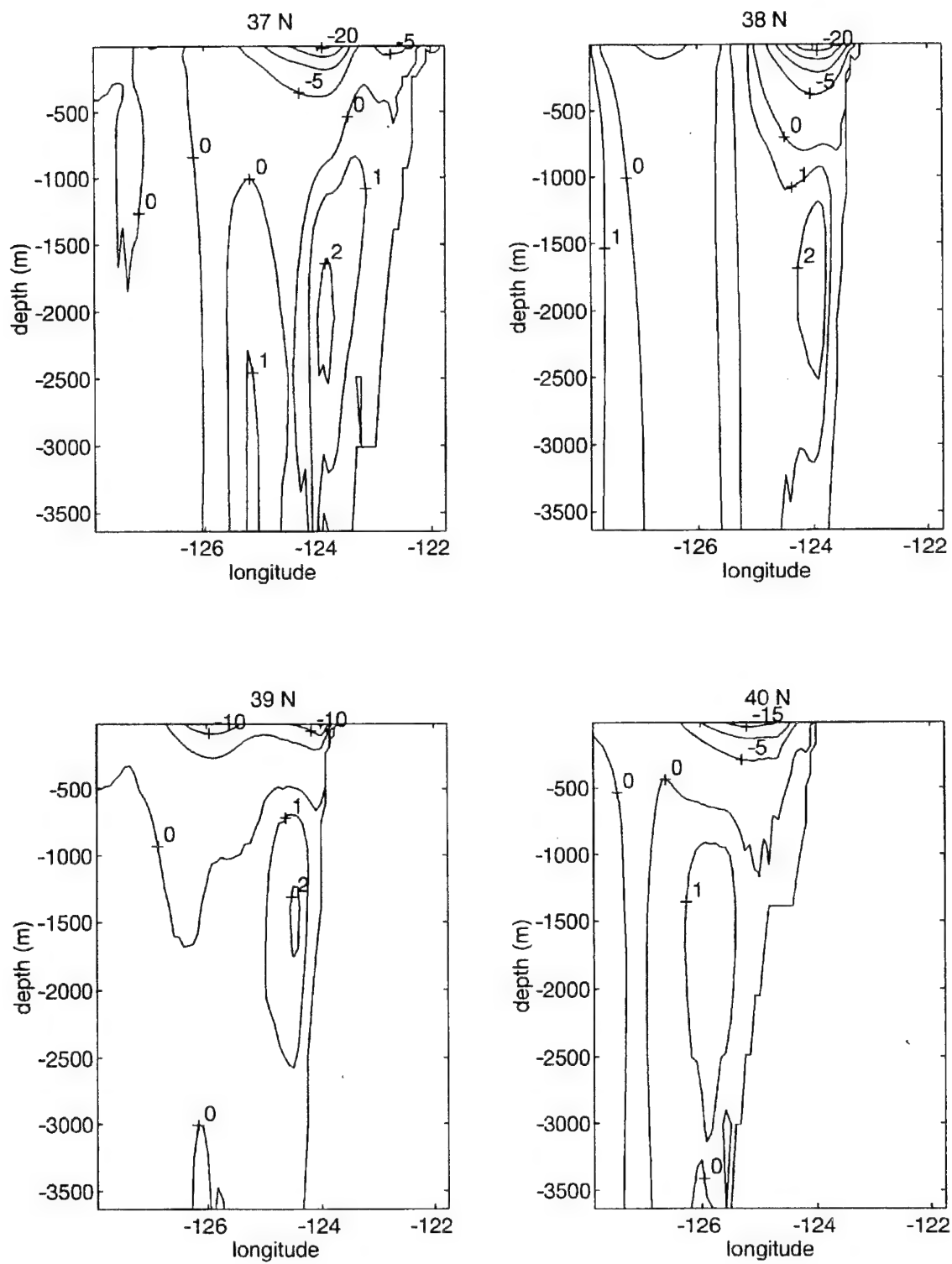for days 1000, 1250, 1500, and 1750.   Negative values
represent upward motion.

Figure 3.19. Vertical sections of mean model v-velocity (cm/s) along latitudes 37.0°N, 38.0°N, 39.0°N, and 40.0°N. Contour interval is 5 for negative velocities and 1 for positive velocities.
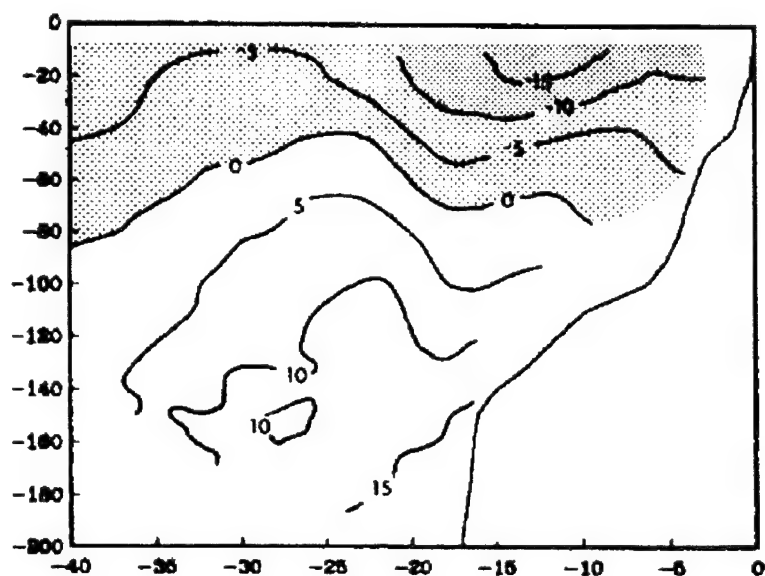
Figure 3.20. Vertical sections of mean alongshore geostrophic currents offshore of Point Arena from CTD data during spring and summer, 1981 and 1982. Horizontal axis indicates offshore distance in km. Vertical axis indicates depth in m. (after Kosro et al., 1987)
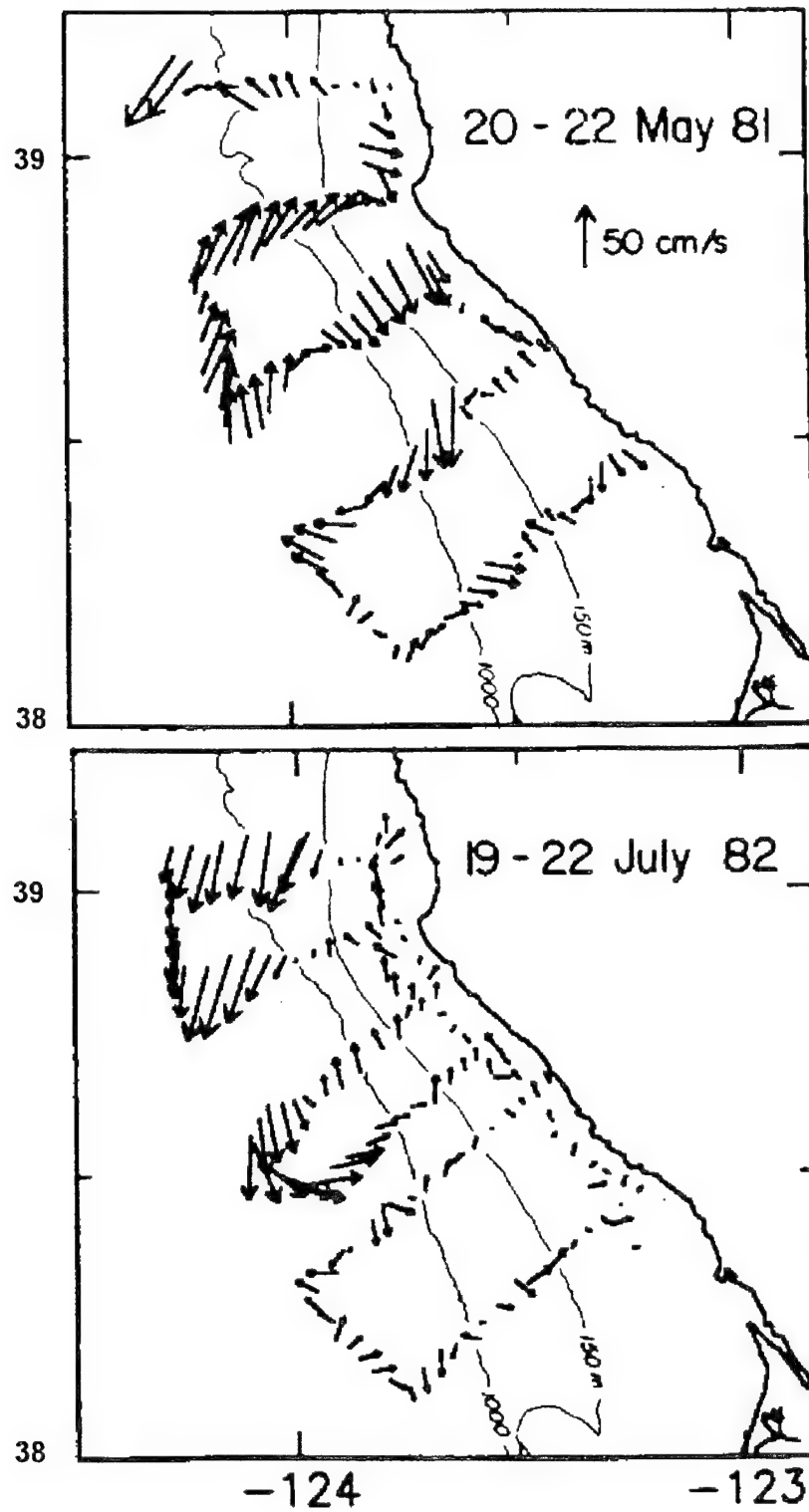
51

Figure 3.21. Maps of DAL (doppler acoustic log) current
vectors at 20 m depth. (after Huyer and Kosro, 1987)

IV. FREQUENCY OF CLOSED CYCLONES AND ANTICYCLONES

In order to study the number and location of cyclones and anticyclones formed in the model run, a program was designed to count the number of days a cyclone or anticyclone was present at each grid point for the entire three year run. The program was designed to count all cyclones and anticyclones or just those above a specified intensity level. This data was used to examine hypothesized relationships between cyclones/anticyclones and the model topography and three year mean pressure fields. This resulted in a large amount of data available for analysis. Comparisons were made between strong and weak cyclones and anticyclones, and between surface and subsurface cyclones and anticyclones. In conjunction with the time-space plots to be seen in Chapter V, these frequency plots should provide useful information on cyclone and anticyclone formation regions and propagation.

A. CYCLONE FREQUENCIES

The method used was to compare the pressure at each grid point with the pressure at each of the eight surrounding grid points. This is demonstrated in Figure 4.1. If this pressure is less than the pressure at every one of the eight surrounding grid points, then a cyclone (closed low pressure isobar) is identified and the cyclone counter for that grid point is advanced. This is done at every grid point in time increments of two days allowing for a possible maximum of 540 cyclone-days at each grid point (cyclone-days will be abbreviated to cyclones hereafter). It is important to note in this example that if the comparison is made with only the four surrounding grid points (to the north, south, and either side), a second cyclone could be counted where in fact there is only one. In Figure 4.1, a second false low of -12.48 cm, located southwest and adjacent to the low of -12.59 cm, would be counted as a second cyclone.

Initial runs of this program on the fields of pressure at 10 m depth produced plots where numerous small amplitude cyclones were being counted and showing up on the plots as an alternating pattern of noise in the meridional direction. One row(latitude) of grid points would have many cyclones and the adjacent row (to the north or south) would have none. This pattern was more evident in areas of the domain where pressure gradients were weak. The existence of small amplitude noise in the pressure field is not uncommon in primitive equation models. The use of higher order derivatives in the pressure gradient force has been suggested as a possible solution to this problem (Tafti, 1995). A two dimensional smoother was therefore applied to the pressure field to eliminate this noise from the cyclone frequencies.

1.   Surface Cyclones

Figure 4.2 is a plot of the number of cyclones counted at 10 m depth at each grid point for the three year period. A total of 2670 cyclones were counted. The contours run from one to ten in increments of one although there are a few points with as many as 15 cyclones. This is a fairly noisy field, with many peaks spread throughout the domain, although several larger scale clusters can be identified. The noisy nature of the data may be improved with an even longer model run, or a more complex requirement for identifying a cyclone.

To help in analyzing this data, a minimum cyclone intensity requirement was added to the program to allow only those cyclones above a specified intensity to be counted. This was accomplished by the additional requirement that the center pressure be at least a specified amount less than the average of the four surrounding pressures located above, below, and to either side of the grid point. Figure 4.3 shows the distribution of the number of cyclones at the surface as a function of this minimum intensity value. This shows that an intensity (difference between the grid-point value and the

average of the four surrounding grid-points) of 0.28 cm or greater would place the cyclone in the strongest one-third of all cyclones counted, while an intensity of 0.44 cm is required to place a cyclone in the strongest one-tenth. The median intensity is 0.225 cm. Using the geostrophic balance equations one can determine that a dynamic height difference of 0.1 cm over an eight kilometer grid distance results in a geostrophic current of 1.25 cm/s. Thus, the median cyclone at the surface has a geostrophic current near its center of 2.8 cm/s. Assuming gradient balance instead of geostrophic balance increases the median cyclone's current at the center to 3 cm/s.

The one-third strongest cyclones were counted and contoured over the three year mean pressure field (Figure 4.4). This figure suggests three groups of strong cyclones related to Cape Mendocino, Point Arena, and Point Reyes, respectively. It is apparent that these three groups of strong cyclones are associated with the pressure trough axes extending offshore of the three coastal capes. An alternate interpretation would be that these strong cyclones are producing the troughs in the mean pressure fields. In any case, there are no strong cyclones near the coast. This suggests that the strongest cyclones originate from offshore meanders of the unstable coastal jet, or that the cyclones originate near shore and only acquire sufficient intensity (to be counted as a strong cyclone) when they reach the offshore location. A more sophisticated cyclone tracking system would be needed to investigate this result further.

The one-third weakest cyclones were counted and contoured over the three year mean field of pressure at 10 m depth (Figures 4.5). These weak cyclone patterns are distinctly different from the strong cyclones in that they are concentrated along the coast. The one-tenth weakest cyclones provide an even stronger signal, being found almost

exclusively along the coast and well inshore of the coastal jet (see Figures 4.6). This suggests that the weak cyclones do not result from instabilities in the coastal jet, but are simply due to the trough of low pressure at the coast where grid-points will frequently satisfy the criteria for a "low" pressure center. Several isolated groups of these very weak cyclones located along the coast can be seen on the plot of all cyclones (Figure 4.2), separate from the stronger cyclones extending offshore. This suggests that many weak cyclones formed near the coast do not propagate offshore and intensify, but are simply due to the existence of weak along-shore variations in pressure at the coast where the mean pressure is generally a minimum.

2. Subsurface Cyclones

Cyclones were counted at each model level and plotted as a function of model level in Figure 4.7a. The number of cyclones increases with depth from 2670 at the surface to 4248 at level 18 (2487 m) with most of the increase occurring below level 16 (1690 m). The number of cyclones then decreases from level 18 down to level 20 (3639 m) which coincides with a sharp reduction in the ocean area below level 18. The increase of cyclones from level 15 to 18 indicates that there are many deep cyclones that do not extend to the surface. For example, more than one-third of the cyclones at level 18 are not present at the surface.

Still, the increase in the number of cyclones with depth is small down through level 16 (1690 m), with most of the increase occurring at level 17 (2052 m) and below. As a first order approximation, the number of cyclones may be described as constant throughout most of the water column with a sharp increase limited to deep ocean areas. Plots of all cyclones and of the one-third strongest and weakest cyclones at level 12 (756 m) show patterns similar to those seen at 10 m depth (see Figures 4.8-4.10, respectively).

56

A measure of the individual cyclone intensity was calculated by subtracting the center pressure from the average of the four surrounding grid point pressures. The average intensity was then calculated by summing all the intensities for the entire model run and dividing by the total number of cyclones. This was performed at each level with the results plotted in Figure 4.7b. Cyclone intensities decrease steadily with depth down to model level 18 and then show a slight increase through level 20. The decrease in eddy intensity with depth down to level 17 is consistent with observations (Huyer et al., 1991).

The increase in the number and intensity of cyclones at the deepest three levels is particularly significant because it indicates the existence of a group of cyclones separate from those above. The surface cyclones have their maximum intensity at the surface. The cyclones at the deepest three levels have their maximum intensity at the bottom and therefore must be topographically-forced. Level 17 is the level of minimum cyclone intensity and therefore indicates the level below which topographically-forced cyclones dominate, and the level above which surface cyclones dominate.

B. ANTICYCLONE FREQUENCY

1. *Surface Anticyclones*

Figure 4.11 is a plot of the number of anticyclones counted at each grid point at 10 m depth for the three year period. As was the case for cyclones, the fields are fairly noisy with many individual peaks among several larger scale clusters. A total of 2139 anticyclones were counted for the entire model run as compared to the 2670 cyclones for the same run. Figure 4.12 shows the distribution of the number of anticyclones as a function of the minimum intensity. Compared to the distribution for cyclones (Figure 4.3), this shows that the number of anticyclones falls off more rapidly than did the

57

number of cyclones. Additionally, the median anticyclone is only half as intense as the median cyclone (0.11 cm verses 0.23 cm). This simply reflects the fact that the pressure gradient is weaker near the center of highs than near the center of lows.

The strongest anticyclones are plotted over the three year mean field of pressure at 10 m depth in Figure 4.13. A pattern complementary to that of the strongest cyclones is seen, with strong anticyclones located in the pressure ridges, whereas the strong cyclones are located in the pressure troughs.

The difference between the strong and weak anticyclones is not as evident as the difference between strong and weak cyclones. There is still a tendency for the weak anticyclones to be located near the coast, but they are also found throughout the domain, including the ridges where the stronger anticyclones are located (see Figure 4.14).

2. Subsurface Anticyclones

Anticyclones were counted at each level and plotted as a function of level in Figure 4.15a. As with cyclones, the number of anticyclones increases with depth but to an even larger degree. There are 2139 anticyclones at 10 m with an increase to 4427 by level 18. This increase of 106 percent is much larger than the 59 percent increase for the cyclones. The number of anticyclones stays approximately constant down to level 9 (391 meters), at which point it increases in a fairly steady manner to its maximum at level 18 (2487 meters). This stronger increase occurs at shallower depths than the increase for the cyclones. Anticyclone intensity falls off with depth through level 17, and then increases with depth to the bottom, as is the case for the cyclones seen earlier (see Figure 4.15b).

To further study this increase in anticyclones with depth, all anticyclones and the one-third strongest and

58

weakest anticyclones at level 12 (756 m) are plotted over the mean field of pressure in Figures 4.16-4.18, respectively. At this level there are 3174 anticyclones, an increase of 48 percent over the near surface count of 2139.

When compared to the same plots at 10 m depth (Figures 4.11, 4.13, and 4.14, respectively), it is evident that much of the increase is accounted for in the region along the coast and adjacent to and north of the Cape Mendocino escarpment. Within this region there are many strong and weak anticyclones in the pressure ridge located along 41.0°N, a group of exclusively strong anticyclones located just north of the low pressure center immediately north of the escarpment, and a group of exclusively weak anticyclones located over the slope near the northern boundary. There is also a large band of strong anticyclones, associated with a tight pressure gradient, located just south and east of the low pressure center off Point Arena near the center of the domain. With the exception of this band, and the group north of the escarpment described above, the strong anticyclones at level 12 have tendencies similar to the strong anticyclones at the surface.

There is a significant difference between the weak anticyclones at 756 m depth and those at 10 m depth. While the weak anticyclones were fairly well spread throughout the domain at the surface, the deeper ones are concentrated along the topography along the coast and north of the escarpment. Since most of the weakest anticyclones at depth are located in regions of pressure maxima along the coast, they are probably not significant features and are largely due to minor pressure fluctuations along the axis of high pressure.

As with cyclones, the increase in the number and intensity of anticyclones at the deepest levels indicates the existence of a separate group of topographically-forced anticyclones (see Figure 4.15). As with cyclones, level 17 is

the level of minimum anticyclone intensity and indicates the level below which topographically-forced anticyclones dominate and above which surface anticyclones dominate.

The combined number of cyclones and anticyclones present at 10 m depth in the southern half of the domain (south of 39.0°N) is about twice the number in the northern half. A total of 1699 surface cyclones and 1545 surface anticyclones were counted in the southern half, versus 971 surface cyclones and 594 surface anticyclones in the northern half of the domain. At level 10 (491 m) there are a total of 1750 cyclones and 1381 anticyclones in the southern half, versus 1445 cyclones and 1109 anticyclones in the northern half of the domain. This is consistent with the observation that eddies are more dominant south of 39.0°N (Strub et al., 1991). Taking into account an approximately 50 percent greater ocean area in the southern half, there is about one-third more cyclones and anticyclones per unit area at 10 m depth in the southern half, than in the northern half. At level 10, the relationship is reversed with about 20 percent more cyclones and anticyclones in the northern half than in the southern half.

The cyclone/anticyclone frequency plots provide several interesting patterns and tendencies. The stronger cyclones are generally located along the mean pressure troughs, while the stronger anticyclones, which are about half as intense as the cyclones, are generally located along the mean pressure ridges. Thus, the presence of strong cyclones and anticyclones are apparent in the mean pressure fields. The weaker cyclones at the surface are generally located close to the coast in the pressure trough there, while the weaker anticyclones are spread more evenly throughout the domain.

Both cyclones and anticyclones increase in number with depth, with the anticyclones showing a stronger increase. The weak anticyclones at depth are primarily located in the

60

pressure ridge along the coast. Both cyclones and anticyclones decrease in intensity with depth down to about 2000 m. Intensities then increase with depth to the bottom, indicating the existence of a separate group of topographically-forced cyclones and anticyclones that are dominant below 2000 m.

```
  8.280    6.132    3.918    1.729   -0.343   -2.215   -3.823   -5.129   -6.127

  6.406    3.999    1.601   -0.685   -2.760   -4.547   -5.999   -7.102   -7.875

  4.028    1.421   -1.070   -3.338   -5.296   -6.886   -8.091   -8.925   -9.431

  1.306   -1.398   -3.858   -5.982   -7.707   -9.013   -9.912  -10.445  -10.663

 -1.531   -4.200   -6.498   -8.364   -9.777  -10.751  -11.323  -11.546  -11.474

 -4.218   -6.722   -8.751  -10.288  -11.353  -11.985  -12.231  -12.143  -11.775
                                              *******
 -6.447   -8.695  -10.401  -11.589  -12.304  -12.595  -12.511  -12.104  -11.427
                                              *******
 -7.919   -9.878  -11.256  -12.103  -12.475  -12.425  -12.003  -11.266  -10.273

 -8.369  -10.051  -11.125  -11.653  -11.697  -11.314  -10.564   -9.515   -8.237

 -7.531   -8.971   -9.783  -10.033   -9.791   -9.126   -8.112   -6.828   -5.358

 -5.236   -6.472   -7.083   -7.134   -6.703   -5.870   -4.722   -3.347   -1.835

 -1.632   -2.702   -3.190   -3.154   -2.672   -1.829   -0.714    0.579    1.962
```

Figure 4.1. Example pressure (cm) field showing how a cyclone
is identified when determining cyclone frequencies. The grid
point indicated has a pressure of -12.595 cm, which is less
than the surrounding eight grid points, and would therefore
advance a cyclone counter for that grid point on that day.
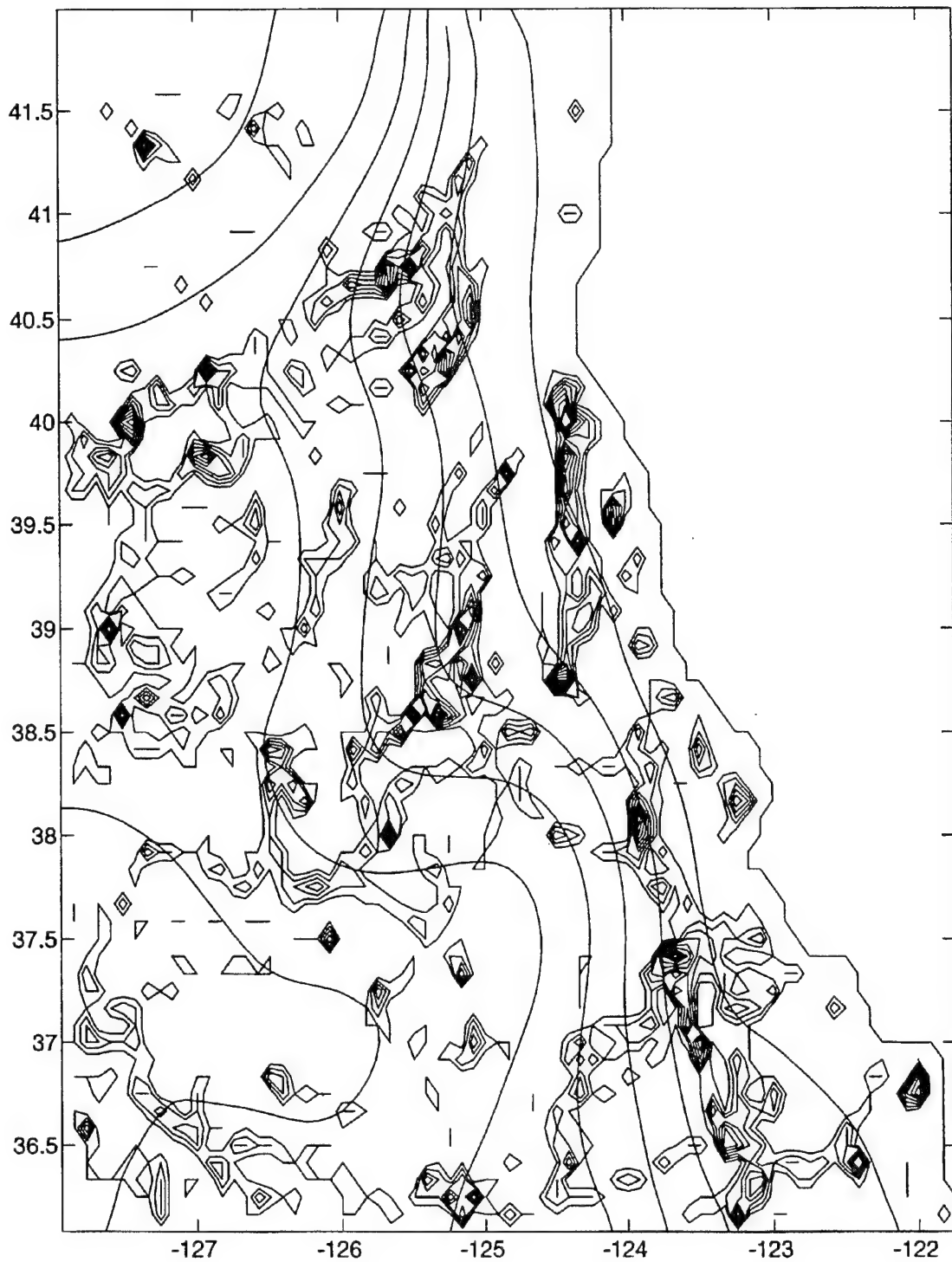
Figure 4.2.   Fields of cyclone frequency (cyclone-days) at 10 m depth with a contour interval of 1, and mean pressure (cm) with a contour interval of 5.
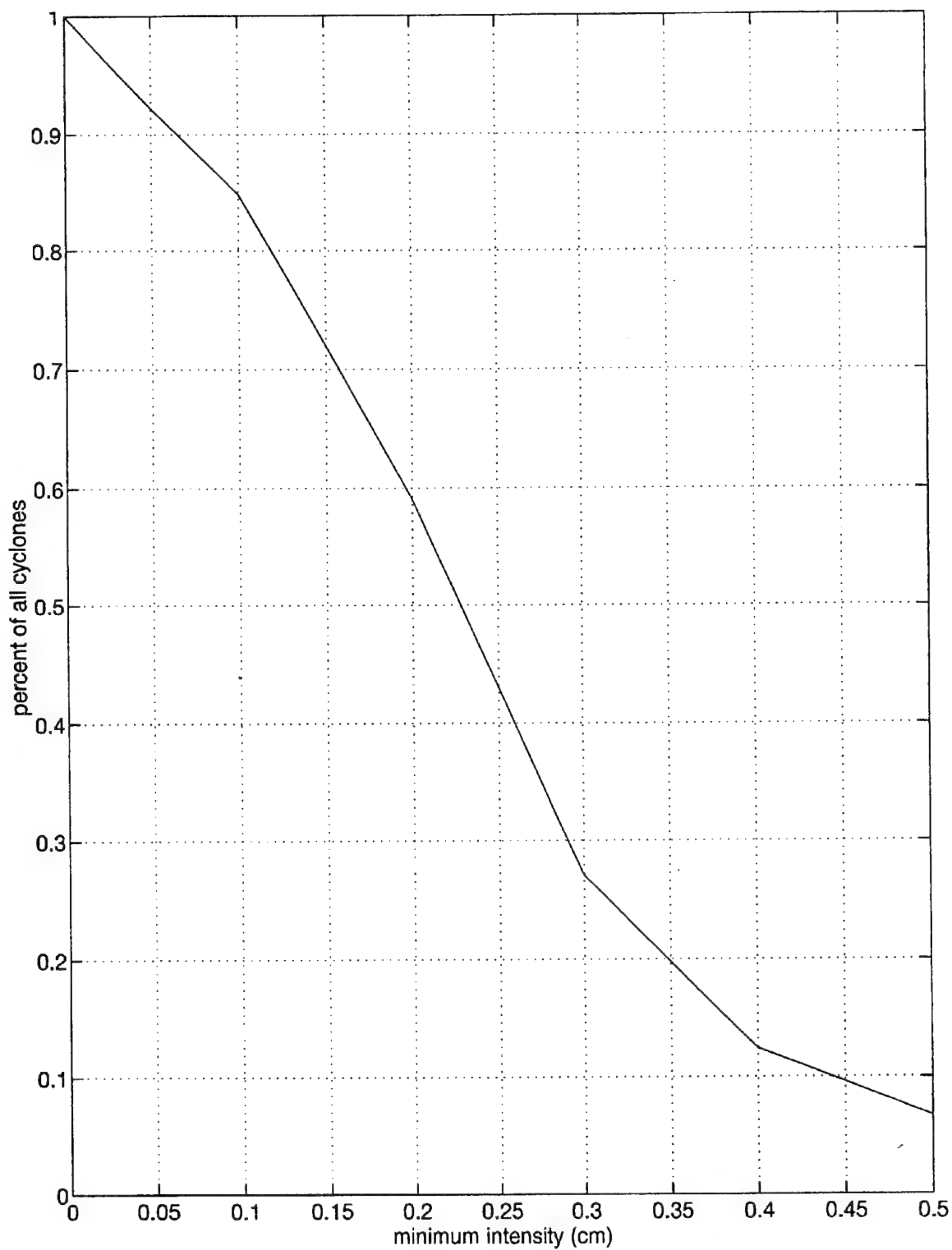
Figure 4.3. Cyclone intensity distribution. The number of cyclones (as a percent of total cyclones) with an intensity at least as large as the minimum intensity, as a function of minimum intensity.
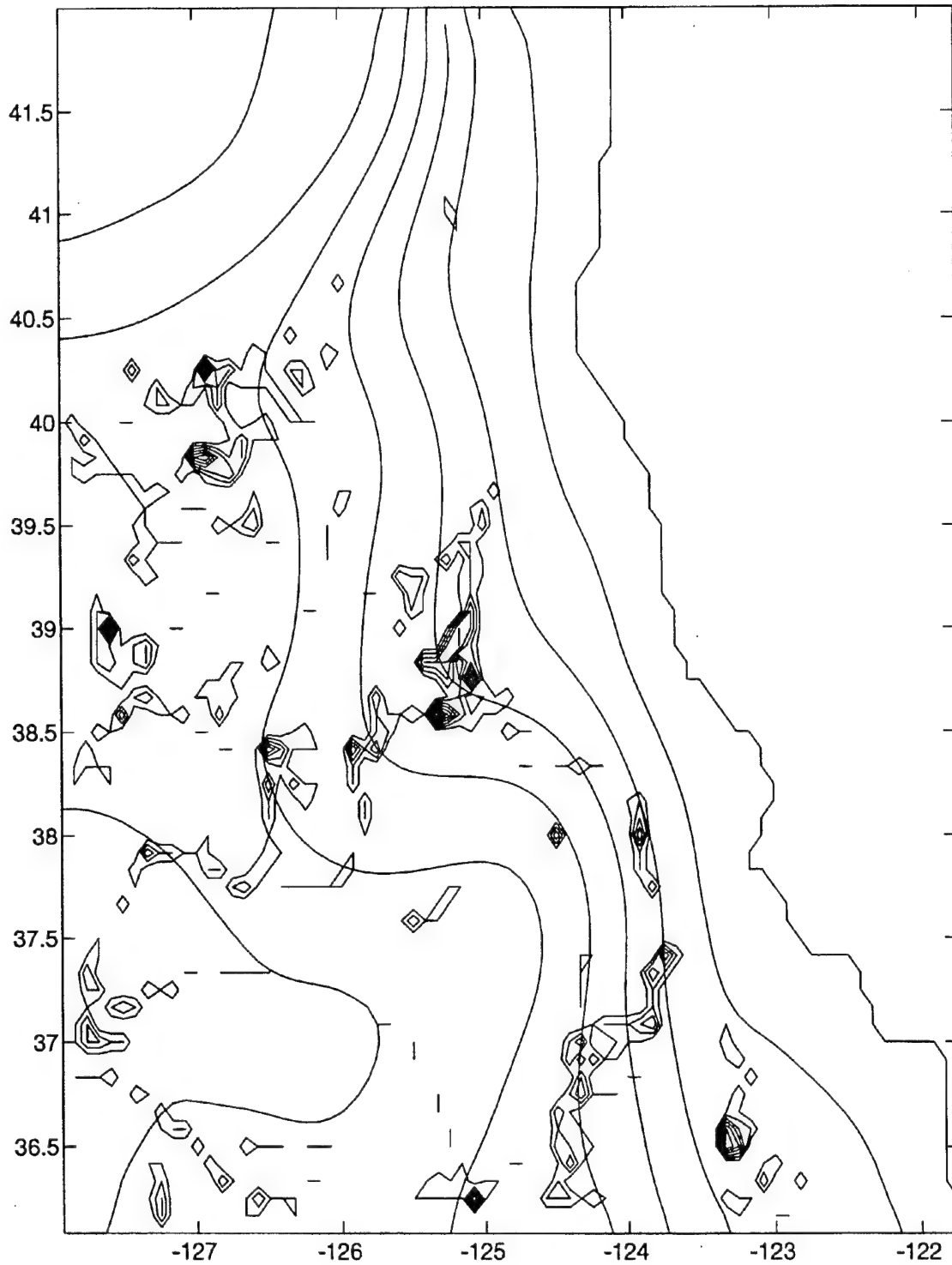
64

Figure 4.4. Same as Figure 4.2 except for the strongest one-third cyclones.
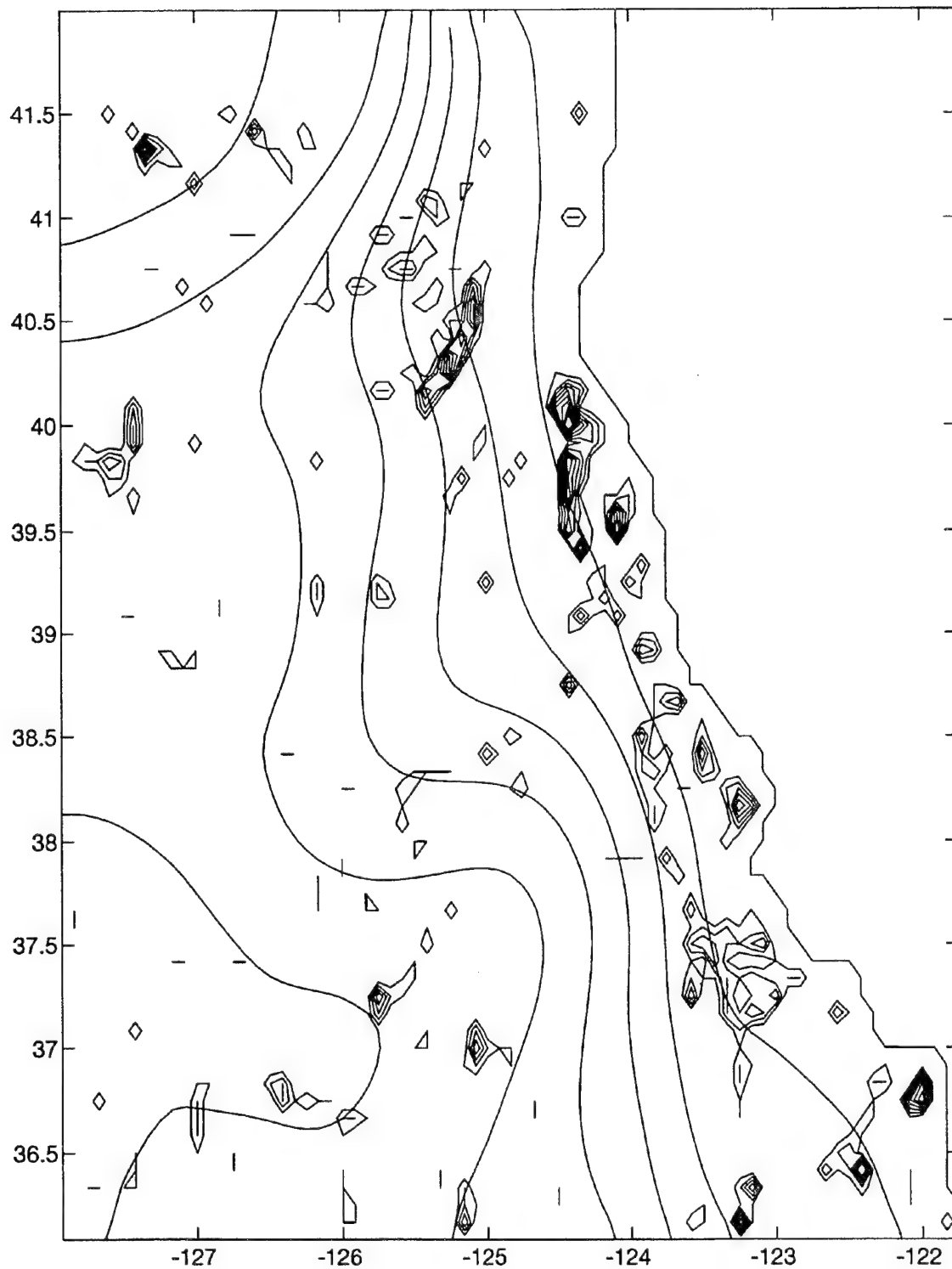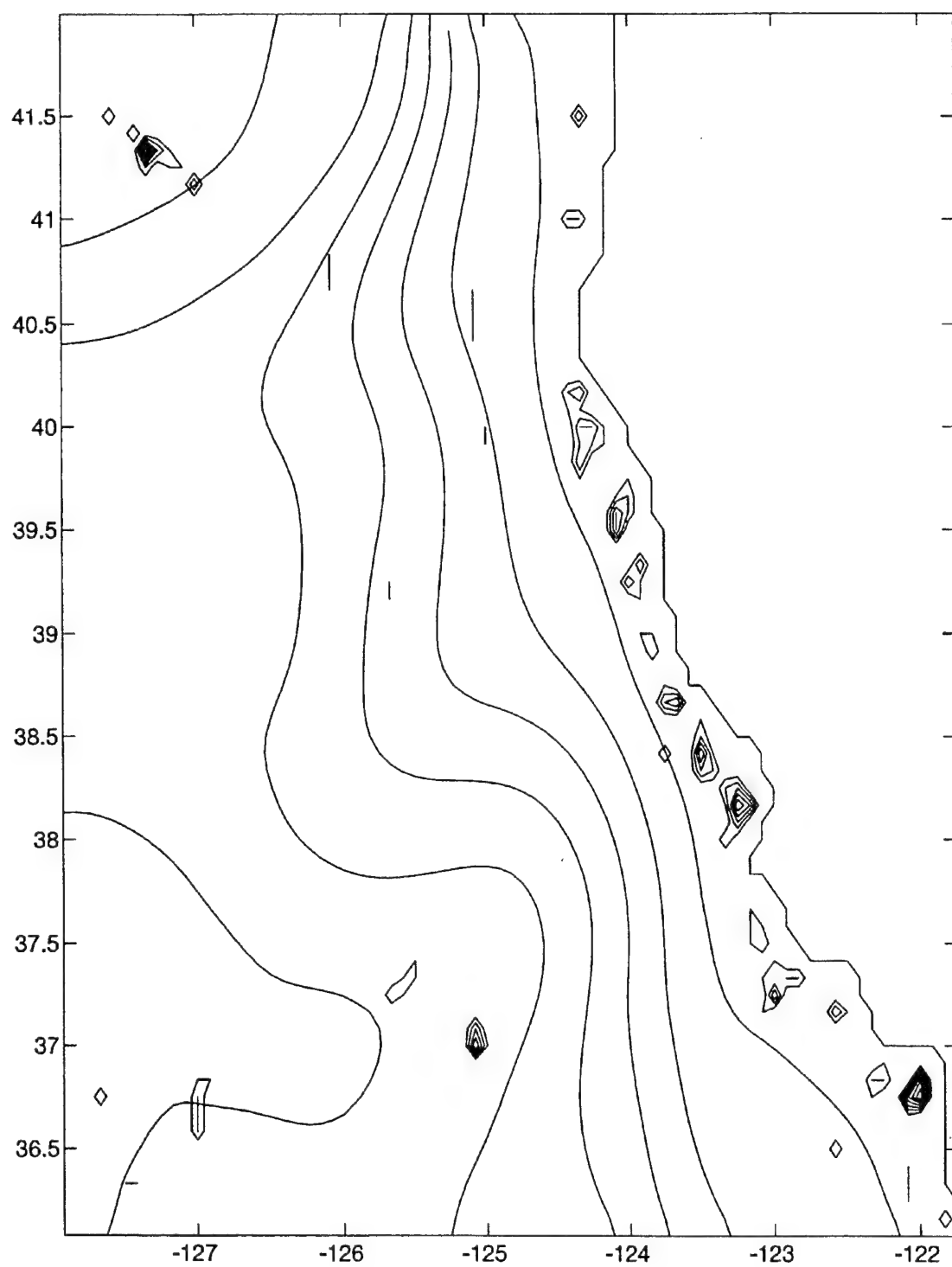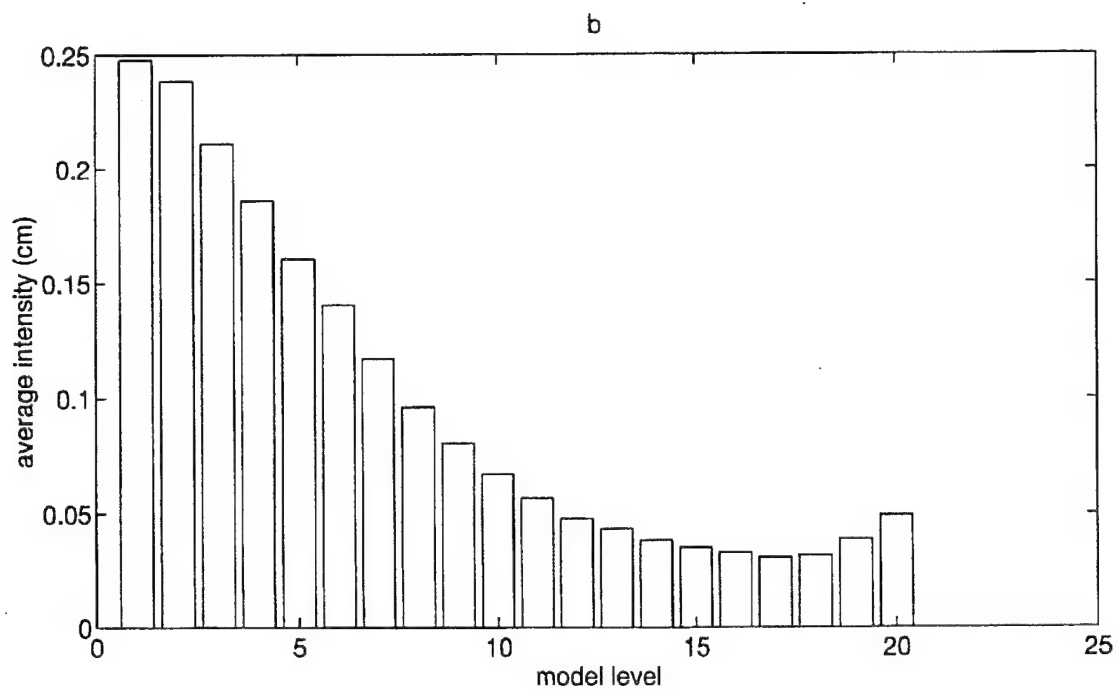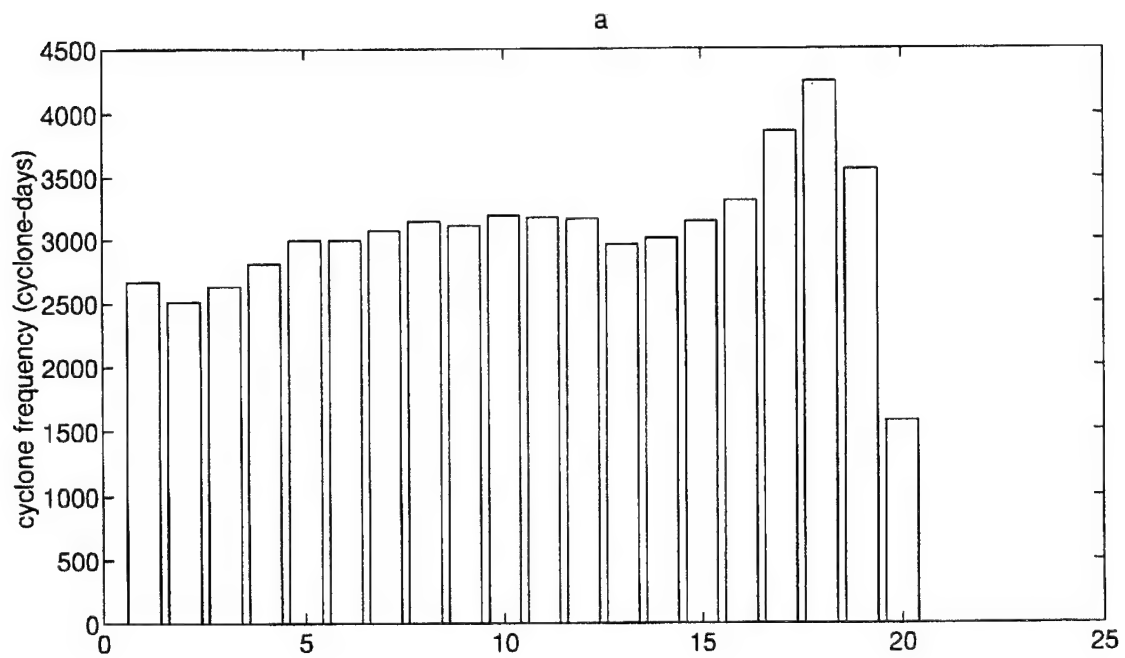
Figure 4.5.   Same as Figure 4.2 except for the weakest one-third cyclones.

66

Figure 4.6.   Same as Figure 4.2 except for the weakest one-tenth cyclones.

Figure 4.7. Cyclone characteristics as a function of depth (model level): (a) cyclone frequency (cyclone-days); (b) average cyclone intensity (cm).
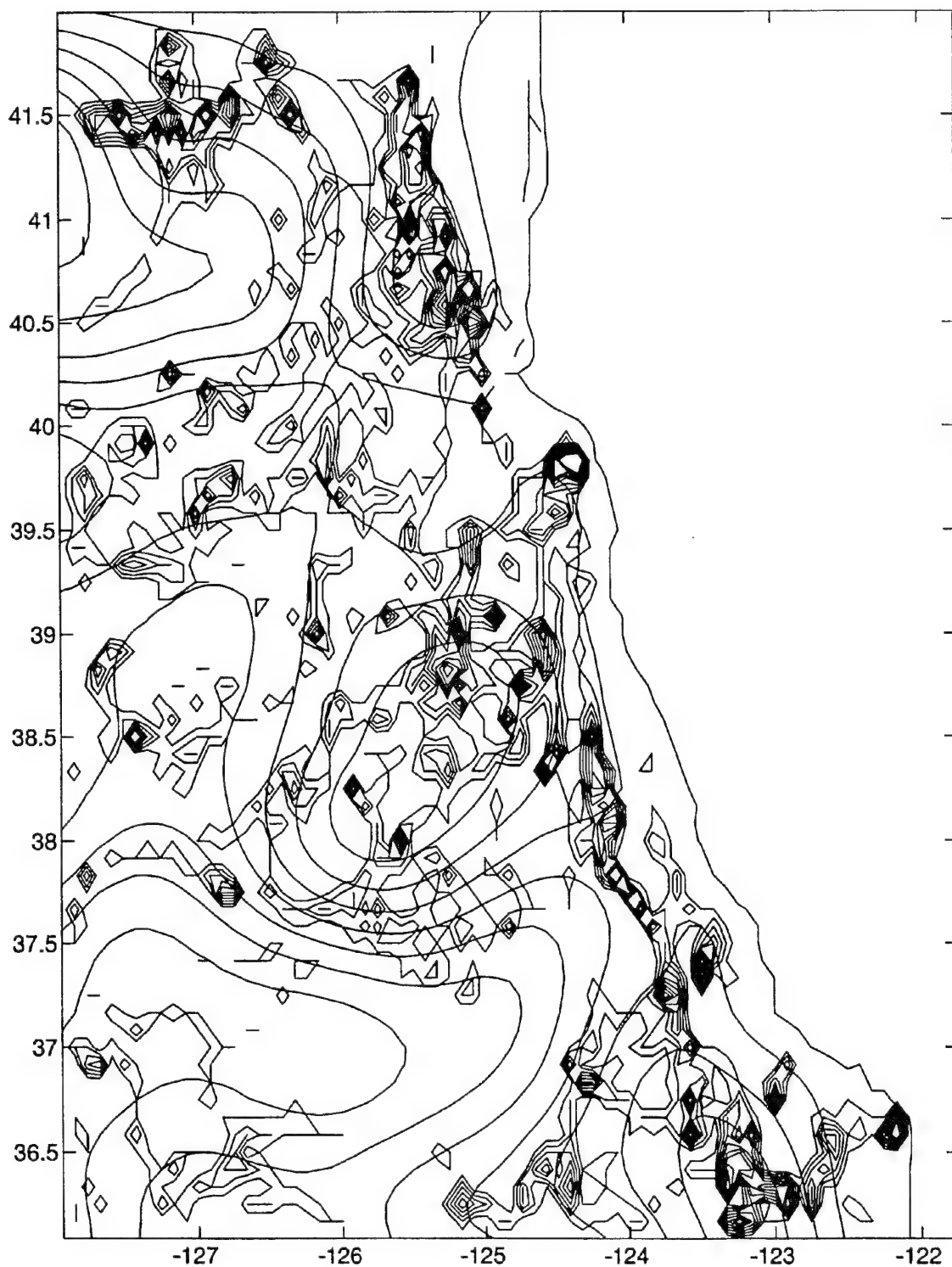
Figure 4.8. Fields of cyclone frequency (cyclone-days) at 756 m depth with a contour interval of 1, and mean pressure (cm) with a contour interval of 0.3.
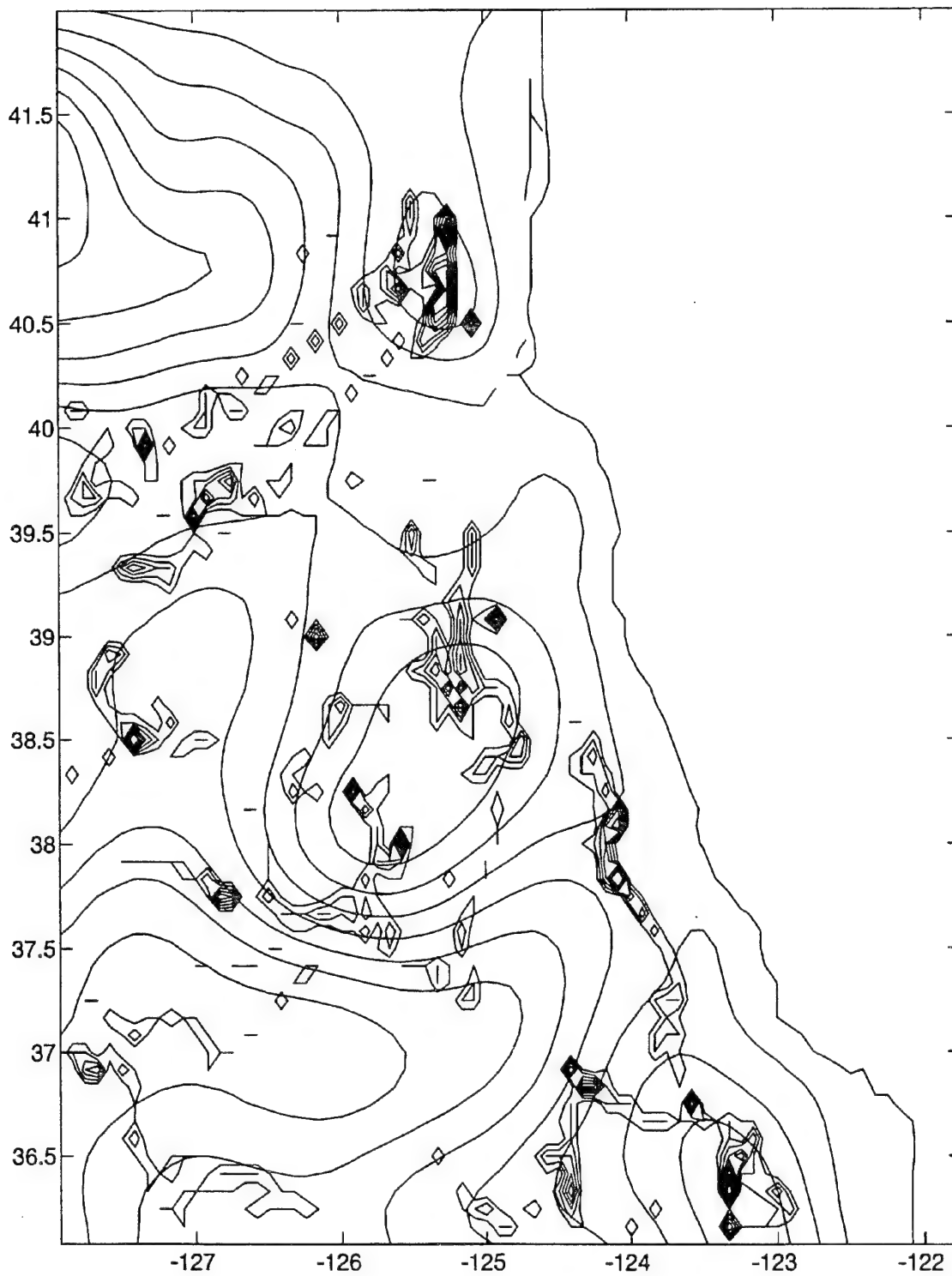
Figure 4.9.   Same as Figure 4.8 except for the strongest one-
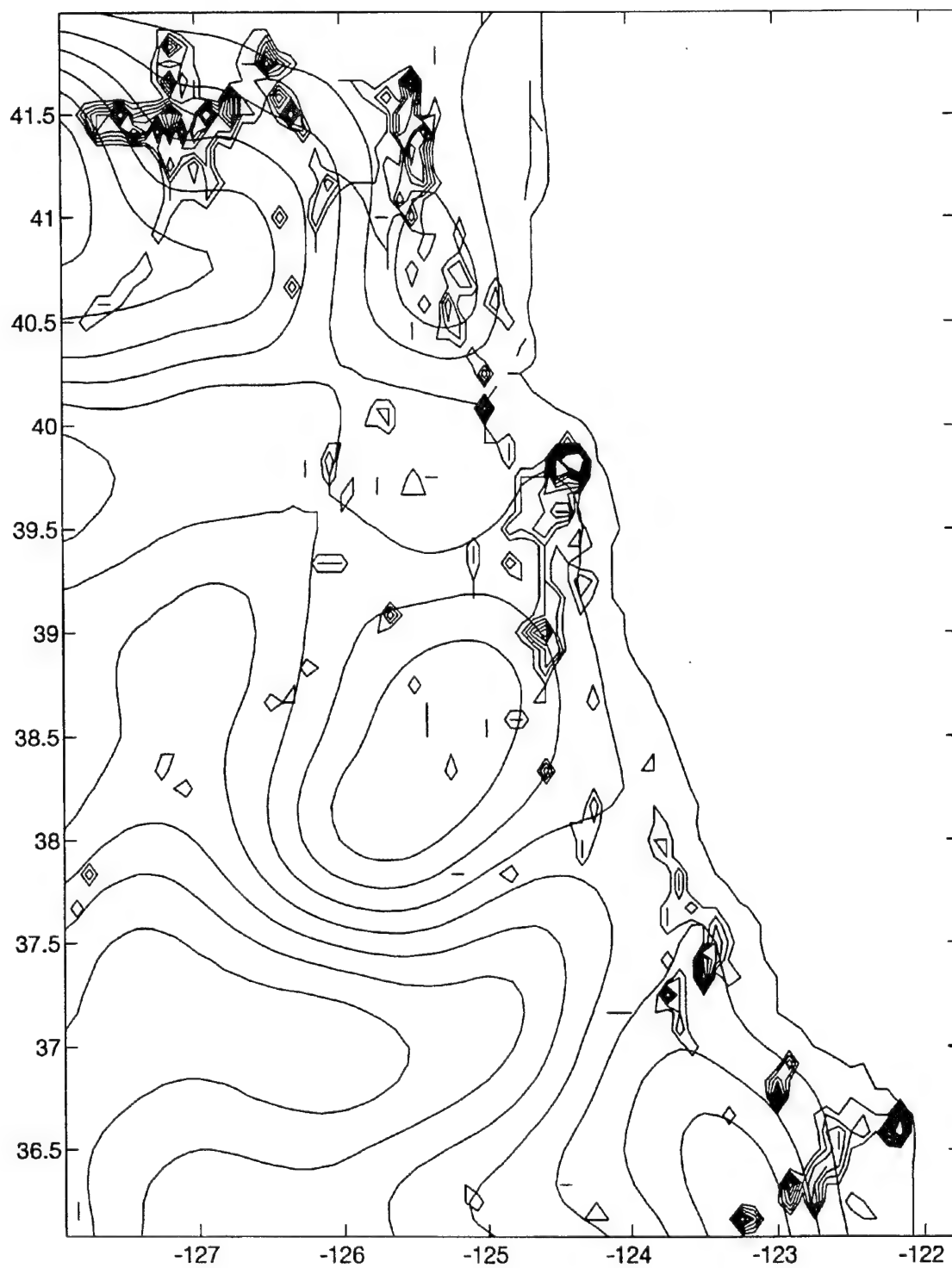third cyclones.

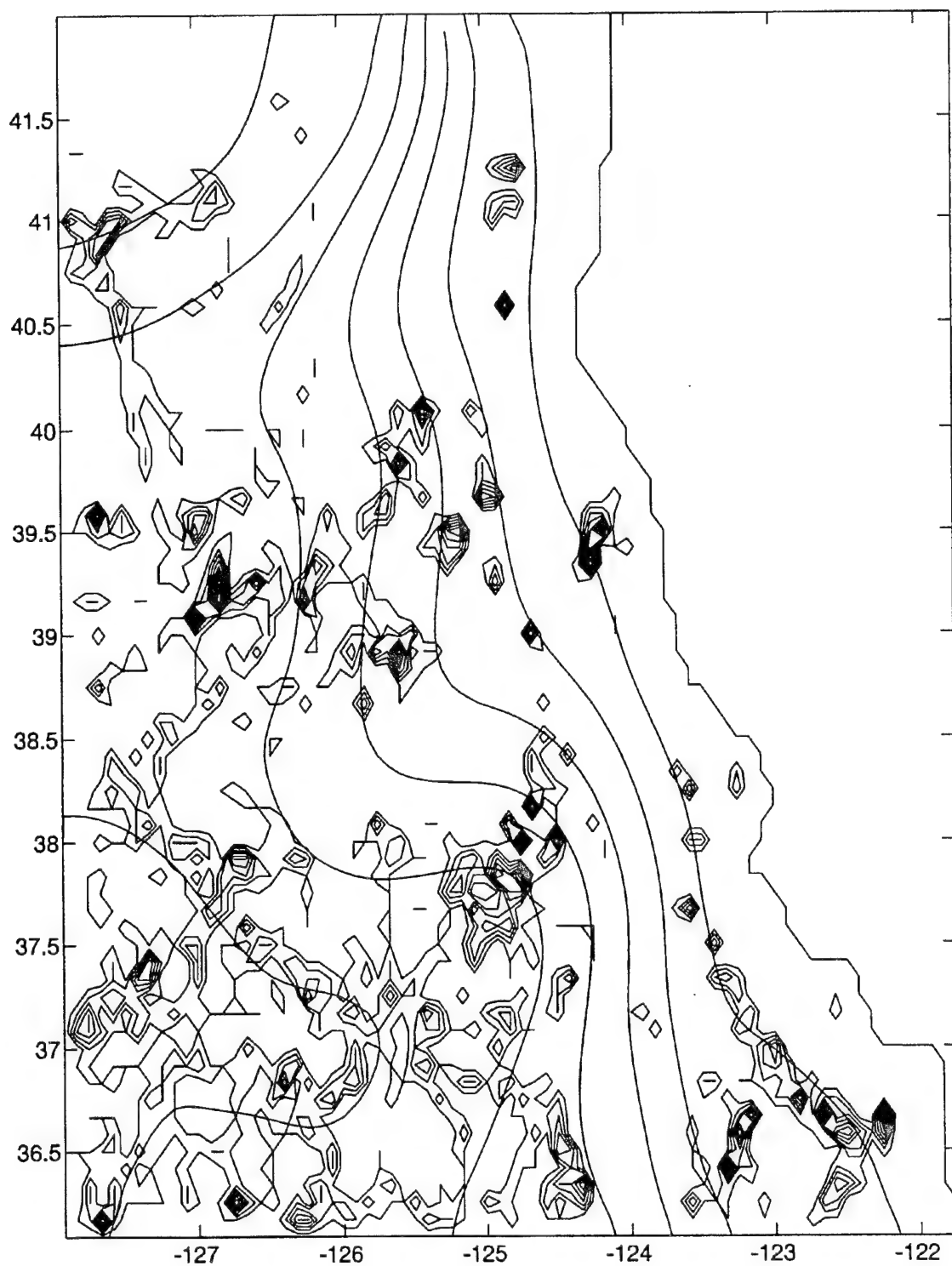Figure 4.10.   Same as Figure 4.8 except for the weakest one-third cyclones.

71

Figure 4.11.   Fields of anticyclone frequency (anticyclone-
days) at 10 m depth with a contour interval of 1, and mean
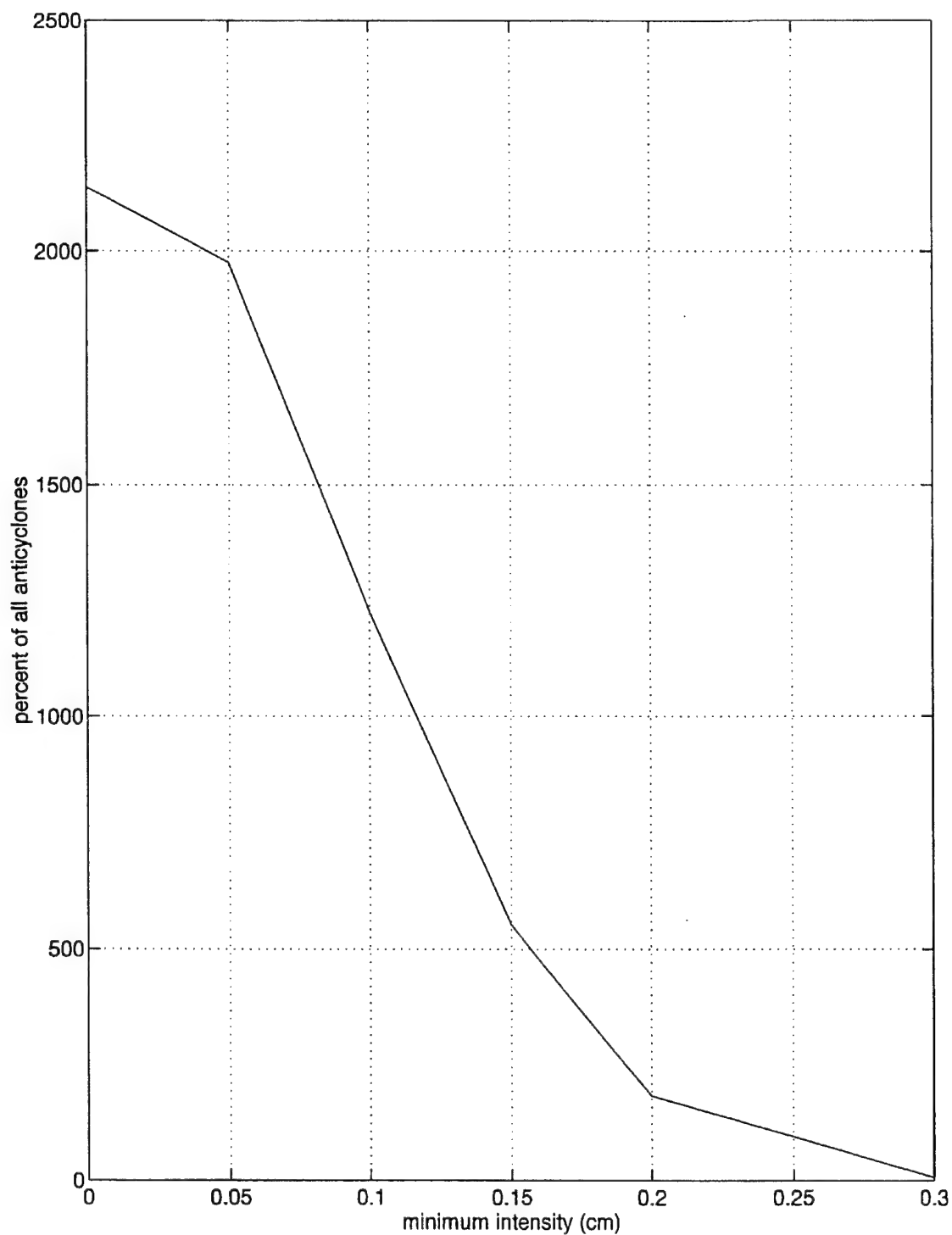pressure (cm) with a contour interval of 5.

Figure 4.12. Anticyclone intensity distribution. The number of anticyclones (as a percent of total anticyclones) with an intensity at least as large as the minimum intensity, as a function of minimum intensity.
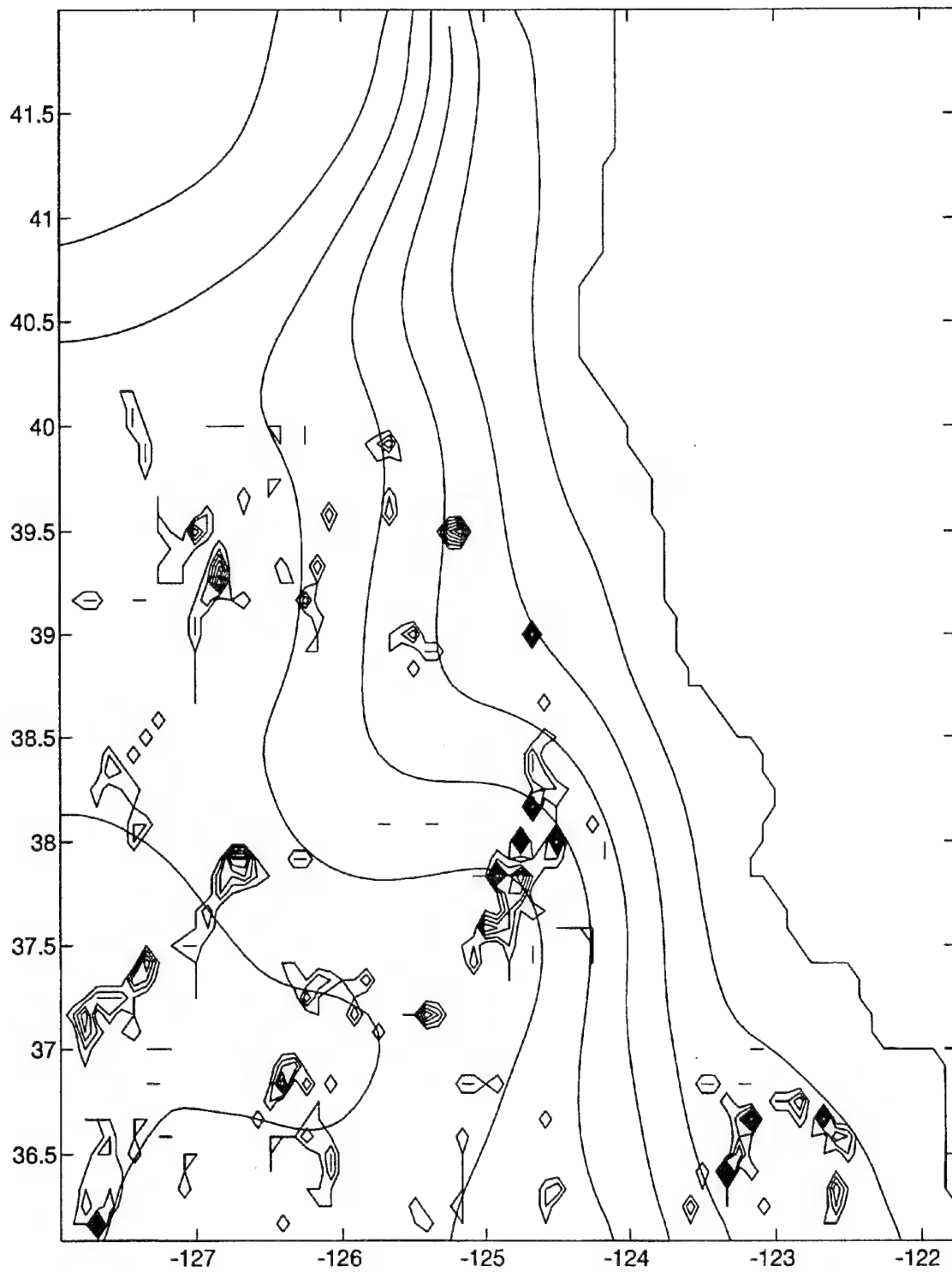
Figure 4.13.   Same as Figure 4.11 except for the strongest
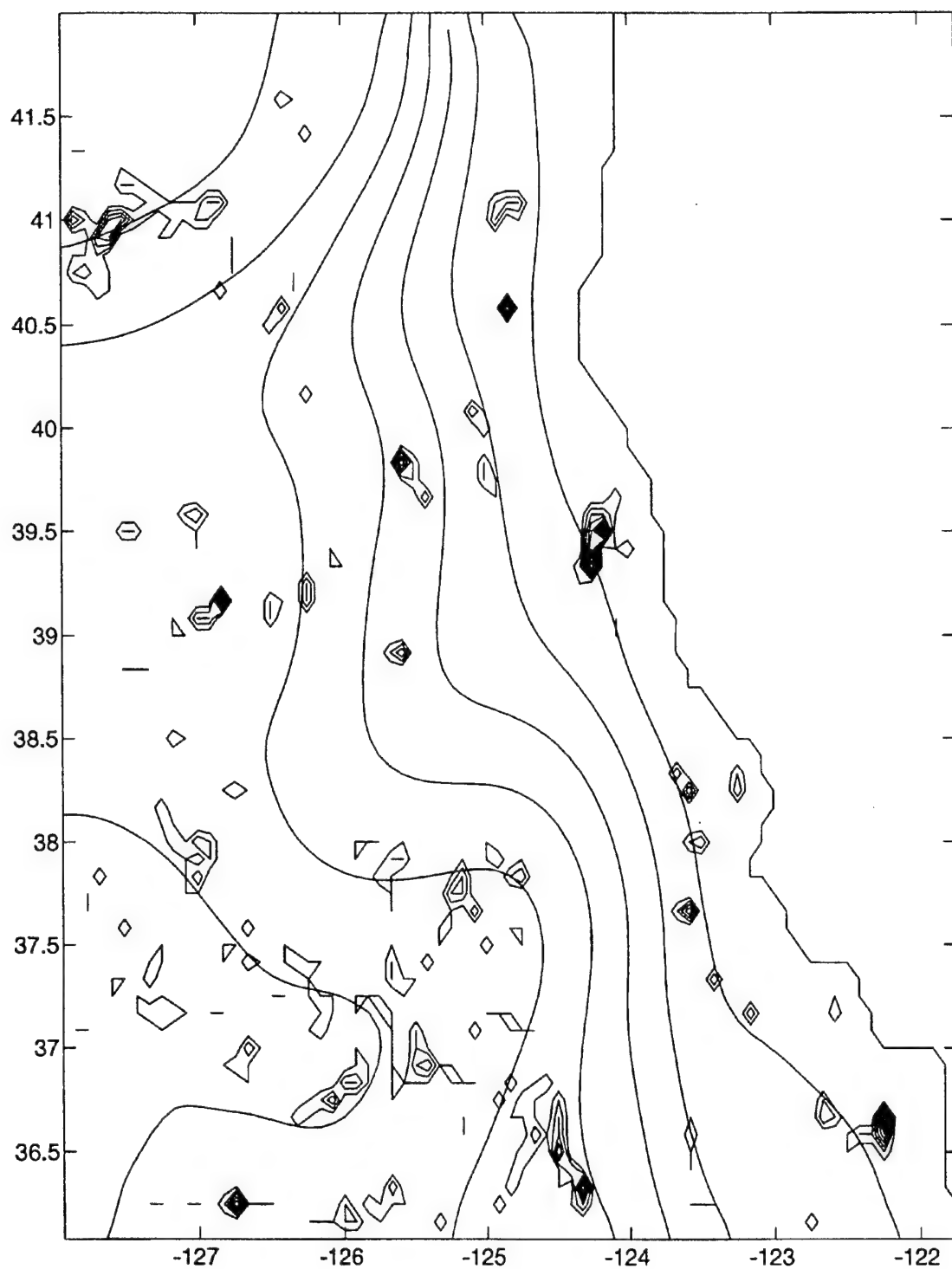one-third anticyclones.

74

Figure 4.14. Same as Figure 4.11 except for the weakest one-third anticyclones.
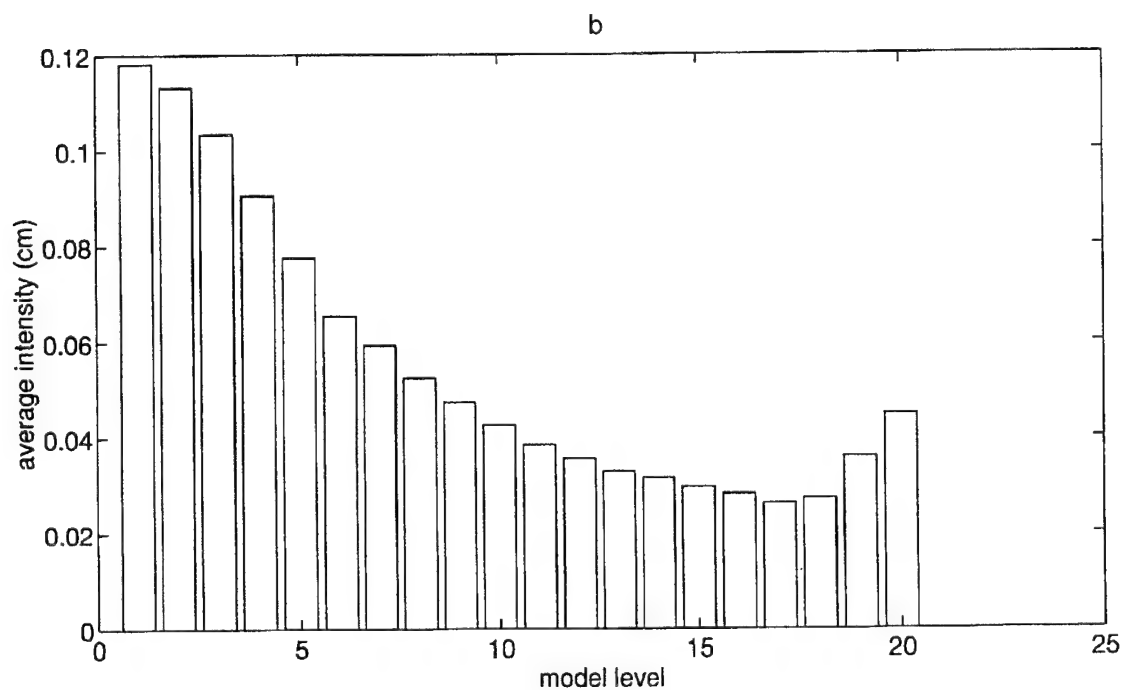
Figure 4.15.   Anticyclone characteristics as a function of depth (model level): (a) anticyclone frequency (anticyclone-days); (b) average anticyclone intensity (cm).

Figure 4.16.   Fields of anticyclone frequency (anticyclone-days) at 756 m depth with a contour interval of 1, and mean pressure (cm) with a contour interval of 0.3.

Figure 4.17. Same as Figure 4.16 except for the strongest one-third anticyclones.

Figure 4.18.   Same as Figure 4.16 except for the weakest one-
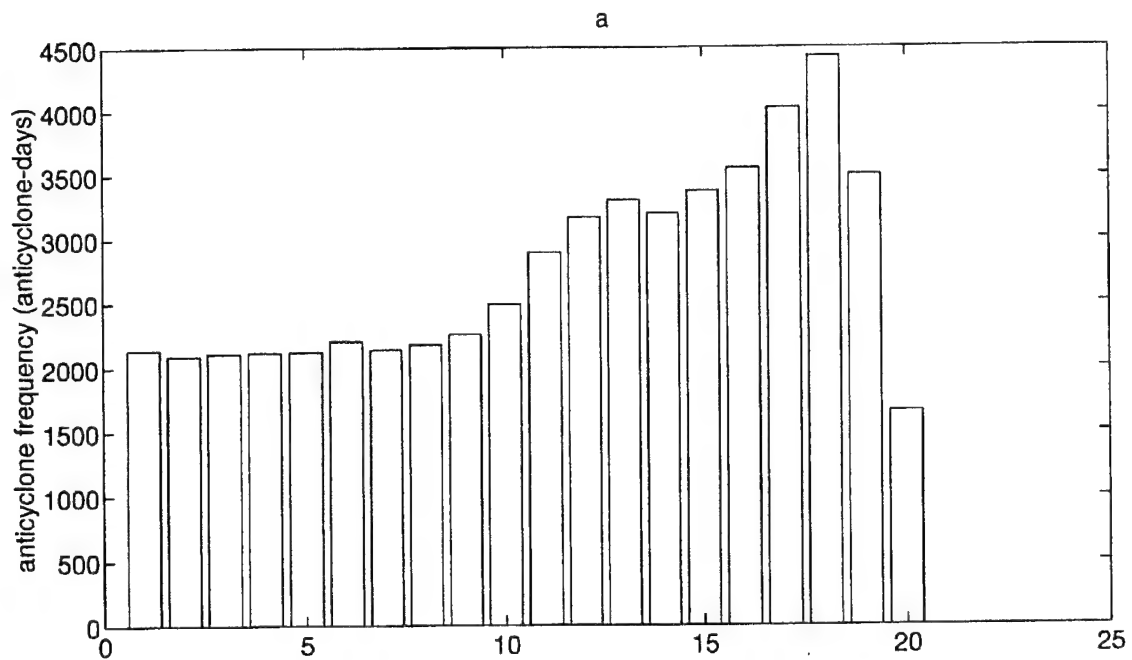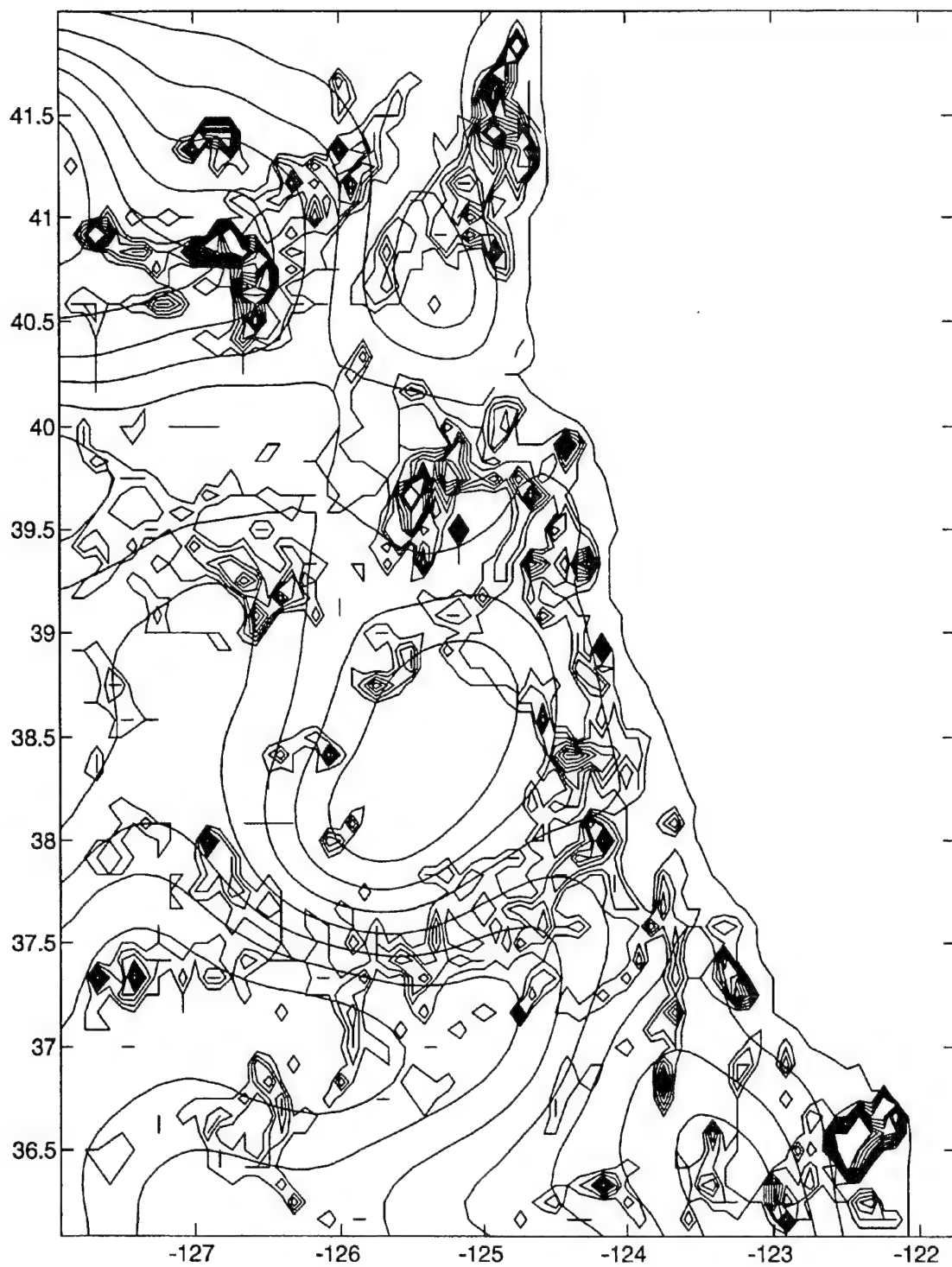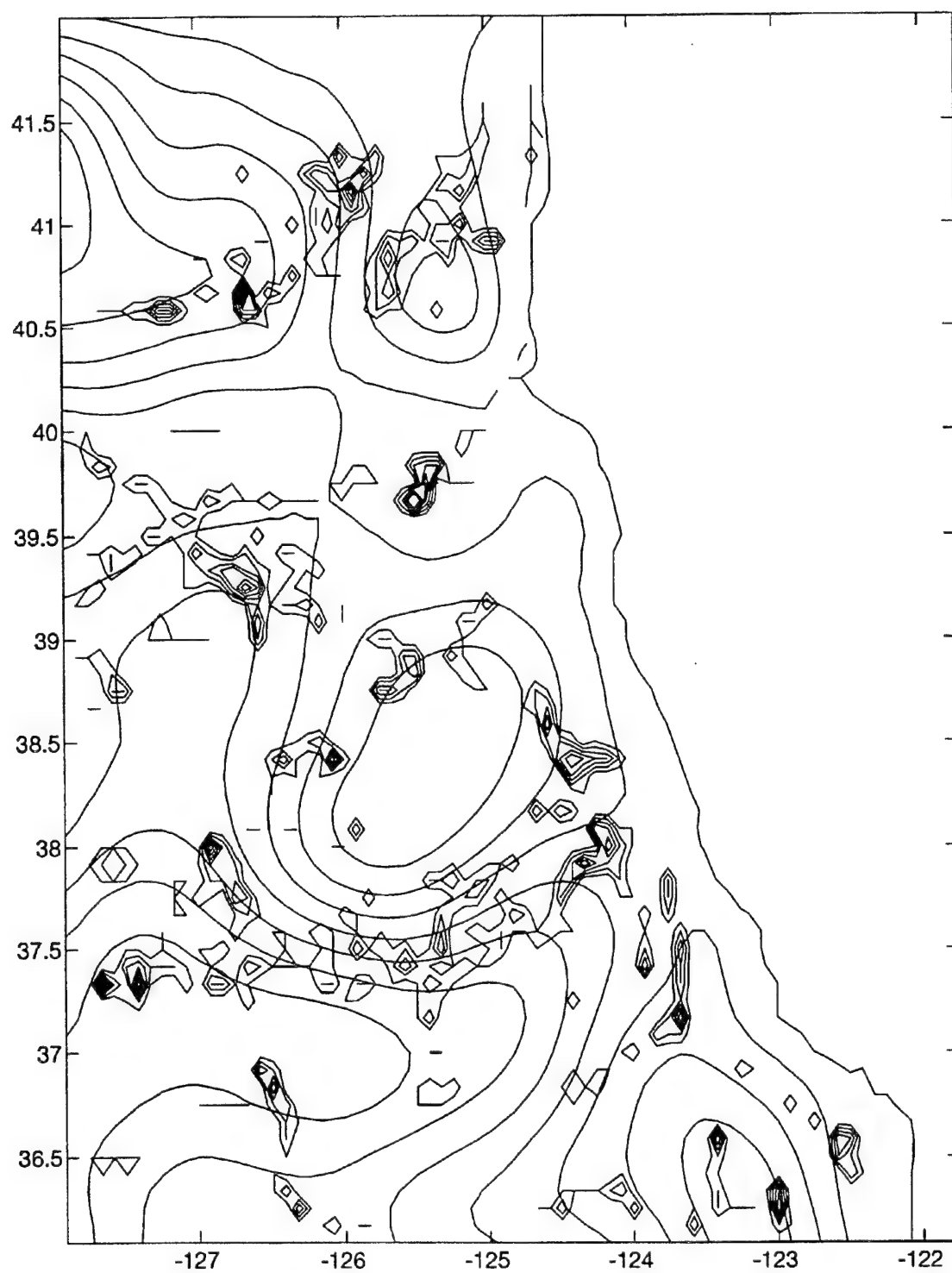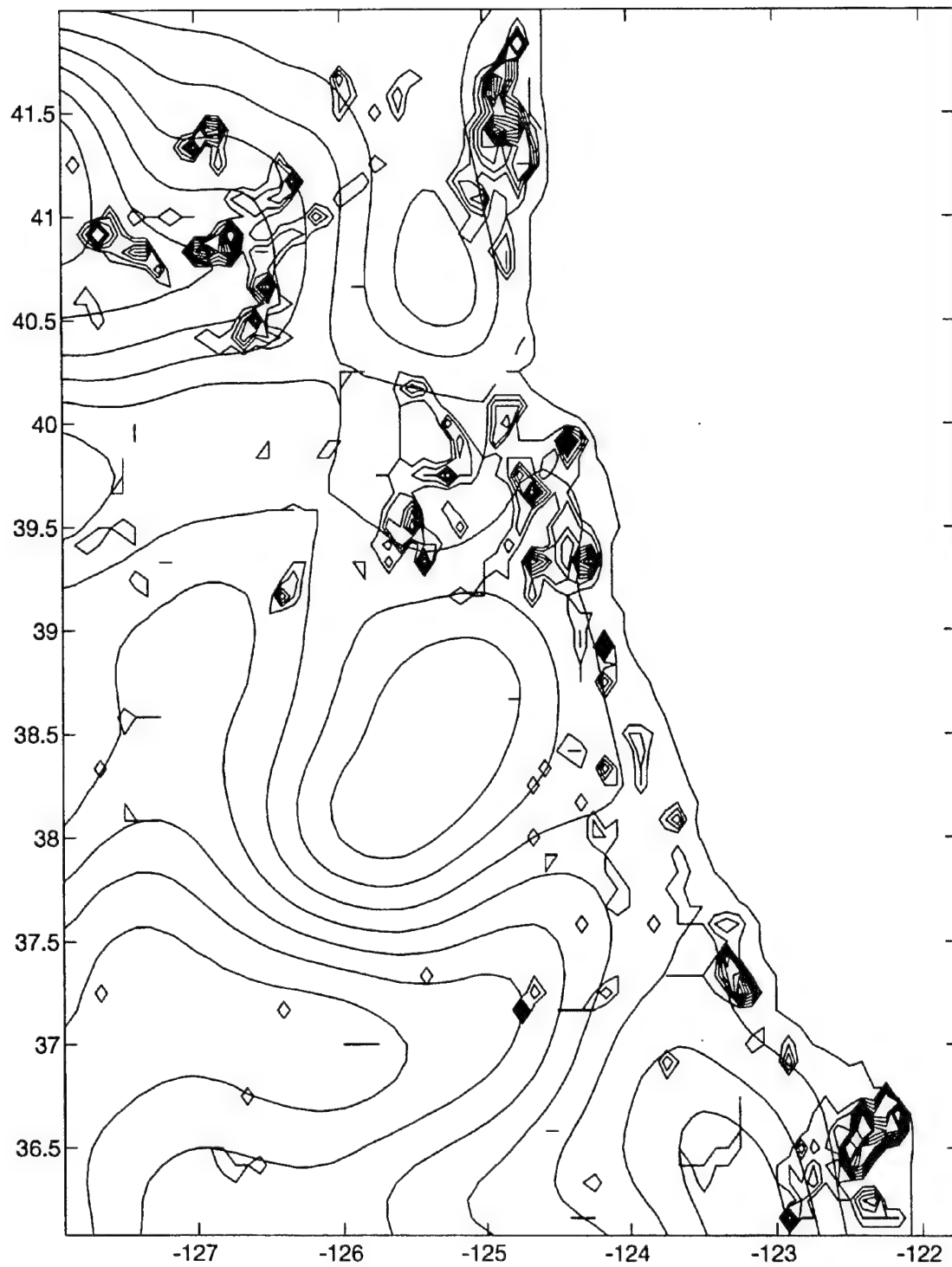third anticyclones.

V. EDDY MOTION

The cyclone and anticyclone frequencies presented in the previous chapter indicated the number of days (out of a possible 540) that a closed cyclonic (low pressure) or anticyclonic (high pressure) eddy was present at each grid point. They do not provide quantitative information on the propagation of those eddies. Eddy phase speed cannot be determined as there is no time dependency involved. A band of high eddy frequency extending offshore could be interpreted in several ways, e.g., as eddies forming inshore and propagating offshore, eddies forming offshore and propagating inshore, a region where eddies form and remain stationary, etc.

In Chapter IV it was shown that the strong surface cyclones are generally located along the mean pressure trough axes which extend out from the capes, while the weak cyclones at 10 m depth are concentrated along the coast. The strong anticyclones are generally located along the mean pressure ridge axes, while the weaker anticyclones at 756 m depth are concentrated along the coast.

In order to further investigate the propagation characteristics of the model eddies, the pressure along the lines indicated in Figures 5.1 and 5.2, were plotted against time at 10 m and 756 m depth. The lines are positioned along and across groups or bands of eddies in the cyclone and anticyclone frequency plots.

A. SURFACE

Line a is located along a broad band of high cyclone frequency extending southwestward from the vicinity of Cape Mendocino, while line b is oriented across the same band and along latitude 38.5°N. Line c is positioned along a band of high anticyclone frequency extending southwest from Point Arena, while line d is oriented across the same band and along latitude 37.5°N. This band of high anticyclone frequency is

81

located between two bands of high cyclone frequency to either side. The time-space plots at 10 m depth for these four lines (Figures 5.3a-5.6a) indicate a non-steady southwestward propagation (right to left on the plots) with an average phase speed of about 10 cm/s. Gradients have a slight tendency to increase towards the offshore side of the plots, indicating intensification of eddies as they propagate offshore.

Line e is positioned along a row of coastal cyclones extending from Cape Mendocino to Point Arena. This row consists six isolated groups of cyclones spaced about 30-40 km apart, and about 20 km offshore. These coastal cyclones were identified as weak cyclones in Chapter IV (see Figures 4.5 and 4.6). The present analysis will help to determine whether or not this is a group eddies propagating down the coast, or a series of eddies separated in space and/or time that might then propagate offshore and change intensity. The time-space plot indicates that the pressure fluctuations at 10 m depth along the coast are very weak (see Figure 5.7). The gradients are weak for the entire three year period. There also does not appear to be any significant propagation in either meridional direction, the pressure fluctuations being primarily in phase all along the coast. These weak pressure fluctuations have an along-coast scale of about 100 km or more. They appear to be caused by minor on-offshore shifts in the position of the equatorward-flowing coastal jet having a relatively long meridional scale and no meridional phase propagation. As discussed in the previous chapter, the coastline is generally a region of lowest surface pressure in the across-shore direction, so a relatively large number of occurrences of closed, but weak, lows are observed there. The associated pressure fluctuations, being less than 2 cm are of no important physical consequence.

B. SUBSURFACE

Time space plots were generated at 756 m depth along each of the same lines identified in the previous section with the exception of line e (see Figures 5.3b-5.6b). These plots indicate a tendency for somewhat steadier and more westward propagation with phase speeds slightly smaller than those seen at 10 m depth.

The phase propagation revealed in all the plots clearly is not that of steady southwestward propagation at constant amplitude that would be seen in a linear model. Regions of amplification and decay (or cross-line propagation) are evident in all the plots. This general tendency for southwestward propagation in the bands of cyclones and anticyclones, is qualitatively similar to the propagation characteristics seen in observations, and attributed to Rossby waves in the simpler model formulation of Pares-Sierra et al. (1993).

The long time scale variation seen in the time evolution of the model fields and discussed in Chapter III, is also evident in these plots. There is significantly more activity and higher gradients during the first and last third of the time history (corresponding to years three and five). The weak coastal pressure fluctuations appear to be of no important physical consequence. The plots also support the observation from the previous chapter of a long time-scale variability with a time scale of about one year.

Figure 5.1. Transects for time-space plots a, b, and e;
overlaid on the fields of cyclone frequency (cyclone-days) at
10 m depth with a contour interval of 1, and mean pressure
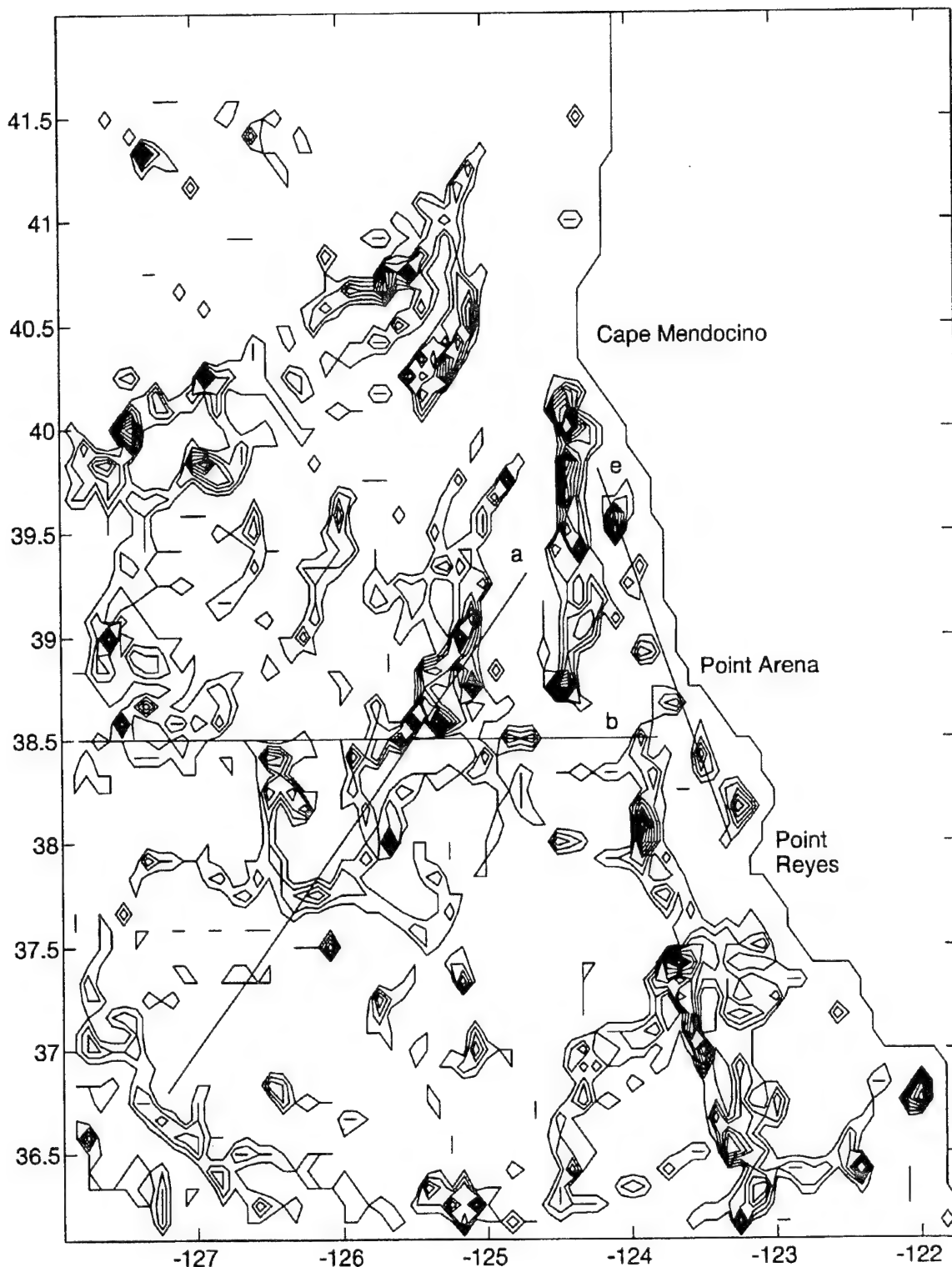(cm) with a contour interval of 5.

84
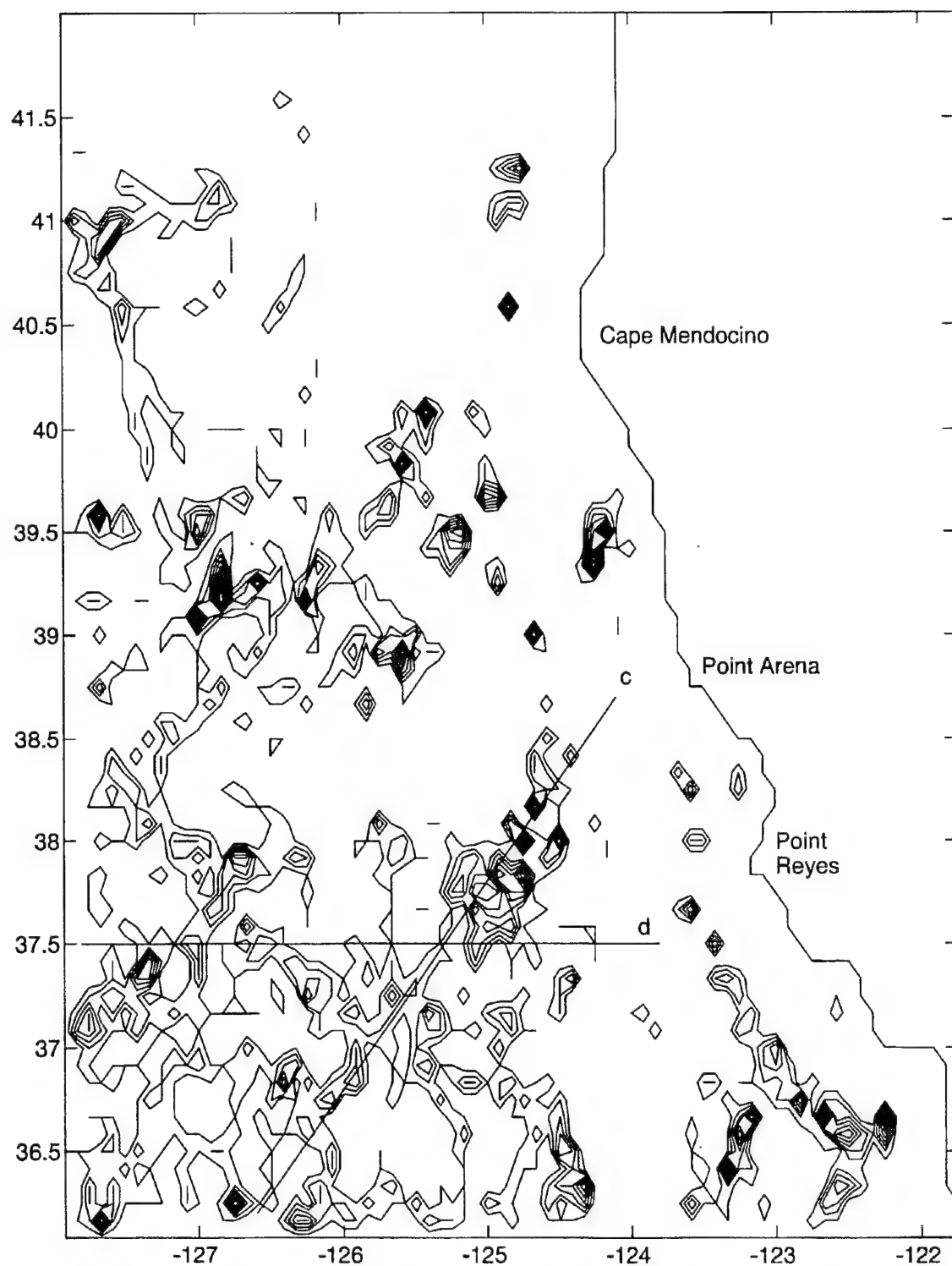
Figure 5.2.   Transects for time-space plots c and d; overlaid
on the fields of anticyclone frequency (anticyclone-days) at
10 m depth with a contour interval of 1, and mean pressure
(cm) with a contour interval of 5.

85

Figure 5.3. Time-space plots along transect a: (a) 10 m depth; (b) 756 m depth.

Figure 5.4.   Time-space plots along transect b: (a) 10 m depth; (b) 756 m depth.

Figure 5.5. Time-space plots along transect c: (a) 10 m depth; (b) 756 m depth.

Figure 5.6. Time-space plots along transect d: (a) 10 m depth; (b) 756 m depth.

89

Figure 5.7.   Time-space plots along transect e at 10 m depth.

VI. SUMMARY AND CONCLUSIONS
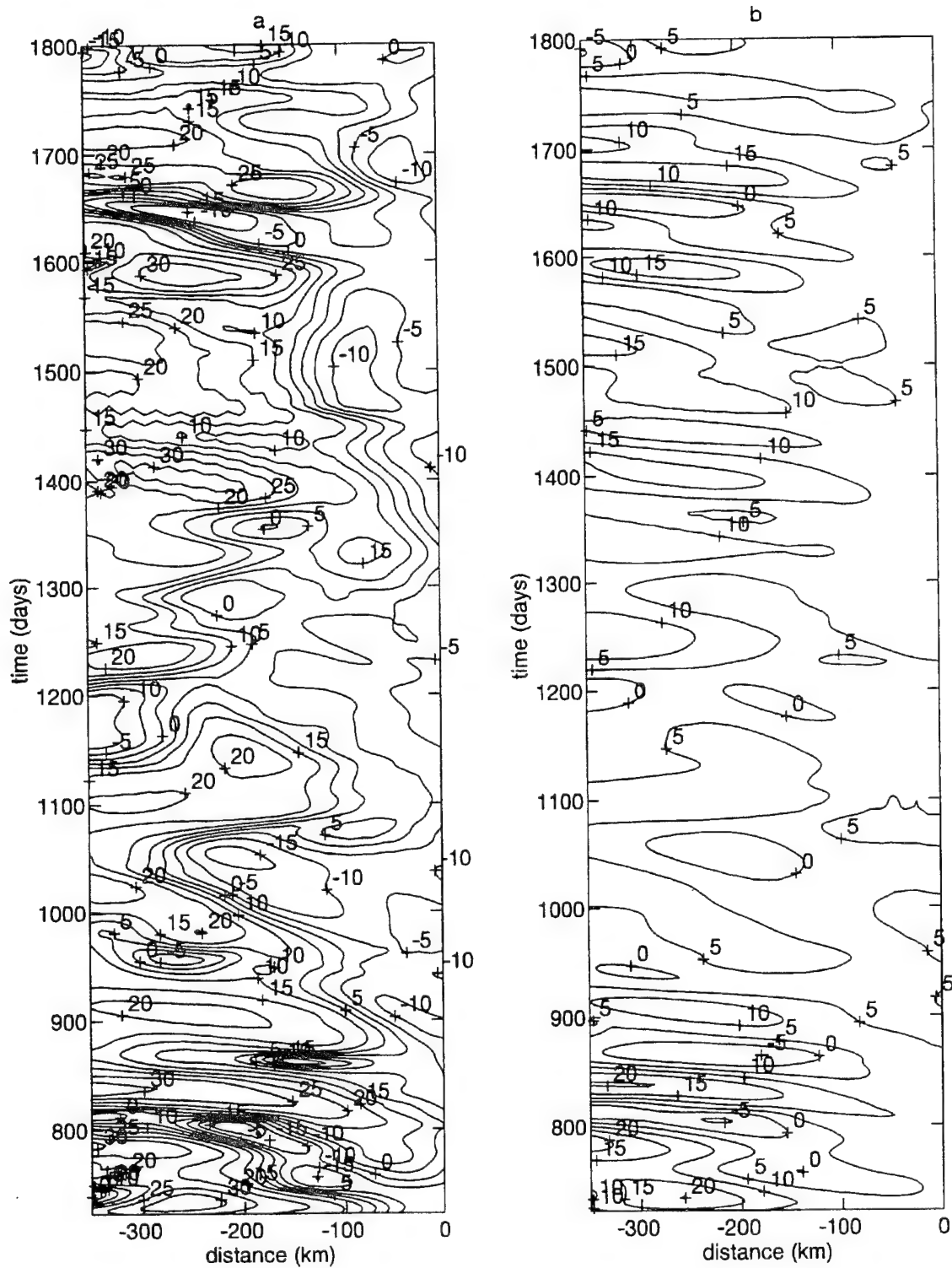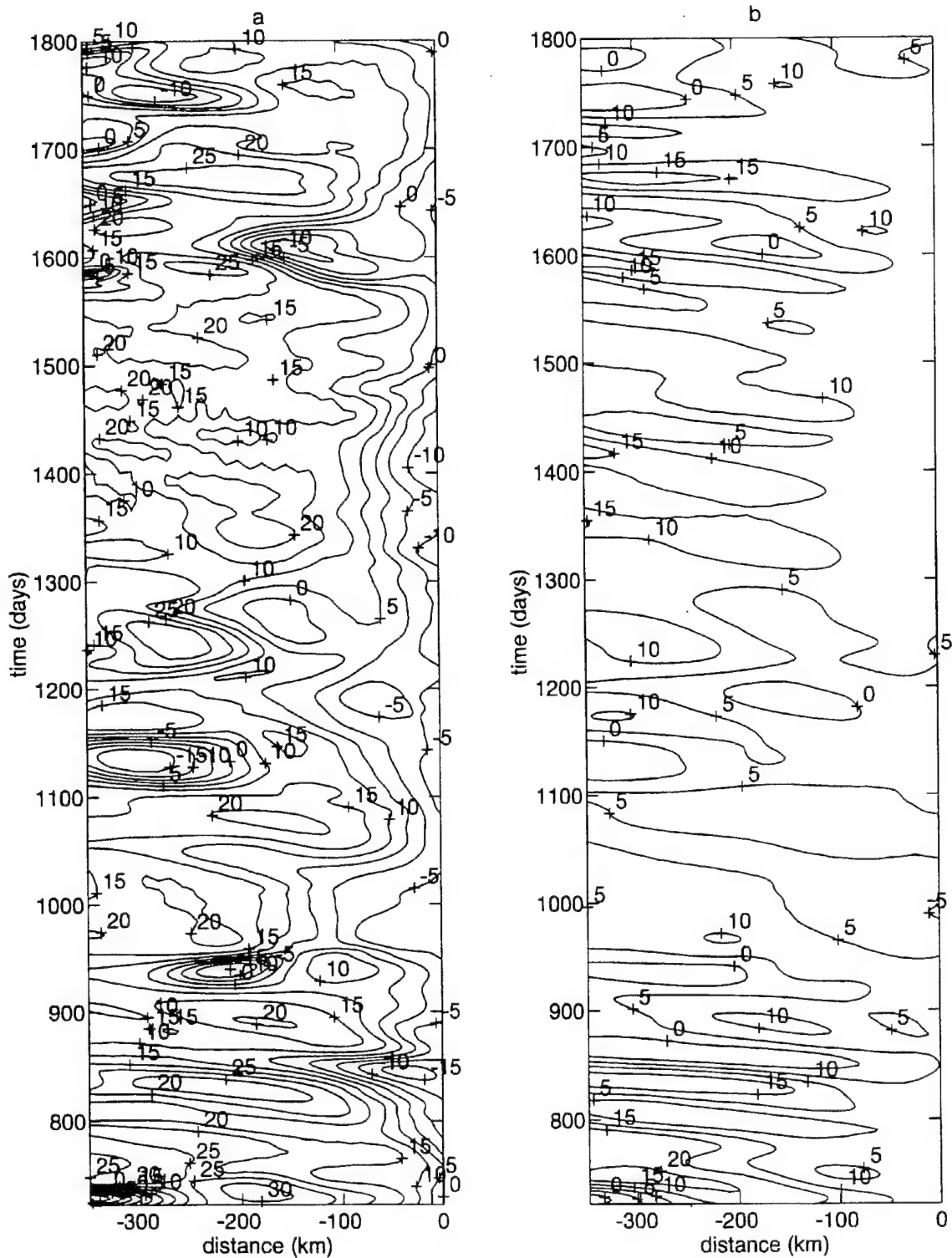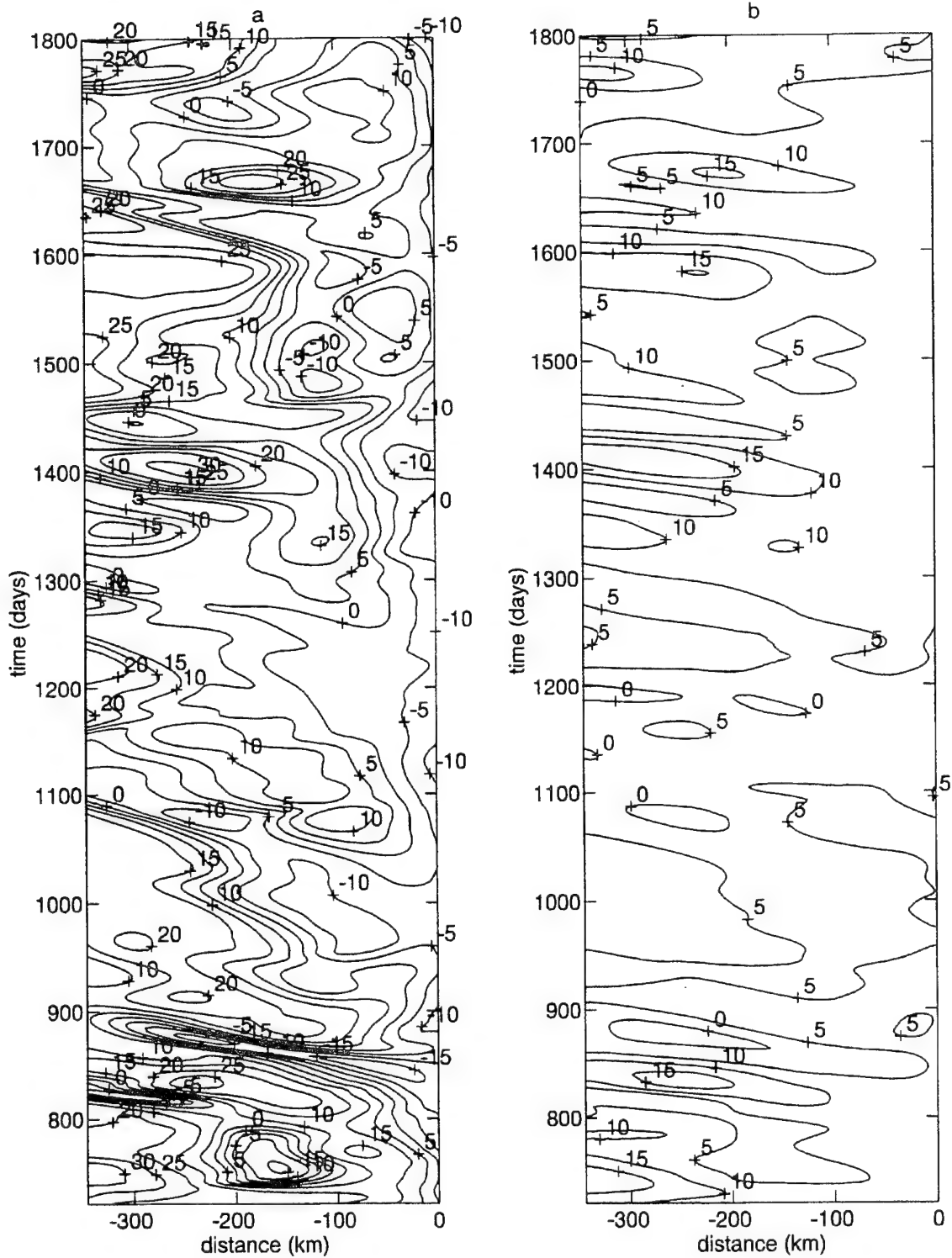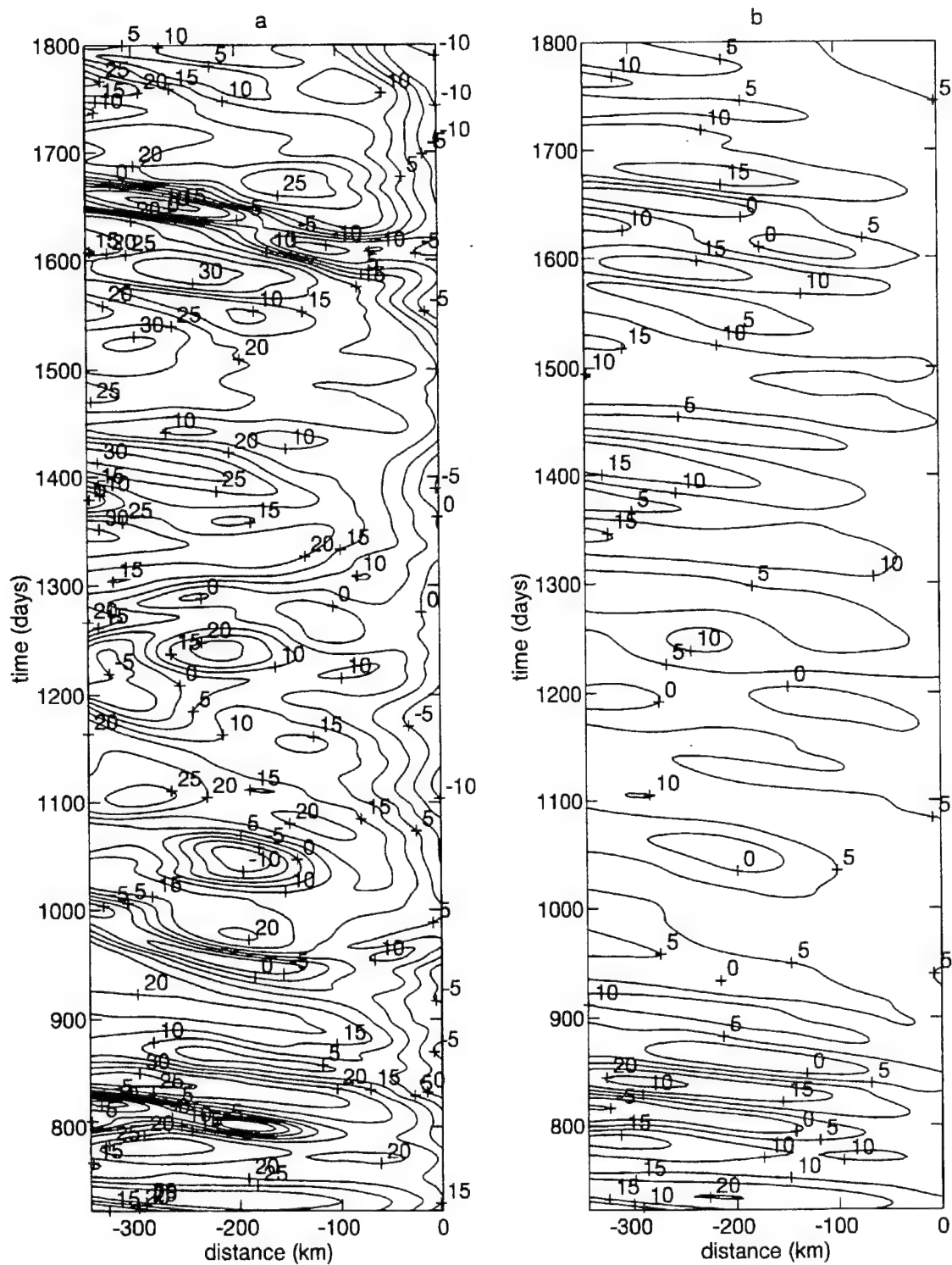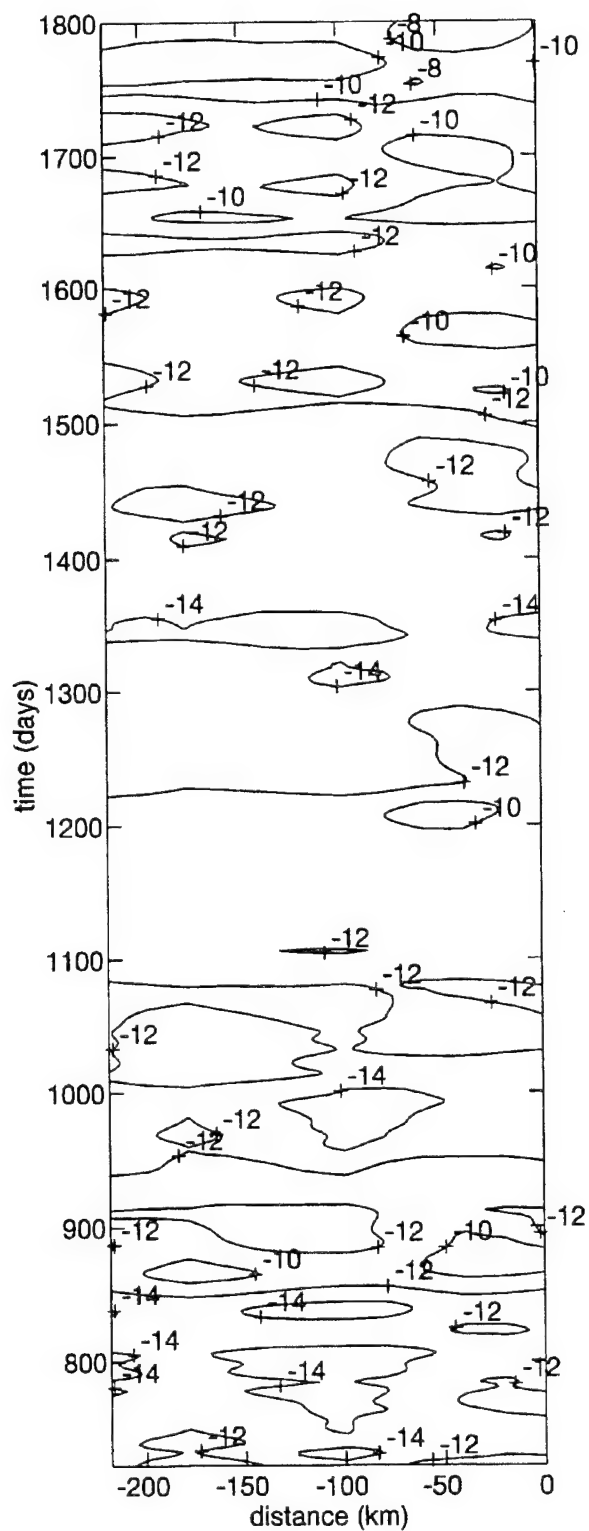
The DIECAST ocean model was used to simulate mesoscale variability in the California coastal zone. This simulation was the first to use realistic coastal geometry and topography in a high resolution model run to equilibrium in the California coastal zone. The objective of the study was to test the importance of boundary forcing in the form of an equatorward-flowing coastal surface jet imposed at the northern boundary, in driving eastern ocean boundary variability. Surface forcing was kept simple with damping to Levitus (1982) climatological (summertime) values of temperature and salinity. There was no wind forcing in the model. The model was run for five years with two years allowed for the model to reach equilibrium, and the remaining three years used for data analysis.

A. SUMMARY OF RESULTS

Time evolution of the model fields show eddies forming at all three capes with a shedding period of about 85 days. In addition, there is a longer term variability with a time scale of about one year suggested by the three year run.

The horizontal fields offshore of Point Arena showed that at 157 m depth temperature gradients are too high, temperatures are too cold, and the salinities are too high, compared to observations.

The mesoscale features produced by the model are qualitatively consistent with those seen in observations. Their spatial scales were somewhat larger and their intensities somewhat less than observations. The equatorward-flowing coastal jet imposed at the northern boundary, although structured after observations, increases in horizontal and vertical scale as it meanders south through the domain. Its maximum vorticity is about half that seen in observations, and

91

the vertical velocity associated with meanders in the jet is also less than that inferred from observations. The model produces a poleward-flowing undercurrent adjacent to the continental slope as in observations, but it is significantly weaker, broader, and deeper than observations.

The frequency of closed cyclones and anticyclones showed that there are patterns or preferred locations for cyclones and anticyclones. The results showed strong signals when compared with the coastal geometry, topography, and the three year mean pressure fields. The stronger cyclones are located along the mean pressure trough axes, while the stronger anticyclones were located along the mean pressure ridge axes. There are many weak cyclones and anticyclones located along the coast, but these appear to be of little physical significance. Cyclone and anticyclone frequencies increase with depth, while their intensities decrease with depth down to 2000 m and then increase to the bottom. This indicates a separate group of topographically-forced cyclones and anticyclones distinct from those present at the surface and dominant below 2000 m.

Time-space plots were taken along transects positioned along and across bands of high eddy frequency at 10 m and 756 m depth. The 10 m depth plots showed areas of intensification and decay (or cross-line propagation) and non-steady offshore propagation with an average phase speed of about 10 cm/s. The 756 m plots show a more steady offshore propagation with a slightly slower phase speed than those at 10 m depth.

B.   CONCLUSIONS

Results indicate the use of boundary forcing only, in a high resolution model, with realistic topography and coastal geometry, and run to equilibrium, produces ocean variability generally consistent with observations in the California coastal zone.

The result that the model creates mesoscale features of larger scale and less intensity than observations may be caused by a combination of the lack of wind forcing in the model and to lesser degree, the structure of the jet imposed at the northern boundary. While the jet was structured to replicate those seen in observations at the northern boundary, it broadens both vertically and horizontally as it meanders through the domain. The addition of wind forcing by climatological winds is the subject of a study currently in progress. It was not included in this study in order to isolate the effect of boundary forcing. Pares-Sierra et al. (1993) tested the importance of two hypothesized sources for the generation of eddies in the California Current: (1) local baroclinic instability of the main current, and (2) remote generation of eddy activity by wind forcing adjacent to the coast. They concluded that the dominant source is wind forcing adjacent to the coast, modified by Rossby dynamics. In this model, the addition of wind forcing would bring additional energy into the system, probably increasing the intensity of the features and making them more in line with observations. The effect of wind forcing on the spatial scales remains to be seen.

The cold temperatures and high salinities produced by the model below the surface are probably caused by the use of steady model forcing based on summertime (maximum upwelling) observations of the coastal jet, as well as steady surface damping to summertime Levitus climatology. The constant addition of cold salty water at the northern boundary would necessarily result in a gradual overall decrease in temperature and increase in salinity in the domain over the five year model run. Visual inspection of the time series of density taken 100 km offshore Point Arena suggest that this is the case (see Figure 3.1). Additionally, the adjustments made to the Levitus (1982) values at the northern boundary were

93

quite large. Along the coast, at 150 m depth the temperature was reduced from about 8.0°c to about 5.5°c. This 2.5 degree adjustment represents by itself, about three-fourths of the discrepancy with observations.

The broader, deeper, and weaker (than observations) undercurrent indicates that the onshore geostrophic current driven by the poleward pressure gradient between the northern and southern boundary conditions, is not strong enough to force sufficient downwelling of isopycnals along the coast at depth, to drive an undercurrent as strong as in observations. However, when combined with wind forcing, the inclusion of the alongshore pressure gradient has been shown to improve the prediction of alongshore velocities (Federiuk and Allen, 1995). The addition of boundary forcing at the southern boundary, in the form of a poleward-flowing undercurrent structured after observations, might correct some of this discrepancy. This southern boundary forcing arguably should have been included in this study, as this is a study of the importance of boundary forcing, but the separate role of the poleward pressure gradient produced by the northern and southern boundary conditions, in driving the undercurrent, was an additional objective of this study.

As this was the first simulation in the California coastal zone to use realistic topography and coastal geometry, the effects of these two factors on eddy formation and propagation is an important result. The cyclone and anticyclone frequency plots provided information on the preferred locations of cyclones and anticyclones, but could not provide a quantitative measure of eddy propagation, or a statistical analysis of eddy formation regions and tracks. A more sophisticated tracking method would be required to provide that information. The frequency plots do show that cyclones and anticyclones do have distinct preferred locations. These locations must be the result of topography

94

and/or coastal geometry as there are no other factors. Time space plots used in conjunction with the frequency plots provided additional information on the propagation of the model eddies.

The conclusion of this study is that a model simulation utilizing realistic topography and coastal geometry with boundary forcing only, can produce results that are consistent with observations to first order. The inclusion of wind forcing (currently in progress), southern boundary forcing in the form of a poleward-flowing undercurrent, and most importantly, an annual cycle for all model forcing, will likely bring the results more in line with observations. An adjustment to the structure of the imposed coastal jet may be considered, but it is stressed that this jet is presently structured after observed jets. More realistic buoyancy forcing at the surface, and a mixed layer formulation, should be included in order to allow a meaningful comparison between model fields and the more plentiful observations that are available at the surface.

LIST OF REFERENCES

Batteen, M.L., R.L. Haney, T.A. Tielking, P.G. Renaud, A Numerical Study of Wind Forcing of Eddies and Jets in the California Current System, J. Mar. Res., 47, 493-523, 1989.

Brink, K.H., R.C. Beardsley, P.P. Niiler, M. Abbott, A. Huyer, S. Ramp, T. Stanton, D. Stuart, Statistical Properties of Near-Surface Flow in the California Coastal Transition Zone, J. Geophys. Res., 96, 14,693-14,706, 1991.

Dewey, R.K., J.N. Moum, C.A. Paulson, D.R. Caldwell, S.D. Pierce, Structure and Dynamics of a Coastal Filament, J. Geophys. Res., 96, 14,885-14,907, 1991.

Dietrich, D.E., D.-S. Ko, A Semi-Collocated Ocean Model Based on the SOMS Approach, Int. J. Numer. Methods Fluids, 19, 1103-1113, 1994.

Federiuk, J., J.S. Allen, Upwelling Circulation on the Oregon Continental Shelf. Part II: Simulations and Comparisons with Observations, J. Phys. Oceanogr., 25, No. 8, 1995.

Haidvogel, D.B., A. Beckmann, K.S. Hedstrom, Dynamical Simulations of Filament Formation and Evolution in the Coastal Transition Zone, J. Geophys. Res., 96, 15,017-15,040, 1991.

Huyer, A., P.M. Kosro, Mesoscale Surveys Over the Shelf and Slope in the Upwelling Region Near Point Arena, California, J. Geophys. Res., 92, 1655-1681, 1987.

Huyer, A., P.M. Kosro, J. Fleischbein, S.R. Ramp, T. Stanton, L. Washburn, F.P. Chavez, T.J. Cowles, S.D. Pierce, R.L. Smith, Currents and Water Masses of the Coastal Transition Zone off Northern California, June to August 1988, J. Geophys. Res., 96, 14,809-14,831, 1991.

Kosro, P.M., Structure of the Coastal Current Field off Northern California During the Coastal Ocean Dynamics Experiment, J. Geophys. Res., 92, 1637-1654, 1987.

Kosro, P.M., A. Huyer, S.R. Ramp, R.L. Smith, F.P. Chavez, T.J. Cowles, M.R. Abbott, P.T. Strub, R.T. Barber, P. Jessen, L.F. Small, The Structure of the Transition Zone Between Coastal Waters and the Open Ocean off Northern California, Winter and Spring 1987, J. Geophys. Res., 96, 14,707-14,730, 1991.

Levitus, S., Climatological Atlas of the World Ocean, NOAA Prof. Pap. No. 13, U.S. Government Printing Office, Washington D.C., 173 pp, 1982.

McCreary, J.P., Y. Fukamachi, P.K. Kundu, A Numerical Investigation of Jets and Eddies Near an Eastern Ocean Boundary, J. Geophys. Res., 96, 2515-2534, 1991.

Pares-Sierra, A., W.B. White, C.-K. Tai, Wind-driven Coastal Generation of Annual Mesoscale Activity in the California Current, J. Phys. Oceanogr., 23, 1110-1121, 1993.

Ramp, S.R., P.F. Jessen, K.H. Brink, P.P. Niiler, F.L. Daggett, J.S. Best, The Physical Structure of Cold Filaments Near Point Arena, California During June 1987, J. Geophys. Res., 96, 14,859-14,883, 1991.

Strub, P.T., P.M. Kosro, A. Huyer, The Nature of the Cold Filaments in the California Current System, J. Geophys. Res, 96, 14,743-14,768, 1991.

Strub, P.T., C. James, The Large-scale Summer Circulation of the California Current, Geophys. Res. Letters, 22, 207-210, 1995.
Swensen, M.S., P.P. Niiler, K.H. Brink, M.R. Abbott, Drifter Observations of a Cold Filament off Point Arena, California, in July 1988, J. Geophys. Res., 97, 3593-3610, 1991.

Tafti, D., Alternate Formulations for the Pressure Equation Laplacean on a Collocated Grid for Solving the Unsteady, Incompressible Navier-Stokes Equations, J. Computation. Phys., 116, 1995.

INITIAL DISTRIBUTION LIST

		No. Copies
1.	Defense Technical Information Center Cameron Station Alexandria, Virginia 22304-6145	2
2.	Library, Code 52 Naval Postgraduate School Monterey, California 93943-5101	2
3.	Oceanography Department Code OC/Bf Naval Postgraduate School 833 Dyer Rd. Rm 331 Monterey, California 93943-5122	1
4.	Dr. Robert L. Haney Code MR/Hy Naval Postgraduate School 589 Dyer Rd. Rm 121 Monterey, California 93943-5114	5
5.	Dr. Jeffery D. Paduan Code OC/Pd Naval Postgraduate School 833 Dyer Rd. Rm 348 Monterey, California 93943-5122	1
6.	Dr. Manny D. Fiadeiro Office of Naval Research Navy Ocean Modeling and Prediction 800 N. Quincy St. Arlington, Virginia 22217	1
7.	LCDR Stanley A. Akahoshi 110 Woods Ave Bergenfield, New Jersey 07621	2